Russian Original Vol. 49, No. 4, October, 1980

April, 1981

SATEAZ 49(4) 657-710 (1980)

SOVIET ATOMIC ENERGY

АТОМНАЯ ЭНЕРГИЯ
(ATOMNAYA ÉNERGIYA)

TRANSLATED FROM RUSSIAN

c/b **CONSULTANTS BUREAU, NEW YORK**

SOVIET ATOMIC ENERGY

Soviet Atomic Energy is a translation of *Atomnaya Énergiya*, a publication of the Academy of Sciences of the USSR.

An agreement with the Copyright Agency of the USSR (VAAP) makes available both advance copies of the Russian journal and original glossy photographs and artwork. This serves to decrease the necessary time lag between publication of the original and publication of the translation and helps to improve the quality of the latter. The translation began with the first issue of the Russian journal.

Consultants Bureau journals appear about six months after the publication of the original Russian issue. For bibliographic accuracy, the English issue published by Consultants Bureau carries the same number and date as the original Russian from which it was translated. For example, a Russian issue published in December will appear in a Consultants Bureau English translation about the following June, but the translation issue will carry the December date. When ordering any volume or particular issue of a Consultants Bureau journal, please specify the date and, where applicable, the volume and issue numbers of the original Russian. The material you will receive will be a translation of that Russian volume or issue.

Subscription (2 volumes per year)
Vols. 48 & 49: $335 (domestic); $374 (foreign)
Vols. 50 & 51: $380 (domestic); $423 (foreign)

Single Issue: $50
Single Article: $7.50

CONSULTANTS BUREAU, NEW YORK AND LONDON

c/b
233 Spring Street
New York, New York 10013

Published monthly. Second-class postage paid at Jamaica, New York 11431.

Soviet Atomic Energy is abstracted or indexed in *Chemical Abstracts, Chemical Titles, Pollution Abstracts, Science Research Abstracts; Parts A and B, Safety Science Abstracts Journal, Current Contents, Energy Research Abstracts,* and *Engineering Index.*

SOVIET ATOMIC ENERGY

A translation of *Atomnaya Énergiya*

April, 1981

Volume 49, Number 4 October, 1980

CONTENTS

The Russian press date (podpisano k pechati) of this issue was 9/22/1980. Publication therefore did not occur prior to this date, but must be assumed to have taken place reasonably soon thereafter.

ARTICLES

CHEMICOTECHNOLOGICAL CYCLES OF CERTAIN NUCLEAR POWER STATION CIRCUITS BY MEANS OF SAMPLE-INDICATORS

V. M. Sedov, P. G. Krutikov,
L. I. Loshkova, A. P. Eperin,
I. A. Varovin, A. V. Tsykin,
A. I. Gromova, V. N. Belous,
and V. A. Gosteva

UDC 621.311.25.621.039

A study of the water–chemical cycle of nuclear power station systems suggests both observation for the water medium [1] and an investigation of the physicochemical state of the internal metal surface of the systems, in particular of the oxidation products of the metal and the state of the metal itself [2-4]. The quality characteristics of the water medium of the circuits associated with a reactor of the RBMK type (cassette cooling ponds, intermediate circuit of the purging secondary cooler, the cooling circuit of the control and safety rod channels and of the biological shield) over the period investigated (1977-1978) are shown in Table 1.

TABLE 1. Quality Characteristics of the Coolant in the Circuits Associated with the Reactor of a Nuclear Power Station

Nuclear power station circuit	$\varkappa$, μmho/cm	pH	J_0, μg-equiv/kg	Cl^-, μg/kg	Fe, μg/kg	Al, μg/kg	SiO_3^{2-}, μg/kg
Cooling circuit of the Control and safety rod channels							
before purification	0,7—1,8* 1,0	5,4—6,5 6,0	1,0—2,5 1,0	1,0—6,0 1,3	1,0—3,0 8	10—23 14	25—540 220
after purification	—	5,4—6,5 5,9	1,0—2,7 1,3	1,0—35 2,6	1,0—22 5	10—16 10	25—330 100
Biological shield cooling circuit	—	7,5—9,3 8,6	140—430 335	42—410 240	195—1000 460	—	—
Cassette cooling pond	—	6,2—7,5 7,0	140—990 590	150—2580 1140	120—800 560	—	—
Purging secondary cooler intermediate circuit	—	5,8—8,3 6,8	1,0—50 17	1,0—80 29	100—4100 1150	—	25—210 110

Nuclear power station circuit	F^-, μg/kg	H_2O_2, μg/kg	NH_3, μg/kg	O_2, mg/kg	CO_2, mg/kg	NO_2^-, μg/kg	NO_3^-, μg/kg
Cooling circuit of the control and safety rod channels							
before purification	< 20	4100—8840 5200	100	6,5—8,3 7,3	—	< 10	130—790 420
after purification	< 20	530—6080 2600	< 100	4,3—13,2 17,6	1,2—2,2 1,8	< 10	70—130 100
Biological shield cooling circuit	60—530 325	5—320 70	100—240 170	0,0025—0,60 0,13	< 0,1	10—12 11	26—130 60
Cassette cooling pond	170—340 230	5—230 130	100—200 130	—	—	—	—
Purging secondary cooler intermediate circuit	—	—	—	0,0025—0,0050 0,0030	1,4—3,7 2,6	—	—

*Numerator – minimum and maximum values; denominator – average value.

Translated from Atomnaya Énergiya, Vol. 49, No. 4, pp. 211-216, October, 1980. Original article submitted March 19, 1980.

0038-531X/80/4904-0657$07.50

TABLE 2. Chemical and Phase Composition of Deposits

Location of sample-indicators	Steel		Time of cooling of samples 3200 h							Time of cooling of samples 9000 h						
	of circuit	of samples	chemical composition, % on weighing					phase composition of iron oxide compounds, %		chemical composition, % on weighing					phase composition* of iron oxide compounds, %	
			Fe	Mn	Cr	Ni	Cu	Fe_3O_4	γ-FeOOH	Fe	Mn	Cr	Ni	Cu	Fe_3O_4	γ-FeOOH
Control and safety rod cooling circuit emergency tank	Kh18-N10T	3	63.5	0,57	0,07 (ε=12%)	0,025 (ε=14%)	0,024	90	10	67,0	0,30	0,03	0,05	0,03	60	40
		20	65,2	0,38	0,05	0,01	0,01	90	10	68,3	0,43	0,05	0,08	0,06	70	30
Expansion tank of biological shield cooling circuit	10KhSND	3	66,7	0,45	0,07	0,015	0,09	100	—	67,7	0,40	0,05	0,01	0,09	100	—
		20	67,8	0,28	0,02	—	—	70	30	65,3	0,40	0,23	0,05	0,04	90	10
		10KhSND	—	—	—	—	—	—	—	53,9	1,1	3,4	0,32	1,7	100	1
Expansion tank of purging secondary cooler intermediate circuit	20	3	67,2	0,065	0,05	0,06	0,56	90	10	65,0	0,42	0,01 (ε=12%)	0,06	0,27	100	—
		20	63,5	0,10	0,045	0,08	0,36	90	10	68,3	0,32	0,03 (ε=13%)	0,03	0,13	100	—
Cassette cooling pond	Kh18-N10T	3	64,9	0,20	0,001	0,03	0,13	60	40	61,0	0,30	0,02	0,04	0,05	30	70
		20	63,1	0,33	0,03	0,01	0,04	35	65	61	0,42	0,01	0,04	0,01	45	55
		10KhSND	59,5	0,48	0,30	0,16	0,20	40	60	66,8	0,72	0,35	0,11	0,25	40	60

*Relative yield of iron oxide compounds in the corrosion deposits is taken arbitrarily as 100%.

Declassified and Approved For Release 2013/02/14 : CIA-RDP10-02196R000800040004-9

TABLE 3. Porosity of Corrosion Deposits Firmly Bonded with the Surface of the Sample-Indicators Installed in the Circuits, pores/cm^2

Mater. of sample-indic. (steel)	Emergency tank of control and safety rod cooling system	Expansion tank of biol. shield cooling circuit	Compartment of biol. shield tank	Expan. tank of purging secondary cooling intermed. circuit	Cassette cooling pond
3	45—75	12—55	—	8—20	22—70
20	12—18	3—8	83—97	31—45	32—150
10KhSND	—	38—48	—	—	53—67

In order to study the state of the metal, mechanically cleaned, degreased, and weighed sample-indicators of the structural materials of the nuclear power station were used. They were placed in the cassette cooling pond, in one of the compartments of the biological shield tank, in the control and safety rod emergency tank and the expansion tanks of the biological shield cooling circuit and the intermediate circuit of the purging secondary cooler, on selected brackets according to the grades of steel. After exposure in the water medium of the systems under operating conditions, the sample indicators were removed and studied. After removal, the samples were subjected to a detailed visual examination, the nature of the metal corrosion and the rate of corrosion were determined, and chemical, isotopic, and phase analyses of the corrosion products were carried out by the methods described earlier [2-3]. The relative error of the determination (ε, %) was compiled for the gravimetric analysis as not more than 10%. For cases exceeding this value, the errors are given in Table 2 in brackets.

In addition, the porosity of the oxide deposits, firmly bonded with the surface of the sample-indicators, were investigated by the ferrocyanide method [4]. The electrochemical characteristics of the metal surfaces with the firmly bonded corrosion products were investigated by comparing the anode potential relations obtained for polished samples and the sample-indicators [5]. The surfaces of the sample-indicators of Kh18-N10T steel and alloy 125 were covered with a thin layer of superficial, loose corrosion products, easily abraded by india rubber down to the pure surface of the metal. The surface of the samples of perlite steel, taken out of the cassette cooling pond and the emergency and expansion tanks, were covered with a loose layer of corrosion products having a dark-brown color. No dense, thin oxide films are formed in these systems.

The sample-indicators from the compartment of the biological shield were covered with a thin layer of deposits of a black color, loosely bound with the surface of the metal and quite easily abraded with india rubber. It was not possible to take the deposits from these samples in a quantity sufficient for phase and chemical analysis. The oxide layers investigated, firmly bonded with the metal surface, are porous. The porosity data are shown in Table 3. The number of pores attains 150 per cm^2. Some reduction of the porosity of the oxide layers is noted in the upper surfaces of the horizontally placed samples during their exposure in the circuits investigated. Based on the data obtained, it was not possible to show any relationship, and the porosity of the deposits firmly bonded with the metal surface requires to be studied.

The investigation of the electrochemical characteristics of the metal surface was carried out for steel 20 in a solution of borate buffer. It can be seen from the potentiodynamic relations obtained, shown in Fig. 1, that for the sample-indicators with the corrosion products on the surface and taken from the compartment of the biological shield tank, no region of active dissolution is observed. In the region of potentials of $\varphi = -0.3$-$+0.3$ V (relative to normal hydrogen electrode – normal hydrogen equivalent), a higher current density is noted than for steel 20 polished, which obviously can be explained as a phase transition that takes place in the deposits covering the metal surface, as well as a change of the mechanism of dissolution of the metal in the presence of the oxide deposits.

The steady potential of the metal with the corrosion products is displaced into the positive region and corresponds to the passivation potential of the peak appearing on the potentiodynamic relations obtained, $\varphi_{steady} = 0.17$ V (relative to normal hydrogen equivalent). The electrochemical properties of individual parts of the surface ($S = 1$ cm^2) of the sample-indicators are different which, probably, is due to the nonidentical porosity of the corrosion products. The anode current density can differ for one and the same potential by a factor of 1.5. The position of the critical passivation potential and the steady potential on curves 2-4 is un-

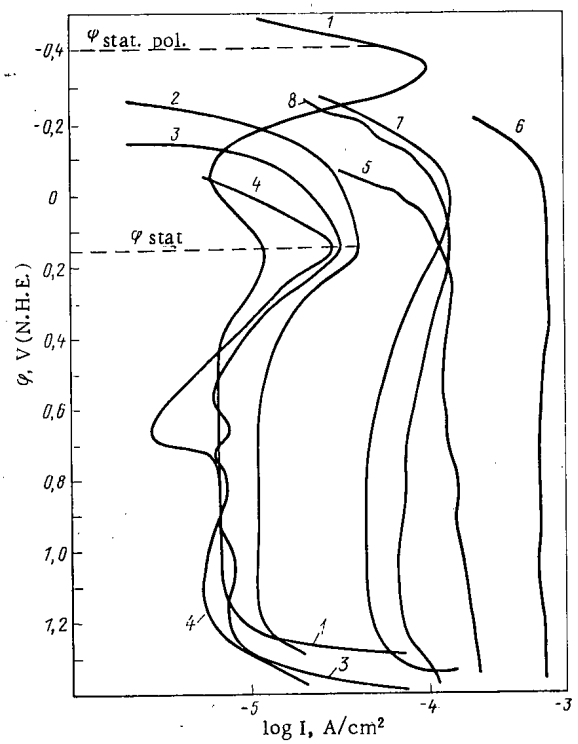

Fig. 1. Potentiodynamic relations for sample-indicators made of steel 20: 1) for polished sample; 2-4) for samples from the compartment of the biological shield; 5, 6) lower and upper surfaces, respectively, for samples from the expansion tank of the biological shield cooling circuit; 7, 8) the same, for samples from the expansion tank of the intermediate circuit.

changed. The potentiodynamic relations obtained confirm the formation of a passivating film on the surface of the sample-indicators from the compartment of the biological shield tank.

In the water medium of the biological shield tank, the oxygen content amounts to 0.0025-0.600 mg/kg (see Table 1). With these conditions, the steady potential obviously will be displaced into the region of more negative potentials and on the metal surface a magnetic film will be formed, protecting the metal from corrosion [6].

The anode potentiodynamic relations for the sample-indicators from the expansion tanks of the biological shield cooling circuit and of the intermediate circuit (curves 5-8) show that the samples have been in corrosion-dangerous conditions. The films of corrosion product oxides have protective properties. On the potentiodynamic curves, a shift is observed of the critical passivation potential to the more positive region by comparison with the relation for the polished sample. The anode current density over the whole range of potentials investigated, on different parts of the surface of the sample-indicators, is high and exceeds the critical passivation current of the polished sample. The films of corrosion products on these surfaces not only do not possess protective properties, but even initiate corrosion. The rate of overall corrosion was determined by the gravimetric method, and the depth of the corrosion site was determined with the MMR-2R microscope (Table 4).

The chemical composition of the corrosion deposits (see Table 2) closely resembles the chemical composition of the samples. This implies that the deposits on the samples are due mainly to corrosion products of the sample-indicators themselves. The effect of composition of the structural materials of the circuits is expressed only insignificantly because of the low rate of movement of the coolant in the system. The phase composition of the loose deposits was determined by the method of nuclear γ-resonance on the YaGRS-4 spectrometer.

TABLE 4. Results of Corrosion Tests of Sample-Indicators in Nuclear Power Station Systems

Location of sample-indicators	Material of samples (steel)	Rate of corrosion: over 3200 h, overall, g/m²·day	over 3200 h, overall, mm/yr	over 3200 h, by pits (max.), mm/yr	over 9000, 5600,* and 18,000† h, g/m²·day	over 9000, 5600,* and 18,000† h, mm/yr	by pits (max.), mm/yr	Nature of corrosion
Emergency tank of control and safety rod cooling circuit	3	1,6	0,075	0,35	1,15	0,071	0,18	Nonuniform, point
	20	2,0	0,094	0,29	1,50	0,054	0,135	
	Kh18N10T	< 0,001	< 0,00005	—	< 0,001	< 0,00005	—	Ditto
	Alloy 125	< 0,001	< 0,00005	—	< 0,001	< 0,00005	—	No corrosion damage
								Ditto
Expansion tank of the biological shield cooling circuit	3	3,3	0,155	0,48	1,70	0,080	0,33	Nonuniform, point
	20	3,0	0,141	0,40	1,30	0,066	0,13	
	10SND	—	—	—	2,20	0,103	0,37	Ditto
	Kh18N10T	< 0,001	< 0,00005	—	< 0,001	< 0,00005	—	Nonuniform, point with patches
								No corrosion damage
Compartment of biological shield tank	20				0,23	0,01	—	No corrosion damage
Expansion tank of the intermediate purging secondary cooler circuit	3	0,9	0,042	0,52	0,80	0,080	0,23	Nonuniform, point with patches
	20	0,95	0,045	0,27	0,90	0,039	0,17	Ditto
	Kh18N10T	< 0,001	< 0,0005	—	0,001	< 0,00005	—	No corrosion damage
Cassette cooling pond	3	2,3	0,108	0,46	1,0	0,047	0,20	Nonuniform, point with patches
	20	2,3	0,108	0,24	1,80	0,094	0,15	Ditto
	10KhSND	2,6	0,122	0,60	1,10	0,056	0,29	" "
	18N10T	< 0,01	0,00005	—	< 0,001	< 0,00005	—	No corrosion damage

* For steel 10KhSND.

† For St. 20 in compartment of biological shield tank.

The radioactivity of the corrosion products is due to radionuclides of corrosion origin: ^{51}Cr, ^{95}Nb, ^{95}Zr, ^{58}Co, ^{60}Co, ^{54}Mn, ^{59}Fe, ^{65}Zn. The presence of radioactivity due to long-lived radionuclide fission products (^{134}Cs, ^{137}Cs, ^{144}Ce) is explained by the periodic makeup of the auxiliary circuits with water from the emergency feed filling containing these radionuclides.

Discussion of the Results

By considering jointly the results of the investigations of the water medium of a nuclear power station system [1] and its bounding structural materials (by sample-indicators), the following basic conclusions can be drawn:

1. The neutral uncomplicated water-chemical condition of the control and safety rod system is found to be the optimum combination with the structural materials comprising this system.

In steel of the austenitic class and zirconium alloy, corrosion is minimal and there is no visually observable corrosion damage whatsoever. With the introduction into this circuit of perlite steel (steel 20), corrosion starts with a rate from 1.15 to 1.5 g/m²·day, which has a point nonuniform nature. Therefore, the use in this circuit of perlite steel as the structural material requires the development of a special water–chemical cycle, which will reduce the rate down to acceptable values – 0.22 to 1.08 g/m²·day [7].

2. During the period investigated, in the water medium of the cooling ponds a significant content of chloride ions is noted (up to 2580 μg/kg) and corrosion products (up to 1000 μg/kg). The increased content of chloride ions was caused by the inflow of seawater as a result of failure in the heat exchanger, and the entrance of wash-water from the central hall. Under these conditions, austenitic steel has the minimum rate of corrosion, and there is no visually observable damage; perlite steel corrodes with a rate of 1.0–1.8 g/m²·day, and the corrosion is of a pitting nature. The increased content of chloride ions in the water medium as the result of local superheatings can lead to chloride cracking of both the lining of the cooling ponds and the sheaths of the cassettes. With a significant concentration of iron in the coolant, the corrosion products can be deposited on the bottom of the pond and can cause the development of sludge corrosion. As the cooling pond serves not

only for the temporary cooling of the spent fuel elements, but also for recharging the working cassettes, the presence of a significant quantity of corrosion products is unacceptable. Because of this, since October 1978 an additional purification of the coolant of the ponds has been introduced, on ion-exchange filters (previously the periodic purification of the water medium of the ponds was carried out only on mechanical filters), as a result of which the quality characteristics of the coolant were changed: pH = 5.8-7.4; Cl^- = 40-110 μg/kg; Fe = 40-150 μg/kg; J_0 = 1-50 μg-equiv/kg; $\varkappa$ = 0.8-2.9 μmho/cm.

Thus, when using perlite steel in the cooling systems of cooling ponds, the strict introduction of a water-chemical cycle is necessary, using mechanical and ion-exchange purification of the water medium.

3. The results of the corrosion tests of the sample-indicators in the cooling circuit of the biological shield showed that in the circulation loop and in the expansion tank of the biological shield the nature of the corrosion and the rate of corrosion are different.

Perlite steel in the circulation cooling loop of the biological shield corrodes at the rate of 0.23 g/m^2·day, which is acceptable for the materials used in reactor construction; the corrosion is of a uniform nature. In the expansion tank, perlite steel corrodes at the rate of 1.3-2.2 g/m^2·day and the corrosion is of a local nature. As the coolant is identical in chemical composition in both the expansion tank and in the circulation loop, this difference is explained by the different content of oxygen in the water. In view of the nonhermeticity of the expansion tank, the water in it is aerated with oxygen from the air (C_{O_2} = 6-7 mg/kg). In the circulation loop entering from the water filler and makeup, the oxygen is almost completely expended in corrosion processes (C_{O_2} = 0.0025-0.6 mg/kg).

4. In the intermediate circuit of the purging secondary cooler, the oxygen content is low (0.0025-0.0050 mg/kg) and in the nonhermetically sealed expansion tank it is 6-7 mg/kg which obviously also was the cause of the strong development of local corrosion on the sample-indicators placed in the tank. The corrosion rate of perlite steel amounts to 0.8-0.9 g/m^2·day. In view of the hermeticity of the intermediate circuit itself, the entry of O_2 into the coolant is possible only during filling and subsequent makeup of the circuit with water; the O_2 initially entering the circuit is expended in corrosion processes.

In the future, just as experience in the operation of nuclear power stations shows, with the very small makeups of the intermediate circuit with water, the content of O_2 in the water will amount to 0.0025-0.0050 mg/kg. Consequently, it may be supposed that the actual rate of corrosion of perlite steel in the intermediate circuit of the purging secondary cooler will be at the level of the rate of corrosion in the circulation loop of the biological shield.

Thus, the conclusion can be drawn that the hermetic sealing of the cooling circuit of the biological shield and the intermediate circuit of the purging secondary cooler is a positive structural solution. But it should be noted that with a low circulation speed of the coolant (about 0.001 m/sec) in the compartment of the biological shield, favorable conditions are created for the buildup of a sludge of corrosion products. In avoiding the development of sludge corrosion, the content of Cl ions in the water should be limited. In the expansion tanks of these circuits, in which the corrosion of the structural materials is considerable and is of a local nature, it is essential that measures be developed for protecting the surfaces of these tanks.

LITERATURE CITED

1. V. M. Sedov, At. Energ., 47, No. 5, 294 (1979).
2. V. M. Sedov et al., At. Energ., 46, No. 1, 23 (1979).
3. P. G. Krutikov et al., Teploenergetika, No. 6, 13 (1978).
4. Laboratory Experiments on the Corrosion and Protection of Metals [in Russian], Metallurgiya, Moscow (1971).
5. V. M. Sedov et al., At. Energ., 47, No. 5, 340 (1979).
6. I. K. Morozova et al., Removal of Corrosion Product Deposits of Reactor Materials [in Russian], Atomizdat, Moscow (1975).
7. V. V. Gerasimov, A. I. Kasperovich, and O. I. Martynova, Water Cycles of Nuclear Power Stations [in Russian], Atomizdat, Moscow (1976).

BASIC PRINCIPLES FOR ENSURING NUCLEAR SAFETY IN DESIGNS OF TRANSPORTABLE PACKAGED ASSEMBLIES

V. P. Il'in, A. N. Kondrat'ev, and S. G. Lebedenko

UDC 621.039.59.00271,68

The problems of transportation of spent nuclear fuel from nuclear power stations are related with the solution of a complex of problems to ensure nuclear safety. The special measures adopted at present for the conveyance of this fuel provide a relatively low probability of transportation accidents which might lead to damage of the transported packages. According to estimates of foreign experts, the probability of an accident on railroad transport (per mile) amounts to $(0.8\text{-}2.5)\cdot 10^{-6}$. In this case, the probability of damage to the containers (in an accident) is $1.6\cdot 10^{-5}$ to $9.5\cdot 10^{-2}$ [1]. However, with the sharp increase of transport which would be expected in the next few years, the number of accidents can increase. Therefore, when designing new transportable packaged assemblies, a more rigorous analysis of their nuclear safety is required.

At the present time "Regulations for Nuclear Safety during the Transportation of Spent Nuclear Fuel" (PBYa-06-08-77) have been approved and brought into operation, in which the general principles and basic requirements are stated for ensuring nuclear safety in the design and operation of transportable packaged assemblies. When developing a design for the construction of a packaged assembly, it is necessary to assess the nuclear safety at all stages of the design, and also to take into account both normal and hazardous conditions of transportation. In order to ensure nuclear safety with sufficient margin for each individual package, one of the following limitations must be fulfilled: the mass of fissile material must not exceed 80% of the critical mass of the system, similar to that being considered; the effective neutron multiplication factor k_{eff} must not exceed 0.95 [2].

When calculating the critical parameters, it is necessary to take account of the geometry and spatial distribution of the fissile and nonfissile materials in the package, their nuclear-physical properties, composition of the fuel component (taking account of burnup), and the presence of reflectors and absorbers. The assurance of nuclear safety during the transportation of spent nuclear fuel in normal conditions is achieved by means of symmetrically installed fuel elements in the transport packaged assembly with a uniform pitch, for which $k_{eff} = 0.95$. In order to convey the spent fuel of the VVÉR-440 and the VVÉR-1000, the TK-6 and TK-10 packages, respectively, are used (in Table 1, the characteristics for the first version of package design). When analyzing nuclear safety, the conditions of storage of the spent nuclear fuel should also be taken into account. If it is located in a cooling pond in the same transportation flasks, then in order to assess the nuclear safety, it is necessary to take account of the conditions of safe storage, as neutron interaction occurs between adjacent flasks.

Specific difficulties arise in the early stages of design development, when it is necessary to carry out a preliminary analysis of nuclear safety in order to impose the requirements for the strength of the package, i.e., of the packaged assembly, of the loaded fuel elements, and for ensuring the preservation of the contents. In this case, the results of generalization of fuel transportation, analysis of accident situations and previous tests simulating accident conditions and carried out on models or on full-sized samples can be used as the starting data for the physics calculations; also the results of strength calculations can be used to establish the nature and extent of possible damage to the package.

These data, possibly, do not give sufficient statistical information for a quantitative estimate of mechanical damage; however, the data obtained allow a qualitative pattern to be compiled of subsequent accidental damage. It has been established [5] that a variety of possible damage to the packages, in some way or other affecting the change of reactivity of the system, can be represented as the combination of a limited number of types of damage to the structure, each of which has its special features in the analysis of nuclear safety and is characterized by its critical parameters. Taking these situations into account, a classification was proposed of mechanical damages and their consequences, which it is advantageous to consider when analyzing nuclear

Translated from Atomnaya Énergiya, Vol. 49, No. 4, pp. 216-218, October, 1980. Original article submitted August 13, 1979.

0038-531X/80/4904-0663$07.50

TABLE 1. Principal Package Characteristics [3, 4]

Type of package	Shape of containers	Dimensions, cm	Fuel shielding of steel, cm	Mass of fuel (UO_2), tons	No. of fuel elements	Arrangement of fuel assemblies	k_{eff}*
TK-6	Vertical cylinder	Diam. 230, height 440	36	3.6	30	With pitch 22.5 cm in a triangular lattice	0.884; 0.756
TK-10	Horizontal cylinder	Diam. 210, length 610	39.5	3.0	6	Around a circle, distance between centers of assemblies 40 cm	0.845; 0.658

*First figure – for fresh fuel; second figure – spent fuel.

TABLE 2. Classification of Mechanical Damage

Nature of damage	Consequence of damage, representing a hazard	Parameters, taken into account when analyzing nuclear safety
Unsealing of container	Entry of water into package, if presence of water has not been provided for in the design	Neutron multiplication factor in the system formed
	Loss of coolant, if damage leads to melting of the fuel	Case excluded (PBYa-06-08-77)
Depressurization of container	Loss of contents	Case intolerable (PBYa-06-08-77)
Relative displacement of fuel element assemblies	Formation of compact groups of fuel element assemblies	Minimum number of fuel element assemblies forming a critical system
	Reduction of distance between fuel element assemblies, uniform or nonuniform reduction of lattice pitch	Maximum permissible uniform reduction of lattice pitch Nonuniform displacement of fuel element assemblies creating the critical system
Rupture of fuel element assemblies and fuel elements	Filling of container space with fragments of fuel elements and fuel element assemblies	Critical mass of system formed by fragments of fuel elements, in optimum package and with optimum reflector
	Discharge of fuel and fuel elements and filling of the container space with fragments of fuel mixed with coolant	Critical mass of system formed by mixture of pieces of fuel and coolant, of optimum shape and density, with optimum reflector

safety (Table 2). It is shown in column 3 what critical parameters are taken into account when analyzing the danger of the corresponding damage.

Based on the calculations carried out, the acceptable damages have been established for which the package will be nuclear-safe. Then the requirements are formulated for the design of a packaged assembly conforming to the limitation of damage within permissible limits. The order of carrying out the preliminary analysis of the nuclear safety of the transportable packaged assemblies was tested with the production of the TK-6 assembly and the development of the requirements for the TK-10 assembly (Table 3). Based on these data, the requirements were determined for designing packaged assemblies of these units. The results obtained allowed the conclusion to be drawn that in the TK-6 and TK-10 packaged assemblies, from the point of view of nuclear safety considerable damages are acceptable – those which could lead to the movement of tens (in the case of fuel spilling out of the fuel elements) or hundreds (in the absence of spillage) of kilograms of fuel.

TABLE 3. Results of Preliminary Estimates of the Nuclear Safety of the TK-6 and TK-10 Assemblies in Accident Conditions

Nature of damage	Consequence of damage	Determining parameter	Type of fuel conveyed	Values of defining parameters			
				dangerous		permissible	
				TK-6	TK-10	TK-6	TK-10
Relative displacement of fuel element assemblies	Formation of compact groups	Minimum number of fuel element assemblies (fuel elements) forming a critical system	Fresh/spent	6 Fuel element assemblies*	675 Fuel elements 936 Fuel elements	4 Fuel element assemblies 30 Fuel element assemblies*	540 Fuel elements 750 Fuel elements
	Uniform reduction of lattice pitch of fuel element assemblies	Maximum permissible reduction of lattice pitch	Fresh	More than 10 mm	More than 10 mm	10 mm*	1.5 kg
Rupture of fuel element assemblies and fuel elements	Formation of a hazardous system of uranium dioxide and water	Critical mass of sphere of uranium dioxide and water	Spent	2.1 kg† ^{235}U 5 kg U + Pu	1.9 kg ^{235}U	1.7 kg ^{235}U 4 kg U + Pu	^{235}U
	Formation of a hazardous system of fuel element fragments and fuel element assemblies	Critical mass of system		20 Fuel element assemblies	1.5 Fuel element assemblies	16 Fuel element assemblies	1.2 Fuel element assemblies

*Data obtained in the I. V. Kurchatov Institute of Atomic Energy.
†Data obtained in the Division of Nuclear Safety, Physico-Power Institute.

The results of the work on the conduct of the preliminary analysis of the nuclear safety of transportable packaged assemblies were discussed at a conference of specialists on the problem of transportation of nuclear fuel from the member-countries of COMECON in 1978 in Leningrad.

CONCLUSIONS

Any design of transportable packaged assemblies intended for the conveyance of spent nuclear fuel must meet the requirements of PBYa-06-88-77 and must give representative evidence of nuclear safety. The proposed classification of damage established a suitable procedure for calculating the critical parameters of the system when carrying out the preliminary analysis of the nuclear safety of packaged assemblies at different stages of their design. After the preliminary analysis of the nuclear safety of the TK-6 and TK-10 packaged units, the acceptable significant and dangerous damage has been established, which leads to displacement of the fuel within the package, which creates a real possibility for the technical assurance of nuclear safety.

LITERATURE CITED

1. J. Russel, "An evaluation of risk models for radioactive material shipments," in: Proceedings of the Fourth International Symposium of Packaging and Transportation of Radioactive Materials, Miami Beach, Florida, USA, 22-27 Sept., 1974.
2. Regulations for Nuclear Safety during the Transportation of Spent Nuclear Fuel [in Russian], (PBYa-06-08-77), Gosatomnadzor SSSR.
3. P. A. Andreev et al., in: Proceedings of the Central Committee of Heavy Industry [in Russian], No. 142, 10 (1977).
4. V. S. Vnukov, L. V. Diev, and Yu. A. Prokhorov, Problems of Nuclear Safety during the Transportation of Spent Fuel in TK-6 and TK-10 Packages [in Russian], Report of a Conference of Specialists of Member-Countries of COMECON on the Transportation of Spent Fuel Elements, Leningrad (1979), p. 97.

5. V. P. Il'in and S. G. Lebedenko, Preliminary Analysis of Nuclear Safety of Transportable Packages [in Russian], Report of a Conference of Specialists of Member-Countries of COMECON on the Transportation of Spent Fuel Elements, Leningrad (1979), p. 87.

CESIUM VAPOR SOURCE BASED ON A THERMAL TUBE FOR LOOP THERMOEMISSIVE INSTALLATIONS

P. I. Bystrov, V. P. Kirienko, A. N. Popov, and V. V. Sinyavskii

UDC 621.362:629.78.06

During tests of thermoemissive installations, the interelectrode gaps of the converters most frequently are provided with cesium vapor by means of a thermostat [1]. In this case, in order to exclude the entry of cesium vapor into the vacuum lines of the equipment system, the thermostat is cut off by a special valve from the vacuum system. However, in order to remove desorbing gases and the gaseous fission fragments which appear during operation, the valve is opened periodically,as a result of which either cesium vapor can be withdrawn into the vacuum lines or, during opening of the valve, the temperature should be reduced with a corresponding change of the cycle of testing of the installations. Moreover, repeated cycles of opening and closing of the valve could lead to the loss of its hermeticity and the microleaks which appear could lead to the additional outflow and condensation of cesium vapor in the vacuum lines. Therefore, the need arises to design a cesium system which allows simultaneously with the entry of the cesium vapor the continuous removal of gases from the interelectrode gaps of the converters, without withdrawing cesium and without disturbing the testing cycle of thermoemissive installations.

Such a system can be suggested as a cesium vapor source with a wick system for returning the liquid cesium, in which the operating principle of a thermal tube is used (Fig. 1). In the thermal tube of the vapor generator, on the inside surface of which is fixed a metal-fiber wick, three zones can be distinguished:

a zone of vaporization, located in the lower part, which heats the surrounding electroconverter. If the vapor generator is placed close to the core, the required temperature can be ensured because of the radiation heating of the structure and the creation of the appropriate conditions of heat removal. In the vaporization zone, there is a tube with an opening for sampling the cesium vapor in the thermoemissive converter (TEC) and thermocouples for determining the temperature of the vapor stream;

a zone of condensation, located above, cooled from the outside by the reactor water. In order to intensify the condensation process of the cesium vapor, diaphragms with openings in a checkerboard pattern are located inside this zone. The upper part of the condensation zone is joined with the vacuum system;

a transition zone, located between the two zones, separated from the vaporization zone by a baffle disk with an opening.

The source being considered is not a system with cesium consumption; liquid cesium is returned to the vaporization zone through the wick and the gases are withdrawn into the evacuation system. The cesium losses will be determined by the temperature of the vapor at the outlet from the condensation zone and by the realistically achieved temperature in the cooled loop channels, and it will be negligibly small.

In order to verify the operating efficiency and to investigate the characteristics, four modifications of the vapor generator were developed and tested; these differed in the zone dimensions, structure of the wick, the dimensions of the openings, and the arrangement of the diaphragms. Tests were conducted on a special thermovacuum test rig. Preliminary evacuation of the vapor generator cavity (before opening the cesium ampules) was carried out at working temperature over 20 h, until a vacuum of 10^{-7} mm Hg was achieved (1 mm Hg = 133.322 Pa). The levels of liquid cesium in the ampules, vapor generator, and vapor pressure probe were recorded by means of an RUP-200-5 x-ray facility. During the tests, the position of the electric heater was varied over the height of the vapor generator.

Translated from Atomnaya Énergiya, Vol. 49, No. 4, pp. 219-221, October, 1980. Original article submitted December 11, 1979.

0038-531X/80/4904-0666$07.50

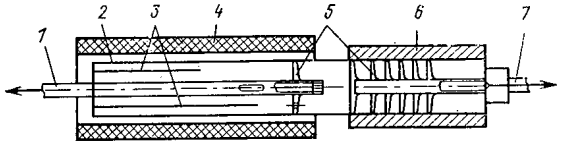

Fig. 1. Structural diagram of a vapor generator, based on a thermal tube: 1) tube for feeding cesium vapor into the interelectrode gaps of the TEC; 2) thermal tube with metal-fiber wick; 3) thermocouples for measuring the vapor temperature; 4) electric heater of the vaporization zone; 5) baffle diaphragms; 6) condensation zone cooler; 7) gas-vacuum main line.

By writing the balance of the pressure intensities for the closed vapor–liquid circuit, the following equation can be obtained for the coolant circulation in the thermal tube:

$$\Delta p_v + \Delta p_l + h\rho = 2\sigma \cos\theta / r_{vap} - 2\sigma \cos\theta / r_{con} \quad (1)$$

where σ and ρ are the surface tension coefficient and the density of liquid cesium, respectively; θ, contact angle of wetting of the structural material by the cesium; h, height of the buoyant liquid cesium in the wick; Δp_v and Δp_l, drop in pressure for the vapor and liquid phases of the coolant. The thermophysical properties of the cesium and the hydrodynamic characteristics of the metal-fiber wick were determined from [2-4]. Taking into account that under working conditions the absolute values of the vapor pressure in the vaporization and condensation zones are strongly different ($p_{vap} \gg p_{con}$), and the coolant flow rate is small ($\Delta p_l \ll \Delta p_{vap}$), it can be assumed that the capillary structure should overcome in practice the total vapor pressure in the vaporization zone. Then the maximum value of the capillary radius in the vaporization zone is determined by the expression

$$r_{vap} \leqslant 2\sigma \cos\theta / p_{max}, \quad (2)$$

where p_{max} is the maximum working value of the vapor pressure of the cesium.

The most loaded meniscus in the capillary structure is the meniscus located in the upper part of the vaporization zone (directly in front of the first diaphragm), as in this section the pressure of the liquid cesium is less than in the lower part of the vaporization zone. In the case of nonfulfillment of condition (1), the vapor located in the vaporization zone displaces the liquid phase from the wick and reduces the section for the passage of the liquid cesium, as a result of which "separation" begins, i.e., drying of the wick in the vaporization zone with subsequent superheating of the wall. When investigating the vapor generators with a different capillary structure, the dependence of the limiting permissible pressure p_{max} on the radius of the capillary r was verified. The results of the experiments coincide well with the theoretical relation $p_{max} = f(r)$ which is given in Fig. 2. The limiting pressure produced by the appearance of "separation" effects amounted to 23 mm Hg.

The height of ascent of the liquid cesium in the wick depends on the properties of the capillary structure. For $p_{vap} \approx p_{con}$ (the instant filling and impregnation of the wick with liquid cesium), the height of ascent of the cesium amounts to $h = h^*$, where $h^* = 2\sigma\cos\theta/r$. For $p_{vap} > p_{con}$, if there is an excess of liquid cesium, ascent of the cesium in the wick takes place to an additional height of $h^{**} = (p_{vap} - p_{con})/\rho$, compensating the pressure difference $p_{vap} - p_{con}$. If, in this case, the height of the vaporization zone $h_{vap} < h^{**}$, then liquid cesium is squeezed out from the vaporization zone into the condensation zone, or into the transition zone of the thermal tube. It was established by means of x radiographs that, as a result of squeezing out, liquid cesium accumulated in the transition zone above the first diaphragm. We note that with reduction of the pressure in the vaporization zone down to a value of $(p_{vap} - p_{con}) < \rho h^{**}$, liquid cesium poured into the lower part of the vaporization zone and the free level was reestablished.

During testing of the vapor generators with a small height of the vaporization zone, it was observed that at the instant of disappearance of the free level of the cesium, superheating of the lower part of the vaporization zone was observed. This, obviously, is explained by the cesium boiling in the wick, in consequence of the sharp reduction of pressure with the disappearance of the free level, from p_{vap} to $p_{vap} - 2\sigma\cos\theta/r_{vap}$. As, under working conditions, "separation" of the thermal tube can lead to failure of operation of the TEC, these events are unacceptable. Therefore, the minimum height of the zone of vaporization must be in excess of h^{**}.

The location of the first diaphragm and the sizes of the openings in it affect the operation of the cesium vapor source. With increase of the diameter of the openings and, consequently also, the flow rate of the circulating cesium, the vapor pressure gradient along the vaporization zone is increased. Therefore, the size of

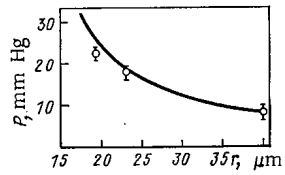

Fig. 2. Dependence of limiting permissible pressure of cesium vapor in the vaporization zone on the capillary radius.

the openings must be minimal, but sufficient for evacuating the installation and the removal of gaseous fission products during operation. In the loop channels, described in [1], in order to remove the gaseous fission products, two openings with a diameter of 0.5 mm are sufficient. However, the transmission efficiency of these openings is insufficient for the preliminary evacuation. Taking these contrary requirements into account, two openings were made in the first diaphragm with a diameter of 1 mm, and the transmission efficiency of this diaphragm is ~60 cm^3/sec (~30 cm^3/sec for the whole installation), which is almost an order of magnitude higher than the transmission efficiency of the interelectrode gaps of thermoemissive devices [1].

The location of the first diaphragm affects the limiting pressure of the cesium vapor developed by the generator, and the temperature gradient over the length of the vaporization zone. In order to eliminate pressure transfer of surplus liquid cesium from the vaporization zone to the transition zone with $p \approx 20$ mm Hg, it is essential that the distance from the surface of the liquid cesium to the first diaphragm should be not less than 150 mm. Experiments have shown that for the reliable operation of the vapor generator, the first diaphragm must be placed in the heating zone. In the contrary case, the effect of a low temperature of the condenser spreads to the upper part of the vaporization zone, which leads to its nonisothermicity. As a result of this, the temperature distribution of the vapor over the length of the vaporization zone represents a typical low-temperature cycle of the thermal tube. In this case, it is difficult to determine the pressure of the cesium vapor sampled in the gap of the TEC. In order to eliminate the temperature gradient in the vaporization zone, it is essential that the height of the heater should be greater than the height of the vaporization zone, and the first diaphragm should be lower than the upper end of the heater by approximately 10 mm. Moreover, it is desirable that the transition zone, where there is no heat supply or removal, should amount to 20-30 mm. Then the length of the condensation can be 70-90 mm.

The temperature field along the vapor generator is characterized by the isothermicity in the vaporization zone, with a sharp drop from the working temperature to a temperature which is somewhat higher than the temperature of the cooling water in the transition condensation zone. It was established by means of a cesium vapor probe, that with an isothermic vaporization zone the pressure of the cesium vapor fed into the TEC is determined quite reliably by the readings of the thermocopules installed in the vapor channel at the point of sampling of the vapor. The readings of all the other thermocouples, including the thermocouples located on the header and the wall of the tube, and also the values of the temperature of the vapor below the openings, do not determine the pressure of the vapor and may exceed the readings of the reference thermocouple by 15-30°C. We note that the same pressures can be observed also in normal thermostats heated from outside, as a result of which the actual cesium vapor pressure will be lower than that determined for the temperature of the wall.

In order to check the possible removal of cesium vapor into the vacuum system, endurance tests of the vapor generator were carried out at the working temperature. After the tests, no traces of cesium were observed in the vacuum line and the nitrogen trap. On the whole, reliable operation of the cesium vapor source based on the thermal tube with a metal-fiber wick is recorded, up to a vapor pressure of ~20 mm Hg. It is proposed to verify experimentally the operation of this type of cesium vapor generator with loop tests of thermoemissive installations similar to those described in [1].

LITERATURE CITED

1. V. I. Berzhatyi et al., At. Energ., 31, No. 6, 585 (1971).
2. É. É. Shpil'rain et al., Thermodynamic Properties of the Alkali Metals [in Russian], Standartov, Moscow (1970).

3. A. A. Smirnov, "Measurement of the energy of adhesion of the alkali metals," Candidate's Dissertation, Moscow Engineering Physics Institute, Moscow (1971).
4. M. G. Semena et al., Teplofiz. Vys. Temp., 13, No. 1, 162 (1975).

ESTIMATE OF THE ERRORS IN CALCULATING THE CRITICALITY AND BREEDING COEFFICIENTS OF FAST POWER REACTORS DUE TO INACCURACY OF THE NEUTRON DATA

P. N. Alekseev, G. N. Manturov, and M. N. Nikolaev

UDC 621.039.51.15:621.039.572.22:621.039.526

In papers by Soviet and foreign authors [1-13], great attention is paid to the estimate of the accuracy of the calculated predictions of the coefficients of criticality (k_{eff}) and breeding (CB) for fast power reactors. It has been established that the principal reason for the indeterminacy of the results of the calculated predictions of these (and other) physical characteristics of fast breeder-reactors are the errors in the neutron cross sections used in the calculations. The contributions of other sources of error (approximateness of the computational procedures, technological tolerances in the manufacture of the reactor components) are found to be significantly less.

The required accuracy of the calculated predictions of k_{eff} and CB for fast breeder-reactors was based on [1] and verified by more recent estimates [3]. These estimates start from a permissible error in calculating the critical mass of ~1.5% and in T_2 of ~10% and they amount to 0.5% for k_{eff} and 1.5% for CB (in [1], the permissible errors are found to be approximately twice as large, but this is because of the 90% confidence level, and not 67% as in the present paper). The accuracy of the calculations guaranteed by the accuracy of the knowledge of the neutron data achieved at the present time is considerably worse: according to the estimates of [2-12], it amounts to ~3-5% for k_{eff} and ~6-8% for CB. Based on these estimates, programs were developed for increasing the accuracy of the neutron data in microscopic and macroscopic experiments [3-7].

It should be noted that the previous estimates of the achievable level of accuracy referred roughly to 1970, and the discrepancy in the estimates of the accuracy of the calculated predictions are associated first and foremost with the difference in the estimates of the indeterminacies of the initial group cross sections. The spectrum of the sensitivity of k_{eff} and CB towards different forms of the neutron cross sections in the present paper and, e.g., in [4-6], as a comparison shows are identical. Thus, changes in the estimates of the accuracy of the calculated predictions for k_{eff} and CB of a fast breeder-reactor are dependent upon the consideration of the extensive data obtained during the last decade in differential neutron-physics experiments. Moreover, the predicted values of the achievable accuracy of the neutron cross sections in many cases are of a qualitative nature and are based on approximate estimates of the accuracy of the cross sections according to certain "recommendations," based on agreements between experts [12]. They do not take into account all the sources of errors in the differential measurements, and also the effect of a specific method of estimating the cross sections, on which the correlation properties of the errors in the group cross sections may depend.

The estimate of the accuracy of the calculated predictions of k_{eff} and CB obtained in this present paper is based on the latest data of differential neutron-physics experiments. The feasibility of this accuracy has emerged because of the development of a system of group cross sections BNAB-78 [13], based on which the system of cross sections BNAB-MIKRO [14] was proposed, compiled from new estimates of the results of differential neutron data measurements. In parallel with the estimates of the most probable values of these data, their errors were also determined, which were represented in the form of a covariational matrix W of the group cross sections, i.e., in a form suitable for practical application. It is important to emphasize that the covariational matrix describes the accuracy of the group cross sections BNAB-MIKRO: the errors of the experiments themselves are taken into account in it, and it is on these errors that this system of cross sections has been compiled. The BNAB-78 system differs from the BNAB-MIKRO system by taking account of the results of macroexperiments. Its use stipulates a higher accuracy of the calculated results [14].

Translated from Atomnaya Énergiya, Vol. 49, No. 4, pp. 221-224, October, 1980. Original article submitted January 22, 1980.

0038-531X/80/4904-0669$07.50

TABLE 1. Errors and Correlation Coefficients (× 100) of the Group Values of $\alpha^{235}U$

Energy limits	Error, %	No. of group	No. of group: 1 2 3 4 5 6 7 8 9 10 11 12
2,5–10,5 MeV	50,0	1	100
1,4–2,5	20,0	2	0 100
0,4–1,4	12,0	3	0 0 100
0,2–0,4	9,5	4	0 0 80 100
0,1–0,2	9,0	5	0 0 75 80 100
46,5–100 keV	8,5	6	0 0 70 75 80 100
21,5–46,5	8,0	7	0 0 60 70 75 80 100
10–21,5	7,5	8	0 0 55 60 70 75 80 100
4,65–10	7,0	9	0 0 30 30 30 30 50 70 100
2,15–4,65	6,5	10	0 0 0 0 0 30 50 70 100
1–2,15	6,5	11	0 0 0 0 0 10 40 70 70 100
0–1	6,0	12	0 0 0 0 0 0 10 40 70 70 70 100

TABLE 2. Errors and Correlation Coefficients (× 100) of the Group Values of $\alpha^{239}Pu$

Energy limits	Error, %	No. of group	No. of group: 1 2 3 4 5 6 7 8 9 10 11 12
2,5–10,5 MeV	50,0	1	100
1,4–2,5	20,0	2	0 100
0,4–1,4	17,0	3	0 0 100
0,2–0,4	10,0	4	0 0 80 100
0,1–0,2	9,5	5	0 0 75 80 100
46,5–100 keV	9,0	6	0 0 70 75 80 100
21,5–46,5	8,5	7	0 0 60 70 75 80 100
10–21,5	8,5	8	0 0 55 60 70 75 80 100
4,65–10	8,0	9	0 0 30 30 30 30 50 70 100
2,15–4,65	8,0	10	0 0 0 0 0 0 30 50 70 100
1–2,15	7,5	11	0 0 0 0 0 0 10 40 70 70 100
0–1	7,5	12	0 0 0 0 0 0 10 40 70 70 70 100

When compiling the covariational matrix W, data about the structure of the measurement errors given by the authors of the experimental papers were taken into account; an analysis was carried out of the possible errors of some or other methods used for measurements of a given type of cross section in a given energy region. The reality of the estimates of the errors of individual experiments was monitored by the spread of the results obtained by different authors. Particular attention was paid to the estimate of the error correlations of the estimated data. As examples, the estimates of the errors in the cross sections of ^{238}U in the region of forbidden resonances [15] may be quoted, and also the estimates of the errors in the group values of $\alpha = \sigma_c/\sigma_f$ for ^{235}U and ^{239}Pu [16, 17].

The covariational matrix of the errors is compiled for the cross sections of all reactions of the principal materials of the core of fast reactors – ^{235}U, ^{238}U, ^{239}Pu, ^{240}Pu, ^{241}Pu, Fe, Cr, Ni, Na, O, C. For ^{238}U, ^{239}Pu, ^{240}Pu, and ^{241}Pu, in addition to the matrix of errors in the fission cross sections, a matrix was compiled of the errors in the ratios of the fission cross sections to the fission cross section of ^{235}U, as the results of these very ratios were used as the basis for compiling the group cross sections. It was assumed that the errors of these ratios are independent. For this same reason, in addition to the errors in the capture cross sections, for ^{235}U, ^{239}Pu, and ^{241}Pu the errors in the values of $\alpha = \sigma_c/\sigma_f$ were estimated. As an illustration of the matrix W, Tables 1 and 2 show the errors (standard deviations) and correlation coefficients of the group values of α for ^{235}U and ^{239}Pu.

When compiling the covariational matrix W, the errors associated with the imprecise knowledge of the spectrum of nonelastically scattered neutrons and the fission spectrum were not taken into account. We related the errors associated with multigroup approximation (such as the indeterminacy of the moderation cross sections) to the category of procedural errors and were also not taken into account (their effect was considered, e.g., in [18]). The errors in estimating the self-shielding cross sections were considered only for the ^{238}U cross sections, for which self-shielding is particularly large. For the structural materials and the fissile isotopes, the indeterminacies of the deviation of the self-shielding factors from unity are quite large, however, the effects of self-shielding of the fission cross sections are not so large that they will appear in the conclusions of the present paper.

The estimates of the accuracy of the calculated predictions of the criticality and breeding parameters are given by the example of a two-dimensional test model of a large plutonium power breeder-reactor suggested in [19]. The sensitivity coefficients of k_{eff}, CB, and CBC (breeding coefficient in the reactor core) were calculated by means of the two-dimensional TVK-2D [20] program complex, based on the generalized theory of perturbations [21, 22]. The homogeneous and nonhomogeneous direct and adjoint equations of generalized perturbation theory in the TVK-2D complex are solved in the diffusion approximation, for which the applicability for large-sized fast reactor calculations is substantiated by the many tests. The diffusion equation in RZ-geometry is solved by means of iteration network methods: in the internal iterations the methods of partial factorization and variable paths are used in order to accelerate the convergence; the external iterations are accelerated by the method of two-layer Chebyshev extrapolation. The accuracy of the internal iterations is set to the optimum dependence on the accuracy of the external iterations. The calculations are carried out with a local criterion of accuracy of the fluxes and importances equal to ~0.01%. The TVK-2D complex was included in the NF-6 program systems [22], by means of which control is effected in the computation process and, in particular, the 26-group constants are prepared (based on the BNAB-78 cross sections).

TABLE 3. Coefficients of Sensitivity of k_{eff}, CB, and CBC, and the Components of Their Errors Due to Indeterminacy of the Group Cross Sections

Type of group cross section σ	Sensitivities $\frac{\partial F}{F}/\frac{\partial \sigma}{\sigma}$					Component errors, %		
	k_{eff}	CB	CB_x	CBC	CBC_x	k_{eff}	CB_x	CBC_x
σ_f^9/σ_f^5	0,42	−0,80	−0,04	−0,83	−0,04	0,7	0,4	0,4
σ_f^{41}/σ_f^5	0,14	−0,20	−0,06	−0,22	0,07	1,0	0,5	0,5
σ_f^8/σ_f^5	0,08	0,01	0,16	0	0,16	0,1	0,2	0,2
σ_f^{40}/σ_f^5	0,03	0	0,05	0	0,05	0,1	0,2	0,2
σ_f^5	0,67	−0,99	0,20	−1,05	0,21	0,8	0,6	0,6
α^9	−0,04	−0,16	−0,23	−0,17	−0,25	0,3	1,5	1,6
α^{41}	0	−0,03	−0,03	−0,03	−0,03	0	0,5	0,6
σ_c^8	−0,26	0,68	0,22	0,80	0,32	1,4	1,4	1,5
σ_c^{40}	−0,02	0,07	0,02	0,08	0,04	0,2	0,2	0,3
σ_c^{ock}	−0,02	0	−0,03	0	−0,04	0,4	0,6	0,8
σ_c^{ct}	−0,01	0	−0,05	0	−0,05	0,2	1,0	1,0
σ_{in}^8	−0,06	0,01	−0,09	0,05	−0,06	0,7	1,2	0,9
σ_{in}^{Na}	−0,01	0	−0,01	0,01	−0,01	0,2	0,4	0,3
σ_{in}^{ct}	−0,02	0	−0,04	0,01	−0,03	1,0	1,2	1,0
σ_e^{16O}	−0,07	0,01	−0,11	0,07	−0,06	0,1	0,1	0,1
σ_e^{Na}	−0,02	−0,02	−0,04	0,01	−0,02	0,2	0,3	0,2
σ_{tr}^8	0,03	−0,07	0	0	0,06	0,1	0	0,2
σ_{tr}^{16O}	0,03	−0,06	0	0	0,05	0,1	0	0,2
σ_{tr}^{Fe}	0,02	−0,03	0	0	0,04	0,1	0	0,2
ν^9	0,64	−0,02	1,12	0,01	1,22	0,6	1,1	1,2
ν^{41}	0,18	0	0,32	0	0,35	0,3	0,6	0,6
ν^8	0,13	0,02	0,26	0	0,26	0,2	0,4	0,4
ν^{40}	0,04	0	0,08	0	0,08	0,1	0,2	0,2
			Total dispersion, %			6,4	11,6	12,0
			Total error, %			2,5	3,4	3,5

The dispersions of the reactor functions are determined by the formula $D_F = \mathbf{H}_F W \mathbf{H}_F^T$, where $\mathbf{H}_F$ is the column vector of the sensitivity of the functional $F(k_{eff}, CB, CBC)$ to variations of the group cross sections (Table 3 gives the coefficients of sensitivity to the group cross sections which make a marked contribution to the dispersion of the functionals k_{eff}, CB, and CBC). In order to illustrate the importance of compensation for noncriticality [24], Table 3 gives the sensitivities of CB and CBC, obtained both directly for an arbitrarily critical reactor and for the case of compensation for noncriticality, due to variation of the enrichment x: $H^{CB,CBC_x}(\sigma) = H_{CB,CBC}(\sigma) - H_{CB,CBC}(x)\, H_k(\sigma)/H_k(x)$. The components of CB and CBC were analyzed on the basis of "compensated sensitivities," as there is no sense in speaking about the accuracy of the calculation of CB and CBC for a noncritical reactor [24].

The estimates obtained for the error in the calculated prediction of CB and CBC proved to be more optimistic than those given in [2-12]: ~3.5% by comparison with 5-8%. An estimate of the error of the calculated prediction of k_{eff} also is somewhat higher: 2.5% by comparison with 3-5%. Based on the available experience of fast reactor and critical assembly calculations with different systems of constants, and carried out according to the systems of cross sections compiled in different countries [14], the accuracy estimate obtained for the calculation of k_{eff} is realistic. This can serve as an indirect confirmation also of the accuracy estimate obtained for the calculations of CB and CBC. In the reactor being considered, CB ≈ 1.4 and CBC ≈ 1, so that the estimated errors in absolute units amount to ± 0.050 for CB and ± 0.035 for CBC.

The principal source of errors in CB and CBC are the errors in α for ^{239}Pu, in the capture cross sections of the fission fragments and structural materials, in the value of ν, and also in the inelastic scattering cross sections. The latter at first glance may appear to be strange, but the significant effect of the indeterminacy in the inelastic scattering was revealed even earlier (see, e.g., [4]). When analyzing the errors in k_{eff}, a large contribution is observed from the inaccuracy of knowledge of the fission cross section of ^{241}Pu.

The accuracy of the calculated predictions of fast reactor characteristics can be increased in the following way (see Table 3):

a) a considerable part of the sources of error in calculating k_{eff} can be eliminated if the group cross sections, corrected by experiments on critical assemblies, are used in the calculations. However, the contribution of the errors in the cross sections of ^{241}Pu and of the fission products in this case are not eliminated and, consequently, the accuracy in the calculation of k_{eff} remains much worse than that required (~1.5% instead of 0.5%);

b) it is very essential to measure the fission cross section of ^{241}Pu with an accuracy of 3-5%. In order to obtain the differential data with the same accuracy, it is particularly helpful to take account of measurements of $\bar{\sigma}_f(^{241}Pu)/\bar{\sigma}_f(^{235}U)$ on critical assemblies;

c) measurements are necessary of α for ^{239}Pu in the spectra of fast power reactors with an accuracy of $\lesssim 3\%$ (there are no foundations for hoping to achieve this accuracy in measuring α in differential experiments). The refinement of α for ^{241}Pu in similar experiments also will be useful;

d) it is important to increase the accuracy of the inelastic scattering cross section measurements. The first step in this direction could be the measurements of the cross sections of withdrawal below the fission threshold of ^{238}U and ^{237}Np, or ^{240}Pu;

e) the contributions of the errors in the cross sections of the fission fragments can hardly be reduced without including macroscopic experiments on fast power reactors;

f) as before, it is necessary to increase the accuracy of ν;

g) an increase of accuracy of the average fission cross sections of ^{235}U, ^{238}U, and ^{239}Pu is no longer the immediate problem; however, experiments on transmission, which will allow the factors of the resonance self-shielding cross sections of fissile nuclei to be estimated directly, retain their urgency.

The conclusions obtained coincide with the recommendations of [3]. The clarification of the role of errors in the cross sections of ^{241}Pu and the inelastic scattering cross sections is new.

LITERATURE CITED

1. S. M. Zaritskii, M. N. Nikolaev, and M. F. Troyanov, in: Proceedings of the Conference "Neutron Physics" [in Russian], Naukova Dumka, Kiev, Part 1, (1972), p. 5.
2. L. N. Usachev and Yu. G. Bobkov, in: Proceedings of the Conference "Neutron Physics" [in Russian], Naukova Dumka, Part 2, (1972), p. 139.
3. M. N. Nikolaev, in: Proceedings of the Conference "Neutron Physics," TsNIIatominform, Moscow, Part 1, (1976), p. 5.
4. L. N. Usachev, V. N. Manokhin, and Yu. G. Bobkov, in: Proceedings of the IAEA Symposium "Nuclear Data in Science and Technology," Paris, 12-16 March 1973, Vol. 1, p. 129.
5. A. I. Voropaev et al., in: Problems of Nuclear Science and Technology. Series Nuclear Constants [in Russian], TsNIIatominform, Moscow, No. 25 (1977), p. 69.
6. A. I. Voropaev et al., in: Problems of Nuclear Science and Technology. Series Nuclear Constants [in Russian], Part 2, No. 20 (1975), p. 112.
7. P. Greebler et al., in: Proceedings of the IAEA Symposium "Nuclear Data for Reactors" Helsenki, 15-19 June 1970, Vol. 1, p. 17.
8. J. Chaudat et al., in: Proceedings of the International Symposium of Physics of Fast Reactors, Tokyo, 16-19 October, 1973, Vol. 3, p. 1207.
9. J. Rowlands et al., in: Proceedings of the International Symposium of Physics of Fast Reactors, Tokyo, 16-19 October, 1973, Vol. 3, p. 1133.
10. S. Yiftah et al., in: Proceedings of the International Symposium of Physics of Fast Reactors, Tokyo, 16-19 October 1973, Vol. 3, p. 1479.
11. J. Marable and C. Weisbin, Trans. Am. Nucl. Soc., 26, 542 (1977).
12. A. A. Van'kov, A. I. Voropaev, and L. N. Yurova, Analysis of a Reactor Physics Experiment [in Russian], Atomizdat, Moscow (1977).
13. L. N. Usachev and Yu. G. Bobkov, in: Proceedings of the Conference "Neutron Physics" [in Russian], Obninsk, Izd. FÉI, Part 1 (1974), p. 87.
14. L. P. Abagyan et al., At. Energ., 48, No. 2, 117 (1980).
15. G. N. Manturov and M. N. Nikolaev, in: Resonance Absorption of Neutrons [in Russian], TsNIIatominform, Moscow (1978), p. 175.

16. V. N. Kononov and E. D. Poletaev, see Ref. 5, p. 23.
17. V. A. Kon'shin, E. Sh. Sukhovitskii, and V. F. Zarkov, Preprint Institute of Heat and Mass-Exchange, Academy of Sciences, Minsk (1978).
18. M. A. Baryba et al., see Ref. 13, p. 175.
19. M. N. Zizin, L. N. Kudryashov, and M. N. Nikolaev, Preprint NIIAR, P-4(270), Dimitrovgrad (1976).
20. P. N. Alekseev, S. M. Zaritskii, and L. K. Shishkov, in: Nuclear-Physics Research in the Soviet Union [in Russian], Atomizdat, Moscow, No. 23 (1977), p. 30.
21. L. N. Usachev, At. Energ., 15, 6, 472 (1963).
22. L. N. Usachev and S. M. Zaritskii, in: Bulletin of the Information Center on Nuclear Data [in Russian], Atomizdat, Moscow, No. 2 (1965), p. 242.
23. M. N. Zizin, O. A. Savochkina, and O. P. Chukhlova, Preprint NIIAR, P-40(334), Dimitrovgrad (1977).
24. M. N. Nikolaev and B. G. Ryazanov, in: Problems of Nuclear Science and Technology. Series Nuclear Constants [in Russian], TsNIIatominform, Moscow, No. 17 (1974), p. 21.

DETERMINATION OF BURNUP AND ISOTOPE COMPOSITION FOR SPENT VVÉR-365 FUEL

A. V. Stepanov, T. P. Makarova, B. A. Bibichev, A. M. Fridkin, A. V. Lovtsyus, L. D. Preobrazhenskaya, A. A. Lipovskii, and A. N. Timofeev

UDC 546.791:539.173.8+546.799.4:621.039.516.22

The object of the present study was to determine the contents and isotopic compositions of the neodymium, uranium, plutonium, and transplutonium elements in specimens of VVÉR-365 fuel pins from the Novovoronezh nuclear power station and to examine the correlation between the ratios of the concentrations for certain nuclides on the one hand, and the burnup on the other.

Methods. Specimens of fuel with an initial enrichment of 3% in ^{235}U were prepared from the pins from two cassettes irradiated to different extents (Table 1). The disposition of the pins is shown in Fig. 1 (there were no absorbing elements in cassette DR-3 No. 80). Cassettes DR-3 No. 80 and PR-3 No. 223 were irradiated for 342 and 1032 days, respectively. During irradiation these cassettes were not adjacent to the reflector or to the cassette used in routine reactor power control. The cooling times before analysis were 3.5 years for DR-3 No. 80 and 4.5 years for PR-3 No. 223.

The fuel was dissolved in 8 M HNO_3. The uranium concentration was determined by potentiometric titration by the Davis–Gray–Eberle method with a semiautomatic instrument [1]. The plutonium concentration was found by isotope dilution of ^{238}Pu in combination with α spectrometry [2]. The isotopic compositions of these elements were determined with a mass spectrometer after chromatographic purification.

The neodymium and transplutonium elements were isolated from the solutions by the lanthanum fluoride method with subsequent separation by electrical migration for the rare-earth and transplutonium groups on Whatman 31 paper impregnated with EDTA [3]. The ^{148}Nd concentration, which acts as burnup monitor, was determined by isotope dilution of ^{142}Nd in combination with mass spectrometry. Then

$$N_{148} = N^s_{142}\,(R^m - H_1 - R^s)/1 - \frac{R^m - H_1 - R^s}{R^v H_2 - H_3}\,\frac{1}{M},$$

where N_{148} is the number of ^{148}Nd atoms in 1 g of solution, N^S_{142} is the number of atoms of the ^{142}Nd tracer added, R^m, R^v, R^S are the 148/142 isotope ratios in the neodymium fractions from the samples with the label, without the label, and in the label itself, respectively, M is the mass of solution used, and

$$H_1 = N_{142(\mathrm{nat})}/N^s_{142};$$
$$H_2 = N_{142(\mathrm{tot})}/N_{142(\mathrm{Pr})};$$
$$H_3 = N_{148(\mathrm{nat})}/N_{142(\mathrm{Pr})}$$

Translated from Atomnaya Énergiya, Vol. 49, No. 4, pp. 225-229, October, 1980. Original article submitted August 27, 1979; revision submitted March 18, 1980.

0038-531X/80/4904-0673$07.50

TABLE 1. Cassette Numbers, Pin Numbers, and Positions of Specimens along Height of Pins

Specimen No.	Cassette No.	Pin No.	Position along height of pin, mm
1	DR-3 № 80	98	125
2	DR-3 № 80	76	2125
3	DR-3 № 80	4	375
4	DR-3 № 80	4	1125
5	PR-3 № 223	107	50
6	PR-3 № 223	87	375
7	PR-3 № 223	76	375
8	PR-3 № 223	69	625
9	PR-3 № 223	69	1625

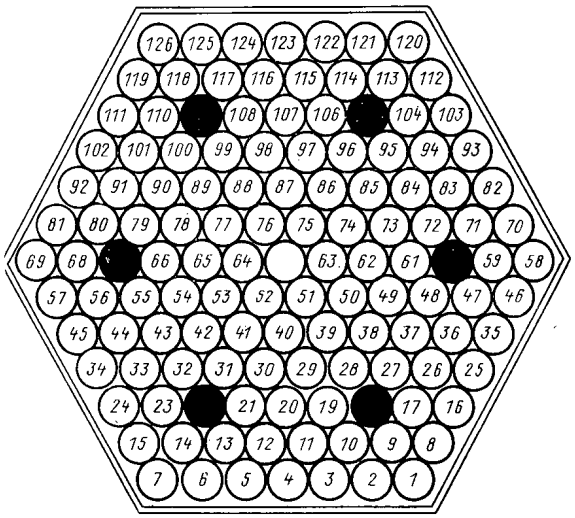

Fig. 1. Disposition of fuel pins in cassettes: ● absorbing elements.

are corrections that arise from contamination of the sample by natural neodymium and from the formation of ^{142}Nd in

$$^{141}\mathrm{Pr} \xrightarrow{n\gamma} {}^{142}\mathrm{Pr} \xrightarrow{\beta} {}^{142}\mathrm{Nd}.$$

The concentrations of the americium and curium nuclides were determined by α spectrometry. Thin-layer sources of these elements were produced electrolytically from the chlorides in solution in dimethysulfoxide using metallic substrates after the elements had been separated by electrical migration [4]. The chemical parameters of Am(III), Cm(III), and Eu(III) are similar, so it was possible to use ^{154}Eu and ^{244}Cm to estimate the chemical yields. The concentrations of these two in the initial solutions and in the transplutonium preparations were measured respectively by γ and α spectrometry. The ^{137}Cs concentration, which also acts as a burnup monitor, was determined on an aliquot fraction of the solution by γ spectrometry.

Results and Discussion. The burnup was determined by three methods: from the change in isotope composition in the heavy elements [3], from the accumulation of ^{148}Nd, and from the accumulation of ^{137}Cs. In the latter two cases, we used the weighted mean yields of ^{148}Nd and ^{137}Cs from the fission of ^{235}U, ^{239}Pu, and ^{241}Pu by thermal neutrons and from ^{238}U by fission neutrons [5]. The contribution of each fissile nuclide to the total number of fissions was found by the first method. The values of the cumulative yields of ^{148}Nd and ^{137}Cs for the above fissile nuclides were taken from [6].

Table 2 gives burnup values found by the three methods. The data are in agreement within the error of measurement.

Tables 3 and 4 give the isotope compositions and nuclide contents for uranium, plutonium, americium, and curium; for ^{241}Am we also give the content at the time of analysis.

TABLE 2. Burnup Determination in Pin Specimens from Various Methods at the 0.95 Confidence Level*

Specimen No.	Burnup, kg/ton U			
	from ^{148}Nd	from ^{137}Cs	from heavy-atom method	mean value
1	6,0 (1)	6,1 (1)	6,5 (3)	6,1 (1)
2	—	10,6 (2)	10,8 (3)	10,7 (2)
3	13,2 (3)	12,7 (2)	13,2 (4)	13,1 (2)
4	14,8 (3)	14,5 (2)	14,7 (4)	14,6 (2)
5	15,2 (2)	14,9 (2)	15,4 (4)	15,2 (2)
6	28,0 (6)	28,3 (5)	29 (1)	28,3 (5)
7	28,9 (5)	28,8 (5)	30 (1)	28,9 (5)
8	33,2 (5)	32,5 (6)	34 (1)	32,2 (5)
9	33,7 (6)	33,5 (6)	34 (1)	33,7 (6)

*Here and in Tables 3 and 4 the numbers in parentheses apply to the last significant figure and denote the confidence range.

TABLE 3. Plutonium Content and Isotope Composition of Uranium and Plutonium in Pin Specimens at the End of Irradiation at the 0.95 Confidence Level*

Specimen No.	Isotope composition, mass %									Content
	^{234}U	^{235}U	^{236}U	^{238}U	^{238}Pu	^{239}Pu	^{240}Pu	^{241}Pu	^{242}Pu	Pu, kg/ton U
1	0,0164 (8)	2,31 (1)	0,11 (6)	97,53 (6)	0,0732 (6)	87,33 (2)	9,73 (2)	2,715 (6)	0,151 (2)	3,10 (3)
2	0,023 (1)	1,974 (7)	0,202 (4)	97,80 (8)	0,183 (1)	79,79 (3)	13,62 (3)	5,861 (8)	0,542 (6)	5,22 (4)
3	0,0182 (5)	1,789 (8)	0,212 (2)	97,982 (8)	0,223 (2)	76,22 (6)	15,58 (7)	7,11 (1)	0,875 (3)	5,73 (3)
4	0,0187 (11)	1,66 (1)	0,236 (4)	98,09 (1)	0,256 (1)	73,92 (3)	16,77 (2)	7,90 (3)	1,15 (4)	6,18 (3)
5	0,0194 (6)	1,592 (8)	0,249 (2)	98,140 (8)	0,397 (3)	73,46 (2)	18,07 (2)	6,99 (1)	1,13 (2)	5,11 (4)
6	0,0154 (7)	0,845 (6)	0,382 (9)	98,76 (1)	1,050 (7)	59,08 (2)	22,82 (2)	12,62 (1)	4,42 (1)	9,11 (12)
7	0,0146 (4)	0,859 (5)	0,379 (3)	98,747 (6)	1,002 (4)	58,93 (2)	22,84 (2)	12,79 (1)	4,432 (5)	—
8	—	—	—	—	1,312 (8)	55,87 (1)	23,51 (1)	13,699 (8)	5,606 (6)	9,41 (15)
9	0,0145 (6)	0,647 (4)	0,996 (7)	98,943 (8)	1,361 (8)	55,25 (3)	23,89 (3)	13,52 (1)	5,96 (1)	9,64 (29)

*The plutonium content is referred to the uranium content in the spent fuel.

It is of interest to compare the observed contents of the main uranium and plutonium nuclides in the VVÉR fuel with calculations; Figs. 2 and 3 show the calculated amounts of these nuclides in relation to burnup for the VVÉR-365 cassettes with 3% fuel enrichment as determined by means of the POP program [7]. We also give the observed contents for these fuel pins derived here and in [8]. Figure 2 shows that the observed points lie systematically below the theoretical curves for ^{235}U but above the curves for ^{236}U. The mean deviations of the values found here for ^{235}U and ^{236}U were, respectively, 7.8 and 8.4%.

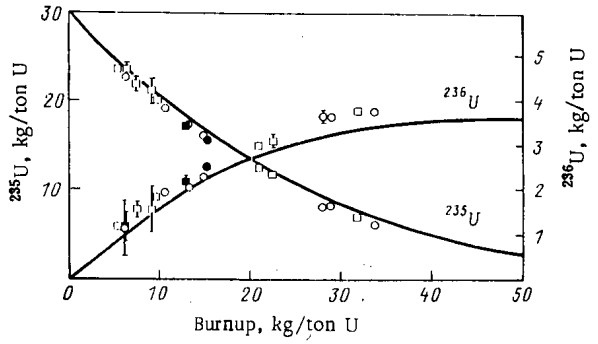

Fig. 2. Reduction in ^{235}U content and accumulation of ^{236}U in relation to burnup (○, ● our results; □, ■ results of [8]; ●, ■ end specimens, lines calculated from POP program).

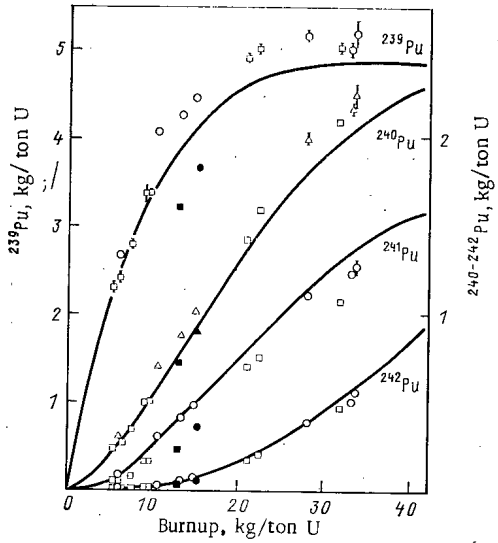

Fig. 3. Accumulation of Pu isotopes in relation to burnup (○, △, ●, ▲ our results; □, ■ [8]; ●, ▲, ■ end specimens; lines derived from POP program).

TABLE 4. Contents of Nuclides of Transplutonium Elements in Fuel Pins at the End of Irradiation at the 0.95 Confidence Level* in 10^3 kg/ton U

Specimen No.	^{241}Am		^{243}Am	^{242}Cm	^{244}Cm
	at time of analysis	at end of irradiation			
1	17,0 (2)	0,3	0,5 (2)	0,19 (2)	0,076 (7)
2	42 (3)	—	0,8 (2)	0,47 (4)	0,12 (1)
3	50 (4)	2	2,3 (4)	0,66 (7)	0,26 (8)
4	114 (4)	—	2,5 (5)	1,6 (1)	0,95 (4)
5	84 (6)	4	2,2 (5)	0,48 (5)	0,38 (3)
6	206 (13)	30	45 (8)	10,3 (9)	10.8 (6)
7	290 (20)	—	38 (8)	19,0 (1,5)	15,0 (7)
8	250 (30)	30	59 (13)	18 (2)	25 (2)
9	300 (10)	30	97 (17)	19 (1)	30 (1)

*The plutonium content is referred to the uranium content in the spent fuel.

Systematic deviation was also characteristic of the plutonium isotopes (Fig. 3); the observed points at burnup more than 10 kg/ton U lie systematically above the theoretical curves for ^{239}Pu and ^{240}Pu but below the curves for ^{241}Pu and ^{242}Pu. The exception is represented by two specimens from the end parts of the fuel pins. The mean deviations for ^{239}Pu and ^{240}Pu for all specimens considered here (except the end specimens) are, respectively, 9.3 and 10.3%. The content of ^{239}Pu in the end specimens was considerably less than the theoretical value, which may be explained at least partially by the softening of the neutron spectrum at the boundary of the core in the VVÉR-365, which is not incorporated into the POP program. This program uses an asymptotic approximation to calculate the burnup and nuclide composition. The systematic discrepancies for uranium and plutonium could be reduced substantially by modifying the effective cross sections used in POP by the method of [8]. Also, the spread in the observed points exceeds the error of experiment for closely similar values of the burnup for the plutonium and transplutonium nuclides. This spread may be due to local variations in the neutron spectrum from one fuel pin to another. Also, there may be some error in determining the burnup, since there is a power-law relationship between the contents of the transplutonium elements and the burnup.

The data also allow one to examine the correlation between the burnup and the concentration ratios for certain nuclides, or else the correlation between the concentration ratios for two pairs.

A correlation of the first type may be described by a straight-line regression equation:

TABLE 5. Values for the Parameters in Regression Equation (3) and Relative Standard Deviations S_r

R	a	k	$S_r(a)$, %	$S_r(k)$, %
[240Pu]/[239Pu]	0,79	—1,57	2,5	1,3
[242Pu]/[241Pu]	1,23	—2,26	3,2	2,2
[242Pu]/[238U]	2,62	—7,30	3,4	4,1
[240Pu]/[238U]	1,04	—4,20	3,8	4,81
[242Pu]/[240Pu]	1,59	—3,00	2,5	3,3
[243Am]/[242Pu]	1,4	—3,0	14,3	3,0
[243Am]/[242Pu]	4,0	—10,2	5,0	27,5
[242Cm]/[238U]	3,5	—10,8	11,4	14,8
[244Cm]/[238U]	4,7	—11,8	4,3	6,8
[244Cm]/[243Am]	0,7	—1,6	4,3	43,8

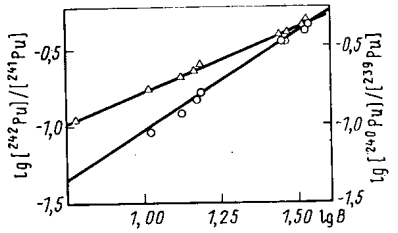

Fig. 4

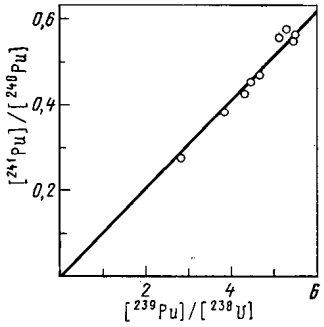

Fig. 5

Fig. 4. Relationship between the logarithms of the concentration ratios [242Pu]/[241Pu] (○) and [240Pu]/[239Pu] (△) and the logarithm of the burnup.

Fig. 5. Relation between [241Pu]/[240Pu] and [239Pu]/[238U].

$$\lg R = k + a \lg B, \tag{3}$$

where R is the concentration ratio for the pair of isotopes, B is the burnup in kg/ton, and *a* and k are regression parameters.

A correlation of the second type is described by

$$R_y = mR_x + c, \tag{4}$$

where R_y and R_x are the concentration ratios for the pair of isotopes and m and c are regression parameters.

Several regression equations of the type of (3) and (4) were drawn up from the data of Tables 3 and 4 together with the scheme for the accumulation of transuranium nuclides in the VVÉR fuel. Tables 5 and 6 give the parameters in these equations as derived by least-squares fitting. Figures 4 and 5 show several examples of correlations of the type of (3) and (4).

Conclusions. The values for the burnup in the VVÉR-365 pins determined by heavy-atom methods and from the accumulation of 148Nd and 137Cs are in agreement within the error of measurement. This shows that there is no appreciable migration of 137Cs in the fuel in this reactor.

TABLE 6. Parameters of Correlations of the Form of (4) and the Average Standard Deviations S_r

R_y	R_x	m	c	$s_r(m)$, %	$s_r(c)$, %
[241Pu]/[240Pu]	[239Pu]/[238U]	104	0	1,15	5
[236U]/[238U]	$([^{235}U]_0-[^{235}U])/[^{238}U]$	0,17	0,014	3,7	80
$1-[^{239}Pu]/\Sigma Pu$	$([^{235}U]_0-[^{235}U])/\Sigma$ [U]	19,4	0,3	2,1	1,9
Σ [Pu]/Σ [U]	$([^{235}U]_0-[^{235}U])/\Sigma$ [U]	4,0	12,6	13,6	18,2

The observed and calculated levels of the main nuclides of uranium and plutonium in the VVÉR-365 fuel show systematic discrepancies, which could evidently be substantially reduced by modifying the basic effective cross sections. This will require further experimental data on the isotope composition of VVÉR fuel.

Typical linear or logarithmic relationships are derived between the burnup and the ratios for certain nuclides of uranium, plutonium, and the transplutonium elements for the VVÉR-365 fuel. These relationships apply for the entire range of burnup from 6 to 35 kg/ton U.

LITERATURE CITED

1. M. V. Ryzhinskii et al., Zh. Anal. Khim., 33, No. 3, 499 (1978).
2. A. A. Lipovskii and Yu. V. Khol'nov, in: Proc. Symp. Safeguarding Nuclear Materials, Vol. 2, Vienna, JAEA-SN-201/65, 165 (1976).
3. T. P. Makarova, A. V. Stepanov, and Z. G. Gritchenko, Isotopenpraxis, 12, No. 11, 424 (1976).
4. T. Handbey and Y. Cooper, Anal. Chem., 41, No. 2, 381 (1969).
5. V. Ya. Gabeskiriya, V. V. Gryzina, and Yu. B. Novikov, At. Energ., 43, No. 4, 240 (1977).
6. M. Meek and B. Rider, NEDO-12154-1 (1974).
7. V. N. Sidorenko and E. D. Belyaeva, IAE-1171 Preprint, Moscow (1966).
8. Yu. B. Novikov, V. Ya. Gabeskiriya, and M. N. Maslennikova, At. Energ., 43, No. 4, 278 (1977).
9. J. Luffin, Z. Szatmary, and J. Vanuxcem, J. Nucl. Energy, 26, 627 (1972).

USE OF CARBON STEEL WITH UNMODIFIED WATER TREATMENT AT THE VK-50 NUCLEAR POWER STATION

A. I. Zabelin, A. B. Andreeva,
V. M. Eshcherkin, L.N. Stupina,
A. S. Kornilov, V. E. Shmelev,
and Yu. V. Chechetkin

UDC 621.039.53

It is becoming more important to use carbon steel in the main loops of nuclear power stations, but although there have been many laboratory and testbed studies [1] that indicate high reliability of carbon steel in water and steam containing oxygen, so far there has been no agreed view on the scope for replacing very scarce stainless steel by carbon steel in nuclear power stations, in spite of experience here and abroad with power systems based on organic fuel.

In that respect, experience with the VK-50 nuclear power station represents a unique industrial experiment on the use of carbon steel in circulation loops for pressurized-water reactors. The results after tests lasting 100,000 h indicate high reliability in carbon steel in the steam section of the loop. On the other hand, experience with some thermal power stations, particularly the Konakovo one, show that there is adequate corrosion resistance in carbon steel when the oxygen level is less than 200 μg/kg in the condensate-feed tract, and the same applies to results obtained in the year after commissioning of the VK-50 nuclear power station.

We give below results on the water chemistry, corrosion-resistance of carbon steel, and stability of protective films on pipelines in the main circulation loop for the VK-50.

The circulation cycle in the main loop in the VK-50 is as follows. The saturated steam produced in the reactor passes via the high-pressure separator and low-pressure separator directly to the AK-70-13 turbine. The condensate from the used steam is transferred by condensate pumps via two stages of low-pressure heaters to a deaerator of atmospheric type (pressure 0.12 MPa, temperature 377°K). The deaerated condensate is passed by high-pressure feed pumps to the reactor and to the control-rod cooling mechanism.

The bodies of the separators, the steam pipelines, the bodies of the condensers, the condenser pipelines, the bodies of the low-pressure heater and deaerator are made of carbon steels of types 20, 22K, and 3, and these together constitute 32.8% of the total surface in the loop.

Translated from Atomnaya Énergiya, Vol. 49, No. 4, pp. 229-232, October, 1980. Original article submitted January 7, 1980.

0038-531X/80/4904-0678$07.50

TABLE 1. Contents of Corrosion Products (μg/kg) in Coolant in Unmodified Treatment (I) and Oxygen Treatment (II) as Indicated by Data of December 1, 1979

Coolant	Iron		Copper		Zinc	
	I	II	I	II	I	II
Feed water (without condensate purification)	14	5	15	5	20	2
Reactor water	22	10	30	20	25	3

The VK-50 was commissioned on 15 October 1965, and it operated with the addition of hydrazine hydrate to the water, but within a short period (on 2 November 1965) it was found that this was unsuitable for the pipe systems in the turbine condensers, the low-pressure heaters, and the other heat exchangers, which are made of brass [2]. Therefore, there was subsequently no water treatment.

The operating modes of the main equipment had not been evaluated, and this lead to frequent long intervals of downtime, while there were also remains of installation contaminants, which meant that the water-chemistry parameters were unstable during the early years. As the loop became run in and the equipment was adjusted and servicing was upgraded, the parameters gradually improved, and there was essential stability from about 1968-1969.

The state of the surfaces in the main loop after the first 3 years of operation was satisfactory, without signs of progressive corrosion of the carbon steel. At that time, electron diffraction revealed the presence of protective oxide films consisting of magnetite Fe_3O_4 and maghemite γ-Fe_2O_3 [3].

The corrosion response of the pipelines after 100,000 h of operation (at the end of 1977) characterizes the operation of the system with unmodified water.

Neutral oxygen conditions were used from July 1978, with a controlled addition of oxygen to the condensate-feed tract to a concentration of 200 μg/kg. A period of about 8000 h of operation in this mode showed that there was an appreciable tendency for the concentrations of the corrosion products to fall by comparison with the unmodified water (Table 1).

During the operation of the nuclear power station, no measures were taken to protect the equipment and pipelines when the reactor was shut down. About 34.8% of the total time was taken up by routine servicing or major modifications.

The state of the materials in the loop was examined at the start of 1978 by cutting meter sections of the pipes with welded joints from the following sections of the loop:

1) the steam pipeline between the high-pressure and low-pressure separators (steel 20, diameter 325 × 10);

2) the condensate pipeline after the low-pressure feed pump (steel 20, diameter 325 × 8); and

3) the pipeline before the feed pump (steel 3 kp, diameter 425 × 5).

The tube specimens were examined for the state of corrosion, nature of the deposits, mechanical parameters, and preservation of the protective properties of the oxide films formed under working conditions.

Standard specimens for mechanical and metallographic examinations were taken from the main metal and the welded joints in accordance with the existing standards [4] and All-Union State Standard (GOST) 6996-66.

Steam Pipe after the High-Pressure Separator. The oxide films formed under working conditions (pressure 2.5 MPa, temperature 497°K, oxygen concentration up to 30 mg/kg) were dense and adhered well to the metal. Electron diffraction showed that the films consisted of maghemite γ-Fe_2O_3 and magnetite Fe_3O_4, which are [5] protective.

The thickness of the layer of metal corroded in 100,000 h of operation was 70-150 μm, which corresponds to 3-4 points on the resistance scale (very stable or stable) in accordance with GOST 13819-68. A distinctive feature of the corrosion of steel 20 in this oxygenated steam over this long period is the absence of deep pitting, which was characteristic of the initial period, and which latterly was replaced mainly by general corrosion (Fig. 1a).

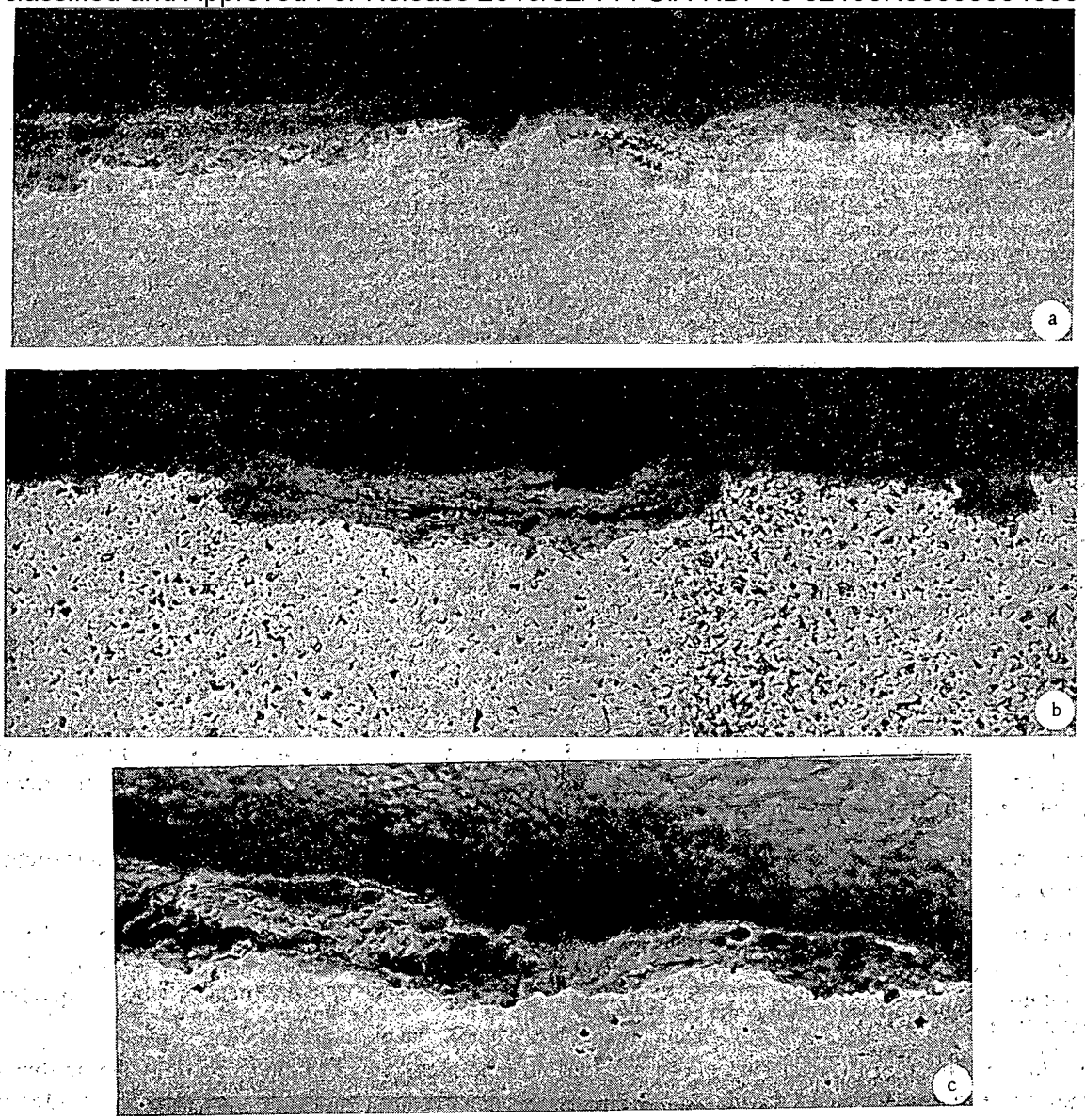

Fig. 1. States of the surfaces of steam pipe (a), condensate pipe (b), and feed pipe (c) after 100,000 h of operation (× 200).

Condensate Pipe. The medium is a condensate from turbine steam at 305°K containing oxygen at the level of 50 μg/kg. The corrosion products on the steel 20 were friable and readily detached, and they consisted mainly of magnetite Fe_3O_4 and hematite α-Fe_2O_3. The corrosion was of pitting type, with the depth of the pits about 300 μm (Fig. 1b). The corrosion resistance was estimated at 4–5 points.

Feed Water Pipe. The steel 3 kp showed mainly uniform corrosion; the thickness of the corroded layer was about 200 μm (Fig. 1c). The corrosion resistance was 4 points. As in the condensate pipes, the surfaces were covered with products formed mainly of magnetite and hematite.

Mechanical Parameters: the sections of the pipe were evaluated from tests on small specimens cut from the main metal and welded joints.

There were no substantial deviations from the requirements of GOST 5520-69 in the metal from either type of specimen after this long period of use.

Reference Specimens Tested in Oxygen. Measurements were made on indicator specimens of carbon steel in the condensate pipeline before the deaerator (condensate temperature 360°K, oxygen content about 200 μg/kg); the corrosion after 8000 h of tests was mainly uniform. The corrosion rate was 0.03–0.05 mm/yr (resistance 4 points), and the loss of corrosion products was not more than 0.01 $g/m^2 \cdot day$.

The corrosion products formed in the condensate tract with oxygen treatment consisted of a mixture of γ-Fe_2O_3 (maghemite), monoclinic Fe_2O_3, and orthorhombic α-$Fe_2O_3 \cdot H_2O$; the presence of maghemite, which is protective, is due to the elevated oxygen content in the condensate.

Stability of Iron Oxides during Shutdown: this was examined to determine the protective properties of the oxides. The tests were performed on specimens that had been in the steam pipelines for 12,500 h and which were then kept under conditions simulating shutdown.

It was found that the stability of the oxides was dependent on the formation conditions. For example, the oxides formed in wet steam containing oxygen (part of the steam pipe between the high-pressure and low-pressure separators, water content of steam 2 mass %) consisted mainly of maghemite, and this retained its phase composition for about 4000 h.

On the other hand, the oxides formed in dry steam (main steam pipe, water content 0.02-0.1 mass %) changed in phase composition within 2400 h. The proportion of maghemite in the oxide film was lower than that in the previous case, and it was transformed to friable hematite with poor adhesion.

This difference in stability of the oxide film is evidently related to the water content of the medium; stable maghemite γ-Fe_2O_3 can be formed only in the presence of a sufficient amount of water [6], which enters the lattice of the oxide (0.5-1.0 mass %).

Consequently, the medium in the steam pipes between the high-pressure and low-pressure separators is more favorable to the formation of oxide films containing stable maghemite than is the medium in the pipes after the low-pressure separator.

The stability of the oxide films during shutdown showed that the steam pipes in this pressurized-water require no protection for shutdown periods up to three months.

The conclusions are as follows:

1) the corrosion state of carbon steels in the main loop of the VK-50 nuclear power station is satisfactory after 100,000 h of operation;

2) the oxide films formed under working conditions on the surfaces of the steam pipe provide constant protection to the metal during operation and also during shutdown for periods of 2400-4000 h;

3) preliminary results on the corrosion with the addition of oxygen for about 8000 h of operation indicate reduced corrosion in the carbon steel in the condensate-feed tract, as is evident from the reduced amount of corrosion products in the coolant and the production of maghemite in the oxide films, which is protective; and

4) the results confirm recommendations on the extended use of carbon steel as a major material in the circulation loops for nuclear power stations, thermal power stations, and combined heat and power stations.

LITERATURE CITED

1. K. A. Nesmeyanova, At. Energ., 29, No. 2, 86 (1970).
2. A. I. Zabelin et al., in: Water Conditions in Pressurized-Water Reactors, Radiation Monitoring of Coolants, and Means of Reducing Radiation Hazard [in Russian], Berlin, VVB Kraftwerksanlagenbau, (1968), p. 72.
3. A. I. Zabelin et al., ibid, p. 105.
4. Rules for Safe Operation of Equipment in Nuclear Power Stations at Experimental and Research Reactors and Systems [in Russian], Metallurgizdat, Moscow (1973).
5. M. Bloom and R. Goldenberg, Corrosion Sci., 5, 623 (1965).
6. S. Sawocka and W. Pearl, in: Proc. Transactions of the International Water Conference Pittsburg, April 1971, Vol. 33, p. 67.

SPUTTERING OF THIN METALLIC FILMS BY FISSION FRAGMENTS

I. S. Bitenskii

UDC 539.211:546.79

While studying the sputtering of gold by ^{252}Cf fission fragments, it was discovered [1] that the sputtering coefficient for a massive gold foil constitutes 13 atoms/fragment, while for a fine-grained gold film on glass and platinum, this coefficient equals 240 and 3,000 atoms/fragment, respectively. Such a high value for the sputtering coefficient of fine-grained films can be explained, first of all, by the inelastic interaction between the fragment and the atoms in the solid, since elastic losses constitute only several percent of the total energy loss by the fragment and, second, by the presence of a large number of defects in the fine-grained film. A similar situation occurs with the formation of fission fragment tracks: tracks are not observed in ideal metals, while in fine-grained films, defects exist along the trajectory of the fragment [2].

The change in the properties of the metal with the passage of a fission fragment was examined [3] on the basis of the θ-spike model. In this model, as a result of the interaction of the fission fragment with the electronic subsystem, the temperature of the latter greatly increases. Furthermore, as a result of the interaction between the electronic and ionic subsystems, energy is transferred to the ionic subsystem, but due to the large relaxation time, the temperature of the lattice cannot increase by more than 100°K. However, in a nonuniformly deposited film, due to the large number of defects, the mean free path with respect to electron–phonon interactions decreases [4], which can increase the energy transfer to the ionic subsystem and, as a result, increase the temperature of the lattice above the melting temperature. Atoms, escaping from the hot spot (θ-spike) that is formed, contribute to the sputtering coefficient together with the atoms that sputter as a result of the development of a cascade of elastic collisions.

In what follows, an expression based on the θ-spike model is introduced for the sputtering coefficient of a metallic film, and the properties of the angular distribution of the sputtered atoms is also examined in the case of self-sputtering of a fine-grained film.

Calculation of the Sputtering Coefficient. The lattice temperature T and the electronic temperature T_e are determined from the system of heat-conduction equations [3]

$$C_e = \frac{\partial T_e}{\partial t} = \varkappa_e \Delta T_e - \alpha (T_e - T);$$
$$C_j = \frac{\partial T}{\partial t} = \varkappa_j \Delta T + \alpha (T_e - T), \tag{1}$$

where $C_e(C_j)$ is the heat capacity of the electronic subsystem (lattice); $\varkappa_e$ ($\varkappa_j$) is the electronic (phonon) thermal conductivity. The heat-transfer coefficient from the electrons to the lattice equals [5]

$$\alpha = \frac{\pi^2 m s^2 n}{6 \tau_0 T_D}, \tag{2}$$

where T_D is the Debye temperature; τ_0, mean free flight time for $T = T_D$; s, speed of sound; n, number of free electrons per unit volume; m, mass of an electron. We will write the initial temperature distribution of the electrons in the form

$$T_e(\rho, 0) = \frac{q}{\pi C_e \rho_e^2} \exp(-\rho^2/\rho_e^2). \tag{3}$$

Here, $q = dE/dx$ is the ionization loss of the fragment; ρ_e is a phenomenological parameter, characterizing the spatial temperature distribution, which must be much greater than the mean free path with respect to electron–electron collisions. We will assume that the initial temperature of the lattice equals zero. Applying the Laplace and Fourier transforms to system (1), we obtain the following solution for the lattice temperature:

$$T(\rho, t) = \frac{\alpha q}{2\pi C_e C_j} \int_0^\infty \frac{\exp(-\omega_1 t) - \exp(-\omega_2 t)}{\omega_2 - \omega_1} \exp\left(\frac{-k^2 \rho_e^2}{4}\right) J_0(k\rho)\, k\, dk, \tag{4}$$

where $J_0(x)$ is the zeroth-order Bessel function;

Translated from Atomnaya Énergiya, Vol. 49, No. 4, pp. 232-236, October, 1980. Original article submitted September 28, 1979.

0038-531X/80/4904-0682$07.50

$$\omega_{1,2}=\frac{1}{2}\left\{(\chi_e+\chi_j)k^2+\alpha\left(\frac{1}{C_e}+\frac{1}{C_j}\right)\mp\sqrt{\left[(\chi_e-\chi_j)k^2+\alpha\left(\frac{1}{C_e}-\frac{1}{C_j}\right)\right]^2+\frac{4\alpha^2}{C_eC_j}}\right\};\tag{5}$$

χ_e (χ_j) is the thermal diffusivity of electrons (lattice). We note the factor $1/4$ in the exponent of the integrand in (4), which was absent in the solution obtained previously [4].

The number of atoms, escaping per unit surface area of the hot spot per unit time, found by integrating the energy distribution function for the evaporated atoms [6], has the form

$$N=n\left(\frac{8kT}{\pi M}\right)^{1/2}\exp(-E_b/kT),\tag{6}$$

where M is the mass of an atom in the lattice; E_b is the surface bonding energy. We obtain the thermal sputtering coefficient by integrating Eq. (6) with respect to the polar coordinates and time:

$$S=4n\left(\frac{2k\pi}{M}\right)^{1/2}\int T^{1/2}\exp(-E_b/kT)\,\rho\,d\rho\,dt,\tag{7}$$

where the function $T(\rho, t)$ is determined by the expression (4).

For $\rho=0$ and some time $t=t_{max}$, the temperature $T(\rho, t)$ attains a maximum value T_{max} [4]. The surface bonding energy E_b is of the order of several electron volts and, as will be shown below, $E_b/kT_{max}\gg1$, so that by applying the method of steepest descents to the integral (7), we obtain the following expression for the sputtering coefficient:

$$S=\frac{8n\pi k^2T_{max}^{7/2}}{M^{1/2}E_b^{3/2}A^{1/2}B}\exp(-E_b/kT_{max}),\tag{8}$$

where $A=|\partial^2T/\partial t^2|$, $B=|\partial^2T/\partial\rho^2|$ are the parameters in the series expansion of the function $T(\rho, t)$ near the maximum. In order to compute the coefficients A and B, we will transform Eq. (4) by substituting the variable $z=(\chi_eC_e/\alpha)\,k^2$ and introducing new dimensionless variables $\tau=(4\chi_e/\rho_e^2)\,t$ and $\xi=2\rho/\rho_e$. Defining $T_0=q/\pi C_j\rho_e^2$, $\beta=\alpha\rho_e^2/4\chi_eC_e$, $\gamma_1=\chi_j/\chi_e$, $\gamma_2=C_e/C_j$, and $\gamma=\gamma_1+\gamma_2$, we obtain for small values of the parameters β, γ_1, and γ_2, the expression

$$T(\xi,\tau)=T_0\beta\int_0^\infty\frac{\exp(-\gamma\beta\tau z)-\exp[-(z+1)\beta\tau]}{z+1+\gamma}\exp(-\beta z)\,J_0(\xi\sqrt{\beta z})\,dz.\tag{9}$$

It can be shown that the root of the equation for the maximum value of the function $T(0, \tau)$ is determined by the equation

$$\tau_{max}=\begin{cases}1/\sqrt{\gamma\beta} & \text{for}\quad \beta\ll\gamma;\\ 1/\beta & \text{for}\quad \beta\gg\gamma.\end{cases}\tag{10}$$

Substituting Eq. (10) into (9), we find the maximum value of the temperature

$$T_{max}=\begin{cases}T_0\beta\ln(1/\gamma) & \text{for}\quad \beta\ll\gamma;\end{cases}\tag{11a}$$

$$\begin{cases}T_0\beta\ln(1/\beta) & \text{for}\quad \beta\gg\gamma.\end{cases}\tag{11b}$$

We note that the value of T_{max}, determined only by formula (11b), was presented in [4] without proof. Using the second derivative of Eq. (9), taking into account expression (10) at the maximum point and using the fact that $A=16\chi_e^2/\rho_e^4\,|\,\partial^2T/\partial\tau^2\,|$ and $B=4/\rho_e^2\,|\,\partial^2T/\partial\xi^2\,|$, we obtain from Eq. (8) the final expression for the sputtering coefficient:

$$S=\begin{cases}S_0\beta^{3/4}\gamma^{1/4}[\ln(1/\gamma)]^{7/2}\exp(-E_b/kT_{max}) & \text{for}\quad \beta\ll\gamma;\\ S_0\gamma[\ln 1/\beta)]^{7/2}\exp(-E_b/kT_{max}) & \text{for}\quad \beta\gg\gamma,\end{cases}\tag{12}$$

where $S_0=nk^2q^2c_1/\pi M^{1/2}E_b^{3/2}C_j\chi_e$ and c_1 is a constant of the order of unity.

The heat-conduction equations (1) do not take into account energy losses due to radiation and thermionic emission of electrons, but these heat losses from the hot spot can be neglected [7]. In the temperature range being considered, such parameters of the electron gas as the thermal conductivity and heat capacity cannot be assumed to be independent of temperature and it is necessary to use and to solve numerically the nonlinear equations of heat conduction, as in the calculation [7] of the energy distribution of electrons in thermionic emission from the hot spot with the passage of a fission fragment through metal. The sputtering coefficient

that we are examining is an integral characteristic and for estimates, apparently, it is possible to use the linear equation (1) with some average values for the thermal parameters.

Using Eq. (2) to determine the heat-transfer coefficient from the electrons to the lattice with $\tau_0 \approx 10^{-14}$ sec, $T_D = 165°K$, $S \approx 4 \cdot 10^3$ m/sec, $n = 6 \cdot 10^{28}$ m^{-3}, we obtain $\alpha \approx 10^{18}$ J/m^3 · sec · deg. Assuming $\varkappa_e \approx 40^6$ J/m · sec · deg, $\varkappa_j = 1.4^5$ J/m · sec · deg [8], $\rho_e = 4 \cdot 10^{-9}$ cm, $C_e \approx 10^5$ J/m^3 · deg, $C_j = 2.5 \cdot 10^6$ J/m^3 · deg, we obtain $\gamma = 0.04$, $\beta = 0.12$, and $T_{max} \approx 10^{4°}K$. For $E_b = 3.3$ eV [6], $E_b/kT_{max} > 3$, so that evaluation the integral (7) by the method of steepest descents is justified. For the indicated values of the parameters and $q = 3.5 \cdot 10^4$ eV/nm, we find from Eq. (12) the value of the sputtering coefficient $S \approx 200$, which agrees satisfactorily with experimental data for sputtering of a gold film on glass [1].

It has been experimentally shown [9] that the energy distribution of electrons emitted from a metallic target bombarded by fission fragments is described better by a model of binary collisions between the fragment and the electrons than by emission from the hot spot [7]. This can be explained by the fact that the δ-electrons that were not taken into account [7] have an insignificant effect on the overall yield of electrons, but make a significant contribution to the high-energy part of the distribution, especially for bombardment of monocrystals.

During sputtering of fine-grained metallic films, the escape of atoms as a result of elastic collisions with the fragment can lead to the appearance of a high-energy tail in the distribution of atoms evaporated from the hot spot.

The conductivity of a film with a thickness not greater than several tens of nanometers is significantly less than the conductivity of the bulk sample [2]. Such a film can be viewed as consisting of isolated grains. In this case, the effect of the electron–phonon collision time is comparable to the electron–electron collision time $\tau_{ee} \approx 10^{-15}$ sec, and it is no longer valid to examine the electron and phonon subsystems in local equilibrium (1). Then, according to the model for the formation of tracks [2], the emission of electrons from a grain due to charging is inhibited and almost all the energy is transferred to the lattice, as a result of which the grain melts and vaporizes, if its radius does not exceed some critical value $R_{cr} = (3q/2\pi n E_b)^{1/2} \approx 10$ nm.

Let us examine the sputtering coefficient when a fragment hits a spherical grain with radius $R < R_{cr}$. Let the fragment pass through the grain at a distance x from the grain center; in this case, the energy transferred to the grain, $E_x = 2q\sqrt{R^2 - x^2}$. The grain will melt if the following condition is satisfied:

$$2q\sqrt{R^2 - x^2} = \frac{4}{3}\pi n R^3 E_b. \tag{13}$$

The probability for the fragment to hit the surface area $dG = 2\pi x\, dx$ equals $dP = dG/\pi R^2$, while the number of evaporated atoms is

$$S = \frac{4}{3}\pi R^3 n \int_0^x dP = \frac{4}{3}\pi n R x^2, \tag{14}$$

where x is a root of Eq. (13). Assuming that all grains have the same radius, equal to some average value $\overline{R}$, we obtain the sputtering coefficient as follows:

$$S = \frac{4}{3}\pi n \overline{R}^3 \left[1 - \left(\frac{\overline{R}}{R_{cr}}\right)^4\right], \tag{15}$$

the maximum value of which, $S_{max} \approx 10^4$, agrees satisfactorily with the experimental value for the case of sputtering of a film on platinum, although the data presented [1] do not permit making any judgments concerning differences in the structure of gold films on glass and platinum.

For a massive metallic foil, due to the long mean free path length with respect to electron–phonon collisions in comparison with the mean free path in a fine-grained film, the maximum temperature of the hot spot decreases approximately by a factor of 10 and the thermal sputtering coefficient becomes negligibly small. In this case, sputtering is determined by elastic collisions between the fragment and lattice atoms, and for fragment energies of the order of tens of MeV, the sputtering coefficient S decreases with increasing fragment energy [10], while the thermal sputtering coefficient of a fine-grain film (12) increases with increasing fragment energy due to the increase in ionization losses.

Angular Distribution of Sputtered Particles. In the process of self-sputtering of a film, the fission fragments forming in the film itself cross its surface at different angles. When a fragment passes parallel to the surface of the film, a grain in the surrounding area will melt or even vaporize. Such a rapid liberation of energy in a small volume leads to the formation of a shock wave. After the shock wave reflects from the free

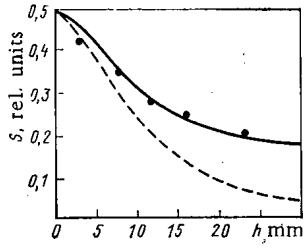

Fig. 1. Number of atoms collected as a function of the distance between the collector and the source: •) experiment [14]; —) calculation according to formula (17); ---) cosinusoidal distribution.

surface, a negative stress forms in the body and, if the tensile forces exceed the strength of the material, then particles break and fly away [11], increasing the sputtering coefficient and leading to the formation of craters. In this case, the angular distribution of the evaporated atoms must differ from a cosine form, since as a result of microexplosions the particles fly out primarily perpendicular to the surface.

There exists some optimum depth H_0 for a fragment to pass along the surface, at which the ejection of particles is at a maximum, since with an increase in the film thickness H only an elastic wave, which does not change the structure of the sample surface, will reach the surface, while at a small depth the number of particles included in the microexplosion will be insignificant. As experimental [12] and theoretical [13] estimates show, this value is given by $H_0 \approx 10$ nm.

Assuming that there are fission fragments that cross the surface in a direction along the normal to the surface and fragments that move parallel to the surface, it is possible to describe the angular distribution relative to the number of atoms emitted into a solid angle Ω by the function

$$f(\Omega) = \frac{1-a}{4\pi} \cdot \cos\theta + \frac{1}{2} a\delta(\Omega). \tag{16}$$

Here, $\delta(x)$ is a delta-function; θ is the angle between the emission direction of the particle and the normal to the surface. The first term in Eq. (16) describes the angular distribution of particles emitted as a result of evaporation from the hot spot; the second term is a result of fragmentation; a is the fraction of such particles, given by $a = \alpha n/(\alpha n + m)$, where n and m are the number of sputtered particles per one "surface" and "orthogonal" fragment, respectively ($n \gg m$); α is the relative number of surface fragments. The dependence of the number of particles collected at a collector with radius r on the distance to the collector h is determined by integrating expression (16) with respect to the solid angle and has the form

$$S_{\text{rel}} = \frac{1}{2}\left[(1-a)\frac{r^2}{r^2+h^2} + a\right]. \tag{17}$$

As can be seen from Fig. 1, the experimental dependence of the number of particles at the collector on h for self-sputtering of a fine-grained film by ^{252}Cf fragments [14] is satisfactorily described by expression (17) with $a = 0.28$. The experiment [14] was performed with a film thickness less than optimum $H < H_0$, and, under such conditions, the relative number of surface fragments $\alpha = \alpha_0 H/H_0$ ($\alpha_0 \approx 10^{-3}$ is the fraction of such fragments with optimum thickness [12]). The experimental data from [14] do not permit judging the precise value of the ratio n/m, but, assuming that $n/m \approx 10^3$, we obtain $a = 0.28$ and film thickness $H = 0.5H_0$, which agrees with the experiment on sputtering of a film with thickness 8 $\mu g/cm^2$ with S = 3800 [14]. For $H > H_0$, the contribution of particles sputtered by fission fragments moving parallel to the surface decreases and, for this reason, the angular distribution of the particles should approximate a cosinusoidal form.

We note that in the case of complete melting and vaporization of a grain, the output of vapor is more likely determined by hydrodynamics, rather than by thermodynamics [15], and the angular distribution of particles will be described by a function similar to (17). Therefore, the experimental study of the angular distribution of particles sputtered by bombardment with fragments from an external source will allow judging the corresponding contributions to sputtering by the mechanisms of vaporization from the hot spot (12) and total vaporization of an isolated grain (15).

Since the value of the sputtering coefficient (12) depends on parameters that are difficult to determine, as well as on the state of the surface [16], it is of interest to measure experimentally the dependence of the sputtering coefficient on the fission fragment energy and to compare this dependence with theoretical calculations.

LITERATURE CITED

1. B. M. Aleksandrov et al., At. Energ., 41, No. 6, 417 (1976).
2. A. Golland and A. Paskin, J. Appl. Phys., 35, No. 7, 2188 (1964).
3. I. M. Lifshits, M. I. Kaganov, and L. V. Tanatarov, At. Energ., 6, No. 4, 391 (1959).
4. Ya. E. Geguzin, M. I. Kaganov, and I. M. Lifshits, Fiz. Tverd. Tela, 15, No. 8, 2425 (1973).
5. M. I. Kaganov, I. M. Lifshits, and L. V. Tanatarov, Zh. Eksp. Teor. Fiz., 31, No. 2, 232 (1956).
6. M. Thompson and R. Nelson, Phil. Mag., 7, No. 84, 2015 (1962).
7. V. M. Agranovich et al., Zh. Eksp. Teor. Fiz., 61, No. 4, 1511 (1971).
8. R. Kelly, Rad. Effects, 32, No. 1-2, 91 (1977).
9. S. Ya. Lebedev, D. D. Odintsov, and Yu. V. Chmyrev, Fiz. Tverd. Tela, 17, No. 2, 621 (1975).
10. M. Kaminskii, Atomic and Ionic Collisions on the Surface of a Metal [in Russian], Mir, Moscow (1967).
11. Ya. B. Zel'dovich and Yu. P. Raizer, Physics of Shock Waves and High Temperature Hydrodynamic Phenomena, Academic Press.
12. V. K. Gorshkov and L. N. L'vov, At. Energ., 20, No. 4, 327 (1966).
13. C. Ronchi, J. Appl. Phys., 44, No. 8, 3575 (1973).
14. B. M. Aleksandrov et al., At. Energ., 33, No. 4, 821 (1972).
15. S. I. Anisimov et al., Action of High-Power Radiation on Metals [in Russian], Nauka, Moscow (1970).
16. V. A. Bessonov, At. Energ., 37, No. 1, 52 (1974).

CROSS SECTION FOR THE FORMATION OF GAMMA-QUANTA DURING THE INTERACTION OF FAST NEUTRONS WITH CARBON, LEAD, AND RHENIUM NUCLEI

M. V. Savin, Yu. A. Khokhlov,
I. N. Paramonova, V. A. Chirkin,
V. N. Ludin, and N. N. Zalyalov

UDC 539.171.02:539.122

Gamma-radiation as a result of inelastic interaction between fast neutrons and intermediate, and especially heavy nuclei consists of a superposition of a line and continuous spectra, caused by transitions between discrete nuclear levels and cascade processes in highly excited states, respectively. For practical applications in nuclear energetics, it is necessary to know the total cross section for the formation of γ-quanta, i.e., the cross section for the formation of the continuous spectrum and the discrete lines. In earlier work, monoenergetic γ-quanta were mainly studied. There is little experimental data concerning the total cross sections for the formation of γ-quanta during inelastic interactions of neutrons with nuclei. This circumstance motivated the present work. Preliminary results for rhenium and lead were presented at the Third All-Union Conference on Neutron Physics [1].

METHOD OF MEASUREMENT

The total cross sections for the formation of γ-quanta were measured on a linear electron accelerator. The technique is described briefly in [1]. The geometry of the experiment, the apparatus, and the setup of the experiment were similarly described in [2].

A tantalum–beryllium target, irradiated by accelerated electrons, served as a neutron source. The ring-shaped neutron beam (D_{out} = 180 mm, D_{in} = 75 mm) was formed with the help of a collimating device placed at the end of an evacuated neutron guide. The samples to be studied, consisting of a natural isotopic composition in the form of a hollow sectioned cone, were placed behind the collimator coaxially with the beam. The thickness of the walls of the cone were 17, 10, and 4 mm for carbon, rhenium, and lead, respectively. Rhenium was used in the form of a metallic powder (ρ = 9.89 g/cm^3), which was poured into a paper container.

The γ-radiation was detected with a hydrogenless liquid scintillation detector (cylinder with D = 54 mm and H = 38 mm). The average angle between the direction of the neutron flux and the detected γ-radiation con-

Translated from Atomnaya Énergiya, Vol. 49, No. 4, pp. 236-239, October, 1980. Original article submitted March 24, 1980.

0038-531X/80/4904-0686$07.50

stituted ~125°. Bursts of light in the scintillator were recorded with an FÉU-93 photomultiplier. The pulse from the anode of the photomultiplier was used simultaneously in the amplitude and time channels. In the time channel, we used a nonlinear time-to-amplitude converter, for which the output amplitude characteristic was nearly exponential. This allowed for a more efficient use of storage with a fairly uniform division of the energy scale. The time scale was calibrated with the help of a variable delay and, in addition, we checked it according to the carbon resonances in the experiment on transmission of the neutron beam through a carbon sample.

The neutron flux on the sample and its energy distribution were measured by the time-of-flight method with a calibrated scintillation detector with a stilbene crystal (D = 30 mm and H = 10 mm). The cross sections for the formation of γ-quanta were measured in separate series, which included measurements with the sample, background measurements, calibration of the time and amplitude scales, and measurements of the energy distribution and flux of neutrons on the samples. An all-wavelength neutron counter served as a monitor. Several series of measurements were performed for each element.

ANALYSIS OF EXPERIMENTAL RESULTS

The amplitude distributions were analyzed by the differentiation method [3]. In order to obtain the sensitivity matrix for the γ detector, we used isotopic sources of monochromatic γ-lines. The process used for performing the measurements on the sources and the method for obtaining the sensitivity functions are described in [2]. The cross section, taking into account the attenuation of the neutron flux and the γ-quanta in the sample, was computed according to the formula

$$\sigma(E_n,\ E_\gamma)=\frac{A\,[\sigma_T(E_n)\,n_0+\mu(E_\gamma)\sin 35^\circ]\ \varphi(E_n,\ E_\gamma)}{1-\exp\{-[\sigma_T(E_n)\,n_0\ +\mu(E_\gamma)\sin 35^\circ]\,l/\sin 35^\circ\}\,n_0\Phi(E_n)} \tag{1}$$

where $\Phi(E_n)$ is the neutron flux on the sample (neutrons); n_0 and l, number of nuclei (cm^{-3}) in and thickness (cm) of the sample; $\sigma_T(E_n)$, total cross section for the interaction of a neutron (cm^2); $\mu(E_\gamma)$, attenuation coefficient for γ-quanta in matter (cm^{-1}); A, a coefficient that takes into account the geometry and normalization according to the monitor channel; $\varphi(E_n, E_\gamma)$, measured energy spectra for the γ-quanta. The transformation of the spectrum due to the scattering of γ-quanta in the sample was computed according to the Monte Carlo method. Formula (1) takes into account the absorption of γ-quanta assuming that all of them are incident on the detector at an angle of 125°. For the indicated thickness, such an approximation has no noticeable error, since the scatter in the values of the γ-quanta path lengths in the sample due to angular resolution is insignificant.

Although we determined that the threshold for detecting γ-quanta in the experiment was equal to E_γ = (0.35-0.4) MeV, we did not take into account the experimental data obtained in the region $E_\gamma < 1$ MeV, since here the results are less reliable due to difficulties in separating out γ-quanta that are annihilated and scattered near objects.

The experimental data for carbon were analyzed using the usual techniques and also with the use of the integral, with respect to the pulse spectra, efficiency for detection of γ-lines $E_\gamma = 4.44$ MeV. In the first case, we determined the function $\varphi(E_\gamma, E_n)$ in formula (1) in the same way as for rhenium and lead by the method of differentiation [3]. In the second case, we computed $\varphi(E_\gamma, E_n)$ according to the formula

$$\varphi(E_\gamma,\ E_n)=\frac{\sum\limits_{i=k_2}^{i=k_{\max}} n_i(E_n)}{\sum\limits_{i=k_1}^{i=k_{\max}} \varepsilon_i(E_\gamma)}, \tag{2}$$

where $n_i(E_n)$ is the number of counts in the i-th channel of the amplitude distribution for a given E_n; $\varepsilon_i(E_\gamma)$ is the differential efficiency of the detector, i.e., the probability for detecting in the i-th channel the amplitude distribution of a γ-quantum emitted from the sample; k_1 and k_2 are the number of channels in the sensitivity matrix and in the experimental amplitude distribution corresponding to the chosen energy threshold $E_{\gamma t}$.

In our analysis, we chose a fairly high threshold: for carbon $E_{\gamma t} = 2$ MeV and for the background with a beryllium sample $E_{\gamma t} = 2.7$ MeV. The results obtained with the two methods for processing data agreed well with each other.

Corrections. The background resulting from neutrons scattered elastically from the sample, detected as a result of γ-quanta from the reaction (n, n'γ) in a carbon scintillator, was determined for rhenium and lead

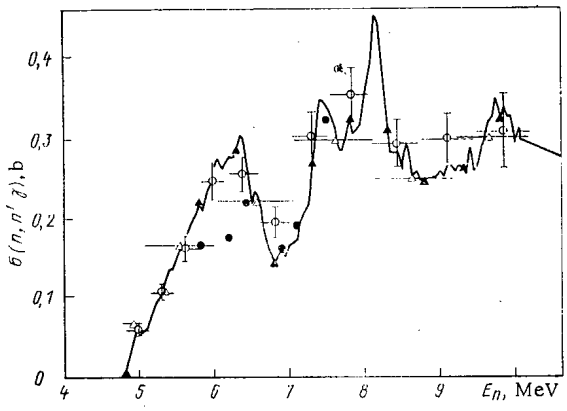

Fig. 1. Cross section for the formation of γ-lines $E_\gamma = 4.44$ MeV in the reaction (n, n'γ) with carbon: ○ – present work; ●, △, ▲ – data from [4, 5, 6], respectively.

by measurements with a carbon sample and for carbon by measurements with a beryllium sample. The background of the beam and the place for each energy interval $E \leq E_\gamma \leq E_i + \Delta E$ was found from the results obtained in the neutron energy range below threshold for the formation of the given group of γ-quanta. This background constituted: for rhenium in the range $E_\gamma = (1\text{-}1.25)$ MeV 10%, in the range $E_\gamma = (3\text{-}5)$ MeV 4-3%; for lead in the range E_γ (1-1.25) MeV 2%, and for $E_\gamma = 2$ MeV, the background was close to zero. For carbon, there was almost no background. The Monte Carlo method was used to compute the corrections for multiple scattering of neutrons. The maximum value of the corrections was ≈ 5, 17, and 15% for carbon, rhenium, and lead, respectively.

For carbon, we introduced a correction for the angular distribution of γ-quanta, which we obtained from the experimental data [4]. The corrections did not exceed 5%.

Errors. In calculating the total error $\sigma(n, x\gamma)$, we took into account the statistical error in the measurements and systematic errors related to determining the absolute value of the neutron flux (4–5%), calibration of the γ-detector (2.5%), the uncertainty in the method used for analysis (15%), and the difference in the position of the origin on the time scales in the cross section measurements and the spectra of neutrons incident on the sample ($\Delta\tau = \pm 0.135$ nsec/m). The systematic error in determining the cross section, arising from the uncertainty in the shift of the time scales, was significant for high-energy neutrons (short time-of-flight): for the spectra of neutrons emitted from a tantalum–beryllium target, this error for $E_n = 9$ MeV constituted $\sigma \approx 4\%$, while for $E_n < 5$ MeV $< 1\%$. The total statistical error was determined taking into account the statistical errors in the measurements of the neutron flux, calibration of the γ-detectors, and random errors which we found from the scatter in the separate series of measurements.

RESULTS OF MEASUREMENTS

Carbon. Figure 1 shows the cross sections obtained and the total error in the measurements, as well as the results recently obtained by other researchers [4-6]. Drake et al. [4] performed the measurements on a pulsed electrostatic generator and detected the γ-quanta with an NaI(Tl) crystal. In [5, 6], the cross sections were measured on a linear electronic accelerator using Ge(Li) spectrometers. In [5] there is no detailed numerical information so that Fig. 1 shows only cross sections that were averaged by the authors of [5] over a wide range of neutron energies. We obtained the data of Morgan et al. from the figure presented in [6].

As can be seen from Fig. 1, our results agree well with the data obtained by other researchers, with the exception of two values from [4] for $E_n = 5.8$ and 6.21 MeV, which are significantly less than most of the data.

Rhenium. The cross section for the formation of γ-quanta with inelastic interaction of neutrons with rhenium nuclei and the total error in the measurements are shown in Fig. 2. The experimental data concerning the cross sections for the formation of γ-quanta on rhenium nuclei have not yet been published.

Using the statistical description of inelastic neutron scattering, the energy balance in the reaction (n, n'γ) can be written in the form $\bar{E}_\gamma \sigma = \sigma_{in}(E_n - 2T)$, where $\bar{E}_\gamma$ is the average energy in the γ-spectrum; σ is the total (for the entire spectrum) cross section for the formation of γ-quanta; σ_{in} is the cross section for inelastic neutron scattering, taken as $\sigma_{in} = 2.5$ b (1 b $= 10^{-28}$ m^2); T is the temperature of the residual nucleus. T was cal-

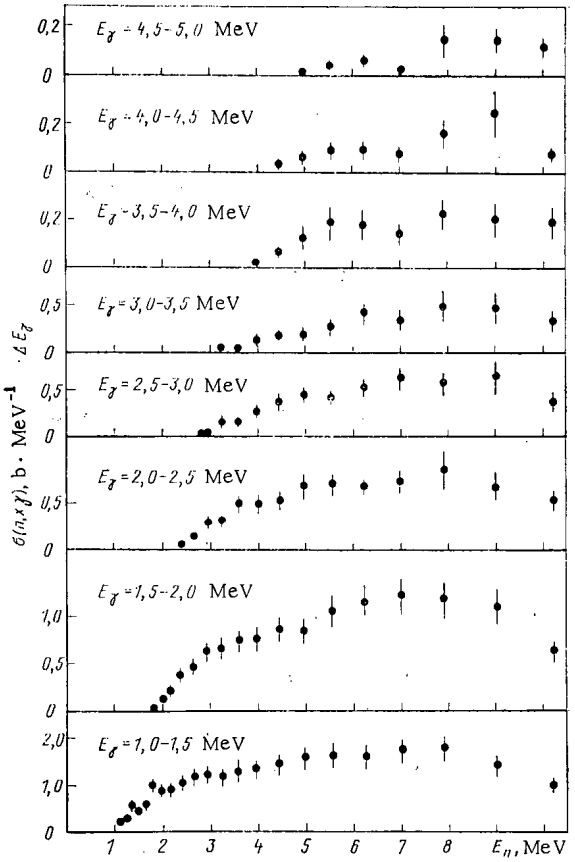

Fig. 2

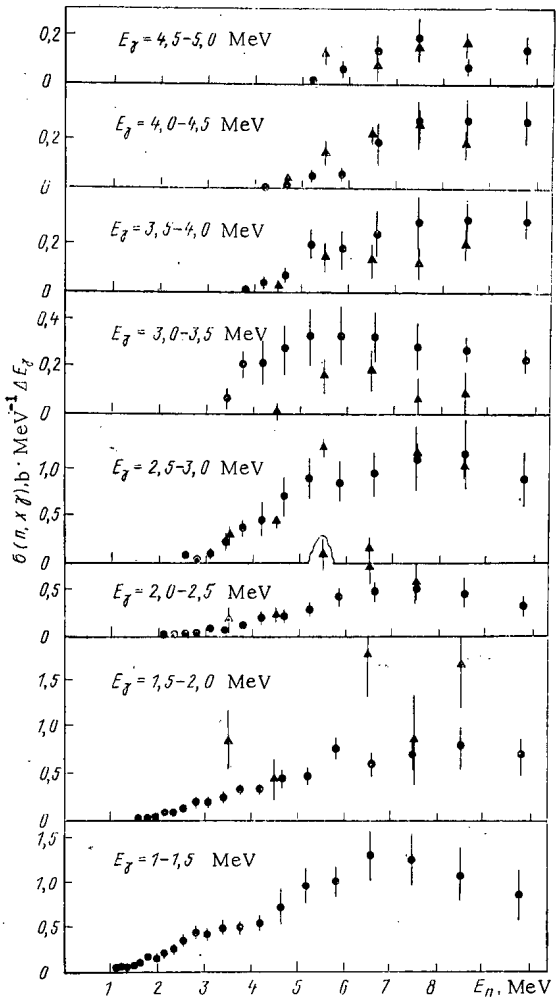

Fig. 3

Fig. 2. Total cross section for the formation of γ-quanta in the reaction (n, xγ) with rhenium nuclei.

Fig. 3. Total cross section for the formation of γ-quanta in the reaction (n, xγ) with lead nuclei: ● – present work; ▲ – data from [7].

culated from the formula for energy balance, assuming that the cross section for the formation of γ-quanta with energy $E_\gamma < 1$ MeV is constant and equals the cross section in the range $E_\gamma = (1\text{–}1.25)$ MeV. It turned out that when the neutron energy increases in the range $E_n = 3\text{–}9$ MeV, the temperature changes from 0.7 to 0.3 MeV. This result does not contradict the existing ideas of the statistical theory of the decay of a compound nucleus.

Lead. The data obtained for lead are shown in Fig. 3, wherein the results of the only published experimental work of Perkin [7], carried out with an electrostatic Van de Graaf generator, are also shown. The data are not contradictory; however Perkin's results for γ-quanta with energy 1.5–2 MeV significantly exceed our data for $E_n = 3.5\text{–}6.5$ MeV, while for γ-quanta with energy 3–4 MeV, they are systematically less than our data.

Natural lead consists of three isotopes: ^{206}Pb(24%), ^{207}Pb(23%), and ^{208}Pb(53%). For all isotopes up to an excitation energy ~4 MeV, γ-quanta are formed due to transitions between discrete levels of the residual nucleus.

Gamma-radiation with energy 1–1.5 MeV in the range of neutron energies (approximately up to 3 MeV) arises mainly as a result of the transitions $1.462(2^+) \rightarrow 0(0^+)$ and $1.998(2^+) \rightarrow 0.803(2^+)$ in the ^{206}Pb nucleus. Gamma-quanta with energies 1.5–2 MeV are formed ($E_n < 4$ MeV) primarily as a result of the three transitions: $1.70(1^+) \rightarrow 0^+$; $2.634(3^-) \rightarrow 0.803(2^+)$ in the ^{206}Pb nucleus; and, 2.34 ($^7/_2$-) → 0.570($^5/_2$-) in the ^{207}Pb nucleus. The total cross section for the formation of γ-lines for these transitions ($E_\gamma = 1.7$, 1.83, and 1.77 MeV) constitutes 0.150–0.250 b in the range of neutron energies $E_n = 3\text{–}4$ MeV [8], which coincides with the results obtained in the present experiments.

Gamma-quanta with energies $E_\gamma = 2.5$-3 MeV arise mainly as a result of the transition 2.615 $(3^-) \rightarrow 0(0^+)$ in ^{208}Pb. Indeed, the cross section for the formation of γ-quanta with $E_\gamma = 2.5$-3 MeV in our measurements coincides with the cross section for the formation of the 2.615-MeV γ-line measured in [9], where for $E_n = 4$ MeV the value ~0.400 b was obtained. For higher neutron energies ($E_n > 5$ MeV), the continuous γ-radiation spectrum begins to appear in the γ-spectrum of lead.

CONCLUSIONS

The values obtained for the cross sections for formation of γ-lines ($E_\gamma = 4.44$ MeV) in carbon agree with the data obtained by other researchers, within experimental error.

The results of measurements for lead agree qualitatively with our understanding of the deexcitation of levels in the reaction (n, nγ) for $E_n < 4$ MeV.

The energy distribution of γ-quanta for rhenium decreases smoothly with increasing E_γ. No irregularities, related to separate intense γ-transitions in the excited nucleus, are noticeable.

LITERATURE CITED

1. M. V. Savin et al., in: Neutron Physics (Materials Presented at the Third All-Union Conference on Neutron Physics, Kiev, 9-13 June 1975), Pt. 4 [in Russian], Moscow (1976), p. 191.
2. M. V. Savin et al., Yad. Fiz., 23, 512 (1976).
3. V. G. Dvukhsherstnov et al., Prib. Tekh. Eksp., No. 4, 39 (1969).
4. D. Drake et al., Nucl. Sci. Eng., 40, 294 (1970).
5. V. Rogers et al., ibid., 58, 298 (1975).
6. G. Morgan, T. Love, and F. Percy, Nucl. Instrum. Methods, 128, 125 (1975).
7. J. Perkins, Nucl. Phys., 60, 561 (1964).
8. Yu. G. Degtyarev, V. V. Chulkov, and V. N. Protopopov, in: Neutron Physics (Materials Presented at the Second All-Union Conference on Neutron Physics, Kiev, 28 May-1 June 1973), Pt. 3 [in Russian], Obninsk (1974), p. 120.
9. D. Nellis, I. Morgan, and E. Hudspeth, Phys. Rev., C9, 1972 (1974).

GROUP AND TOTAL CROSS SECTIONS OF FORMATION OF γ-RAY QUANTA UPON THE INTERACTION OF 14-MeV NEUTRONS WITH VARIOUS NUCLEI

V. M. Bezotosnyi, V. M. Gorbachev, M. S. Shvetsov, and L. M. Surov

UDC 539.172.4

A comparatively large number of papers have been published up to this time which deal with the spectra and cross sections of formation of γ-quanta originating upon the interaction of 14-MeV neutrons with various nuclei [1-9, 11-13].

The results of cross section measurements are given in [1-5] only for individual discrete γ-lines. However, in a number of cases associated with the use of fast neutrons the total cross sections of formation of γ-quanta, which consist of the cross sections of formation of discrete γ-lines and the cross sections of formation of γ-quanta produced by the unresolved part of the spectrum, are of practical importance. The results of the measurements of these cross sections are given in [6-9, 11-13]. The calculated values of the group cross sections of formation of γ-quanta for ^{238}U are given in [14].

Measurements of the cross sections of formation of individual γ-lines and the group cross sections $\sigma_\gamma = f(E_\gamma)$ for nuclei from ^{10}B to ^{209}Bi have been performed by the authors on a pulsed 14-MeV generator [6, 7, 9]. The results of our measurements of $\sigma_\gamma = f(E_\gamma)$ for Cu and the fissionable nuclei ^{235}U, ^{238}U, and ^{239}Pu are also

Translated from Atomnaya Énergiya, Vol. 49, No. 4, pp. 239-242, October, 1980. Original article submitted November 5, 1979.

0038-531X/80/4904-0690$07.50

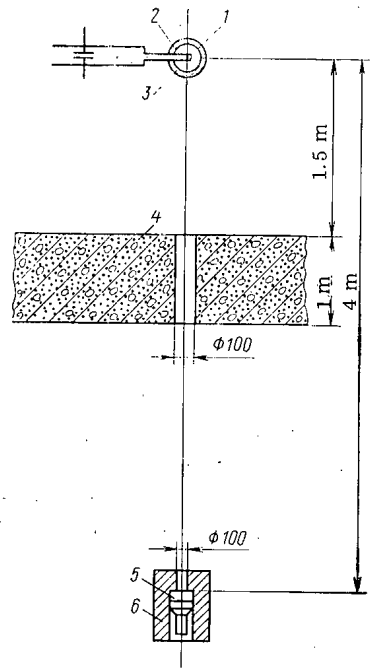

Fig. 1. Layout of the experiment: 1) target of ZrT; 2) the "proboscis" of the accelerator tube; 3) sample; 4) concrete; 5) NaI(Tl) crystal 200× 100 mm in diameter; and 6) lead.

given in this paper. These data together with those published earlier are used for the determination of the total cross sections of formation of γ-quanta upon the inelastic interaction of 14-MeV neutrons with various nuclei.

Experimental Procedure. The measurements were made with a pulsed source of 14-MeV neutrons on spherical samples (4π-geometry) with the use of the time-of-flight procedure, a scintillation γ-ray total absorption spectrometer with an NaI(Tl) crystal 200× 100 mm in diameter, and an AI-256 pulse analyzer. The layout of the experiment is given in Fig. 1. The γ-ray detector was placed behind a concrete shield at a transit distance of 4 m from the neutron source. The surface of the NaI(Tl) crystal, which is turned in the direction of the sample being investigated, was restricted by a lead collimator with an inner diameter of 100 mm.

The samples being investigated were made up mainly of natural isotopic composition in the form of hollow spheres. The zirconium–tritium target of the neutron source was located at the center of the sample. Such a geometry permits neglecting the dependence of the yield of γ-quanta on the angle of emergence relative to the direction of motion of the neutrons and optimally investigating the neutron flux.

In order to obtain the instrumental spectrum of the γ-radiation, two measurements were made: with the sample being investigated and without the sample (background distribution). The background from γ-quanta originating in the target device of the neutron generator was also taken into account. The efficiency of recording of the γ-ray detector was determined experimentally with the help of the computational data given in [10]. The experiment is described in more detail in our papers [6, 7, 9].

Results and Discussion of Them. The group cross sections of formation of γ-quanta obtained by multiplication of the differential cross sections in mb/sr by 4π are given in Table 1. The total cross sections σ_γ obtained by the summation of the group cross sections from E_γ^{min} to E_γ^{max} are given in Table 2. As is evident, our results for the cross sections of γ-formation agree within the limits of error of the measurements for the majority of nuclei with the published data. Weighted average values of the cross sections σ_γ (estimated data), which are also given in Table 2, are obtained from the results of our measurements and those of [1-5, 8, 11, and 12].

The values of the total cross sections σ_γ obtained by us are given in Fig. 2 as a function of $A^{1/3}$. For nuclei from oxygen to ^{238}U (with the exception of Pb) a linear dependence $\sigma_\gamma = f(A^{1/3})$ is observed within the limits of error of the measurements. For light nuclei from boron to oxygen a linear dependence $\sigma_\gamma = f(A^{1/3})$ is

TABLE 1. Group Cross Sections of Formation of γ-Quanta upon Inelastic Interaction of 14-MeV Neutrons with Medium and Heavy Nuclei (A = 24-239), MB

Interval of E_γ, MeV	Mg [9]	Al [6]	Si [9]	P [9]	S [9]	Ti [9]	Fe [6]	Cu This paper	Zn [9]	Zr [9]	Mo [9]
0,5–1,0	58±10	236±47	210±30	560±108	145±30	700±105	1430±210	2750±550	1617±307	1415±270	3100±585
1,0–1,5	506±120	292±48	155±30	487±100	240±43	1250±175	890±134	1350±270	1792±288	788±180	1450±215
1,5–2,0	170±30	285±40	480±98	229±51	340±60	360±60	340±60	475±100	642±105	657±140	780±120
2,0–2,5	140±22	281±37	90±15	469±97	640±100	300±63	273±51	280±60	300±50	1010±206	380±60
2,5–3,0	136±24	232±31	120±20	120±24	200±36	225±38	264±47	160±35	238±42	374±85	320±60
3,0–3,5	90±16	64±13	130±20	100±20	110±20	160±27	175±35	135±30	200±40	290±65	170±29
3,5–4,0	75±21	58±12	98±15	90±20	106±20	160±22	131±28	102±25	133±28	260±54	132±20
4,0–4,5	65±14	65±13	58±15	77±18	100±20	100±20	100±20	88±22	115±19	186±36	105±17
4,5–5,0	60±17	59±12	87±20	74±17	80±14	130±36	86±17	75±23	93±13	140±35	80±11
5,0–5,5	55±10	51±10	76±18	46±10	55±10	122±18	76±15	65±20	86±13	116±25	45±10
5,5–6,0	50±9	46±9	60±11	43±9	60±11	87±22	75±15	54±17	73±11	104±26	54±10
6,0–6,5	45±11	43±9	45±8	76±20	40±8	70±15	74±14	47±15	58±10	90±20	45±10
6,5–7,0	45±8	44±9	70±14	35±8	44±8	95±16	62±13	49±15	55±10	86±23	45±10
7,0–7,5	40±7	40±9	77±14	48±13	35±9	60±13	70±14	41±13	50±10	75±32	36±10
7,5–8,0	45±8	32±7	59±10	19±5	25±6	65±13	60±12	40±13	37±7	63±32	12±6
8,0–8,5	40±7	30±8	40±6	10±5	17±5	40±10	53±11	30±15	28±6	58±30	12±6
8,5–9,0	26±6	20±5	30±8	8±6	7±4	30±8	44±9	28±14	22±8	45±26	12±6
9,0–9,5	25±6	17±5	40±6	9±9	3±2	25±8	31±6	25±12	11±7	32±20	9±5
9,5–10,0	21±9	11±5	34±7	6±6	2±2	11±5	19±5	22±11	6±4	21±15	6±4
10,0–10,5	18±9	8±6	26±6	4±4	1±2	10±6	15±5	15±8	6±5	10±7	3±2
10,5–11,0	15±9		10±4	2±2		5±5	5±5		4±3	5±7	2±2
11,0–11,5	5±5		7±3	2±2		3±3			2±2	4±5	1±1
11,5–12,0	2±2		4±2	1±1		2±2			2±2	1±1	1±1

Interval of Eγ, MeV	Cd [9]	In [9]	Sn [9]	Ta [6]	W [6]	Hg [9]	Pb [6]	Bi [9]	^{235}U This paper	^{238}U This paper	^{239}Pu This paper
0,5–1,0	3100±510	2468±395	1930±386	3000±600	4250±850	4200±700	2960±405	2500±620	7600±1230	5200±780	8950±1510
1,0–1,5	1150±210	1665±265	2330±375	2600±460	2340±460	1800±310	1215±200	4585±940	4060±650	2480±375	3960±660
1,5–2,0	766±134	793±121	710±114	1170±230	1280±260	1140±180	653±115	1350±260	2130±340	1660±255	1770±310
2,0–2,5	530±95	640±107	421±84	920±180	950±190	710±112	485±80	900±190	1129±190	1200±185	920±150
2,5–3,0	405±80	322±50	370±74	746±150	650±130	520±100	322±76	587±117	590±110	560±90	470±77
3,0–3,5	313±60	256±40	211±47	290±60	270±60	300±51	190±40	364±106	370±80	320±55	330±56
3,5–4,0	180±34	153±36	114±25	185±37	230±60	180±31	110±20	223±56	210±55	161±35	225±35
4,0–4,5	132±26	90±20	73±14	150±30	167±35	150±26	98±20	153±48	178±40	154±30	170±27
4,5–5,0	120±27	75±19	68±14	100±85	80±20	90±20	80±16	148±47	96±25	70±17	101±20
5,0–5,5	83±20	63±18	40±7	44±15	65±18	84±20	56±12	88±20	79±25	94±20	70±17
5,5–6,0	73±17	52±12	41±7	40±12	45±15	60±15	45±10	106±40	40±20	68±16	48±20
6,0–6,5	62±16	35±10	35±7	36±10	39±15	26±8	31±10	105±47	28±18	90±18	30±15
6,5–7,0	81±26	46±11	34±9	32±11	4±4	48±10	24±7	109±50	54±20	89±20	9±5
7,0–7,5	70±24	40±18	27±14	21±10		28±10	25±7	136±65	29±14	38±16	6±6
7,5–8,0	41±19	33±15	19±11	13±7		21±10	22±7	131±65	3±3	19±12	1±1
8,0–8,5	24±15	19±10	19±11			14±8	22±7	62±30			
8,5–9,0	15±9	22±10	10±6			9±7	19±7	52±26			
9,0–9,5	20±15	13±9	7±5			7±6	18±6	39±20			
9,5–10,0	10±8	10±9	6±5			8±6	14±7	29±18			
10,0–10,5	8±6	9±8	5±5			5±5	15±7	13±15			
10,5–11,0	6±5	7±9	5±5				15±7				
11,0–11,5	4±4	2±4	3±3				10±7				
11,5–12,0	2±2	2±4	2±2				8±7				

TABLE 2. Total Cross Sections of Formation of γ-Quanta upon Inelastic Interaction of 14-MeV Neutrons, MB

Target nucleus	Energy or energy interval E_γ, MeV	Data of this paper	Data of other papers	Av. data
^{10}B	0,48–6,1	161±31 [6]	146±9 [4]	147±8,6
^{11}B	1,1–9,3	410±62 [6]		
C	4,45	255±26 [7]	245±35 [1] 232±18 [2] 202±26 [8]	230±12
N	0,73–7,0	333±60 [6]	298±56 [5]	314±41
	1,63–7,0	317±58 [6]	298±82 [3]	
O	0,74–7,1	500±65 [6]		
	0,98–7,1	488±62 [6]	451±80 [3]	474±49
	0,5–7,1		520±130 [12]	
Mg	0,5–12,0	1732±380 [9]		
	0,5–8,5	1630±334 [9]	1400±169 [8]	1445±151
	0,2–8,5		1600±228 [8]	
Al	0,5–10,5	1914±335 [6]	1700±425 [12]	1832±263
	0,5–8,5	1858±314 [6]	1430±166 [8]	1524±147
	0,2–8,5		1537±195 [8]	
	2,0–11,0	1100±200 [6]	800±400 [13]	
Si	0,5–12,0	2000±380 [9]		
	0,5–8,5	1855±344 [9]	1553±183 [8]	1620±162
	0,4–8,5		1580±192 [8]	
P	0,5–12,0	2515±555 [9]	–	
	0,5–8,5	2483±525 [9]	–	
S	0,5–10,5	2250±410 [9]	–	
	0,5–8,5	2237±400 [9]	–	
Ti	0,5–12,0	4010±690 [9]	–	
	0,5–8,5	3924±653 [9]	3037±334 [8]	3220±297
	0,2–8,5		3333±415 [8]	
Fe	0,5–11,0	4273±726 [6]	4630±500 [11]	4495±412
	0,5–8,5	4159±700 [6]	3156±354 [8]	
	0,2–8,5		3539±460 [8]	
	2,0–11,0	1600±320 [6]	1350±575 [13]	
Cu	0,5–10,5	5831±1268		
	0,5–10,0	5785±1260	6300±1575 [12]	5985±984
	0,5–8,5	5740±1223	2822±309 [8]	
	0,2–8,5		3419±500 [8]	
Zn	0,5–12,0	5570±990 [9]	–	
	0,5–8,5	5517±959 [9]	–	
Zr	0,5–12,0	5830±1340 [9]	–	
	0,5–8,5	5712±1259 [9]	–	
Mo	0,5–12,0	6800±1200 [9]		
	0,5–8,5	6766±1179 [9]	4903±545 [8]	5232±495
	0,2–8,5		5870±833 [8]	
Cd	0,5–12,0	7195±1362 [9]	–	
	0,5–8,5	7130±1313 [9]	–	
In	0,5–12,0	6815±1200 [9]	–	
	0,5–8,5	6750±1147 [9]	–	
Sn	0,5–12,0	6480±1220 [9]	–	
	0,5–8,5	6442±1189 [9]	–	
Ta	0,5–8,0	9000±1830 [6]	4975±998 [8]	5896±876
	0,3–9,0		6704±1217 [8]	
W	0,5–7,0	10400±2100 [6]	–	
Hg	0,5–10,5	9400±1640 [9]	–	
	0,5–8,5	9371±1616 [9]	–	
Pb	0,5–12,0	6500±1080 [6]		
	0,5–8,5	6338±1032 [6]		
	0,5–5,0	6100±970 [6]	4200±1050 [12]	5225±712
Bi	0,5–12,0	11680±2780 [9]	–	
	0,5–8,5	11547±2700 [9]	–	
^{235}U	0,5–8,0	16596±2820	15382±1848 [8]	15730±1545
	0,3–8,0		20632±2376 [8]	
^{238}U	0,5–8,0	12203±1924	9140±1036 [8]	9829±912
	0,4–8,5		10546±1358 [8]	
	0,5–8,0		9885±1660 [14]	
^{239}Pu	0,5–8,0	17060±2910	16332±2356 [8]	16623±1830
	0,3–8,0		23150±3056 [8]	

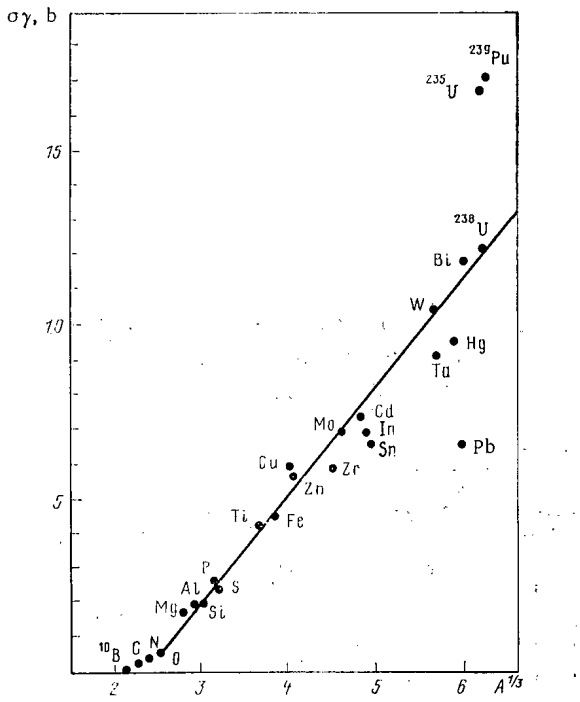

Fig. 2. Dependence of the cross section of formation of γ-quanta on the mass number $\sigma_\gamma = f(A^{1/3})$.

also observed, but with a different slope. The cross section of γ-formation for ^{235}U and ^{239}Pu is not subject to such a simple dependence and is ≈ 1.5 times larger than that for ^{238}U. This circumstance can evidently be explained by the fact that the main process of γ-formation for ^{235}U and ^{239}Pu is fission, and the fission cross section of these nuclei is ≈ 2 times greater than that for ^{238}U.

LITERATURE CITED

1. M. Batatt and E. Graves, Phys. Rev., 97, 1266 (1955).
2. D. Stewart and P. Martin, Nucl. Phys., 60, 349 (1964).
3. F. Engesser and W. Thompson, J. Nucl. Energy, 21, 487 (1967).
4. D. Nellis, W. Tucker, and Ira L. Morgan, Phys. Rev. C, 1, 847 (1970).
5. K. Nyberg-Ponnert, B. Jönson, and I. Bergqvist, Physica Scripta, 4, 165 (1971).
6. V. M. Bezotosnyi et al., in: Nuclear Constants [in Russian], No. 19, Atomizdat, Moscow (1975), p. 77.
7. V. M. Bezotosnyi et al., in: Transactions of the Neutron Physics Conference [in Russian], Part 4, TsNIIatominform, Moscow (1976), p. 133.
8. D. Drake, E. Arthur, and M. Silbert, Nucl. Sci. Eng., 65, 49 (1978).
9. V. M. Bezotosnyi et al., in: Nuclear Constants [in Russian], No. 3 (30), TsNIIatominform, Moscow (1978), p. 21.
10. N. A. Vartanov and P. S. Samoilov, Practical Methods of Scintillation γ-Ray Spectrometry [in Russian], Atomizdat, Moscow (1964).
11. V. Scherrer, R. Theus, and W. Faust, Phys. Rev., 89, 1268 (1953).
12. V. Scherrer, R. Theus, and W. Faust, Phys. Rev., 91, 1476 (1953).
13. R. Caldwell, W. Mills, and J. Hickman, Nucl. Sci. Eng., 8, 173 (1960).
14. H. Takahashi, Nucl. Sci. Eng., 51, 296 (1973).

^{232}Th, ^{238}U, AND ^{40}K CONCENTRATIONS IN VARIOUS TYPES OF PHOTOMULTIPLIERS

E. L. Koval'chuk, A. A. Smol'nikov, and A. Kh. Temmoev

UDC 539.107.43

In γ spectrometry performed with scintillators on extremely small amounts of radionuclides, one must exactly know the intrinsic background of the detector equipment and, first of all, of the photomultipliers when the NaI(Tl) single crystal has a low concentration of radioactive impurities. It follows from an analysis of the α emission spectrum [1] that the ^{232}Th and ^{238}U concentrations in the NaI(Tl) single crystal with which the measurements were made amount to $\sim 10^{-11}$ g per g of the crystal. Thus, a large fraction of the background of the detection equipment used (disregarding the external background) originates from the crystal packing and the photomultiplier proper. In most of the papers concerned with research on the contribution of the photomultiplier to the background of the detector, either particular photomultiplier types are considered or only relative values of the contamination by radioactive impurities are given [2].

In order to obtain a precise idea of the contribution of the photomultiplier to the overall background of a detector and for selecting photomultipliers of lowest activity, measurements were made on 14 types of multipliers of national (Russian) manufacture and the ^{232}Th, ^{238}U, and ^{40}K concentrations for each of the types were calculated. Furthermore, the dynode system with the base and the glass of the bulb were included in the measurements made on several photomultipliers and the relative contribution of those components to the background resulting from the photomultiplier proper was determined.

The ^{232}Th, ^{238}U, and ^{40}K concentrations of the glass of the bulbs of several photomultipliers and of samples of quartz sand (the possible raw material for producing the quartz bulbs of photomultipliers) were compared.

The concentration of the radionuclides in the samples was calculated by determining the area under the peaks of total absorption of γ-quanta in the spectrum resulting from the equipment proper and by comparing the areas with spectra of standard sources. The selection of the intervals of summation in the spectrum

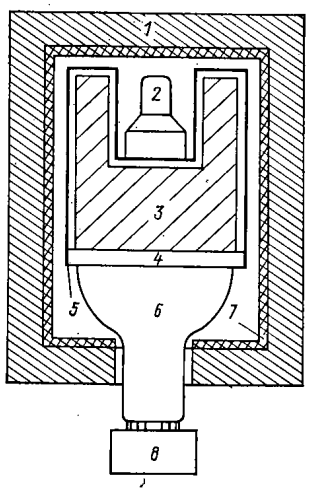

Fig. 1. Setup for measuring the concentration of radionuclides in samples: 1) passive tungsten shield; 2) photomultiplier sample on which measurements are made; 3) NaI(Tl) single crystal; 4) quartz light guide; 5) (stainless steel) housing; 6) photomultiplier; 7) Plexiglas; 8) preamplifier.

Translated from Atomnaya Énergiya, Vol. 49, No. 4, pp. 242-245, October, 1980. Original article submitted January 7, 1980; revision submitted May 5, 1980.

0038-531X/80/4904-0695$07.50

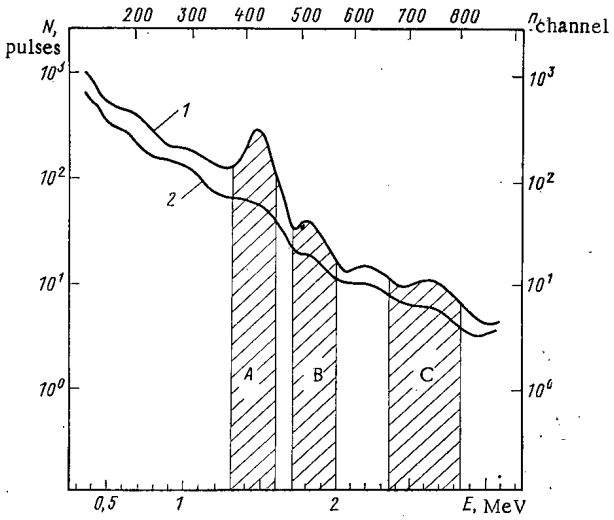

Fig. 2. Intrinsic spectra of 1) one of the FÉU-81 photomultipliers and 2) the background. A, B, and C denote the intervals in which the area under the peaks of total absorption was calculated for ^{40}K (1.46 MeV), ^{238}U (1.76 MeV), and ^{232}Th (2.62 MeV), respectively.

resulting from the equipment proper is one of the reasons for errors made with this method. Only a few techniques of selecting the optimum interval are described in the literature, but these techniques may lead to different quantitative results in the determination of the concentration of radionuclides in particular samples [3, 4], for example, when the difference between the uranium and potassium concentrations in the standard and the sample under inspection is very large.

We used in our work the technique of inserting, in succession, the values obtained from various intervals into a formula for calculating the concentration so that the difference between the measured and the known concentration of a particular nuclide in standard granite samples was minimized. Among all the intervals, the optimum interval selected was characterized by the fact that by making calculations with that interval, the difference between the measured and the known concentration reached its minimum for all standard samples.

When standard sources of the various nuclides are employed and the concentrations are calculated in the sequence Th, U, K, one can employ the following formulas for determining the radionuclide concentration in the samples on which the measurements are made:

$$Q^{\mathrm{Th}}\left(\frac{g\ \mathrm{Th}}{g}\right)_{\mathrm{sam}}=\frac{m_e^{\mathrm{Th}}\left(\frac{S^{\mathrm{sam}}_{2,62}}{t_{\mathrm{sam}}}-\frac{S^{b}_{2,62}}{t_b}\right)}{M_{\mathrm{sam}}\left(\frac{S^{e\ \mathrm{Th}}_{2,62}}{t_{e\ \mathrm{Th}}}-\frac{S^{b}_{2,62}}{t_b}\right)}; \tag{1}$$

$$Q^{\mathrm{U}}\left(\frac{g\ \mathrm{U}}{g}\right)_{\mathrm{sam}}=\frac{m_e^{\mathrm{U}}\left(\frac{S^{\mathrm{sam}}_{1.76}}{t_{\mathrm{sam}}}-\frac{S^{e\ \mathrm{Th}}_{1,76}m^{\mathrm{Th}}_{\mathrm{sam}}}{t_{e\ \mathrm{Th}}m_e^{\mathrm{Th}}}-\frac{S^{b}_{1,76}}{t_b}\right)}{M_{\mathrm{sam}}\left(\frac{S^{eU}_{1,76}}{t_{eU}}-\frac{S^{b}_{1,76}}{t_b}\right)}; \tag{2}$$

$$Q^{\mathrm{K}}\left(\frac{g\mathrm{K}}{g}\right)_{\mathrm{sam}}=\frac{m_e^{\mathrm{K}}\left(\frac{S^{\mathrm{sam}}_{1,46}}{t_{\mathrm{sam}}}-\frac{S^{e\ \mathrm{Th}}_{1,46}m^{\mathrm{Th}}_{\mathrm{sam}}}{t_{e\ \mathrm{Th}}m_e^{\mathrm{Th}}}-\frac{S^{eU}_{1,46}m^{\mathrm{U}}_{\mathrm{sam}}}{t_{eU}m_e^{\mathrm{U}}}-\frac{S^{b}_{1,46}}{t_b}\right)}{M_{\mathrm{sam}}\left(\frac{S^{eK}_{1,46}}{t_{eK}}-\frac{S^{b}_{1,46}}{t_b}\right)}, \tag{3}$$

where Q denotes the concentration of a particular nuclide X per gram of sample material under inspection (Q

TABLE 1. ^{232}Th, ^{238}U, and K Concentrations in Various Types of Photomultipliers, Samples of Quartz Sand, and Granite Standard Samples

Sample	Made in	^{232}Th	^{238}U	K *	$K_M = \frac{\text{Sample mass}}{\text{PM mass}}$
FÉU-13 (glass of the bulb)	1970	$(2,0\pm0,1)\cdot10^{-6}$†	$(4,1\pm0,2)\cdot10^{-6}$	$(3,91\pm0,08)\cdot10^{-2}$	0,56
FÉU-13 (dynode system and base)	1970	$(6,6\pm0,7)\cdot10^{-6}$	$(1,1\pm0,1)\cdot10^{-5}$	$(7,7\pm1,6)\cdot10^{-3}$	0,44
FÉU-13B	1974	$(2,0\pm0,3)\cdot10^{-6}$	$(6,8\pm2,6)\cdot10^{-7}$	$(4,14\pm0,08)\cdot10^{-2}$	—
FÉU-24 (glass of the bulb)	1958	$(6,3\pm2,1)\cdot10^{-7}$	$(9,1\pm2,1)\cdot10^{-7}$	$(7,19\pm0,08)\cdot10^{-2}$	0,68
FÉU-24 (dynode system and base)	1958	$(1,5\pm0,5)\cdot10^{-6}$	$(2,4\pm0,5)\cdot10^{-6}$	$(2,8\pm0,2)\cdot10^{-2}$	0,32
FÉU-29	1965	$(6,3\pm1,7)\cdot10^{-7}$	$(2,9\pm0,2)\cdot10^{-6}$	$(3,82\pm0,08)\cdot10^{-2}$	—
FÉU-30	1969	$(8,0\pm1,0)\cdot10^{-7}$	$(1,8\pm0,1)\cdot10^{-6}$	$(3,20\pm0,07)\cdot10^{-2}$	—
FÉU-43 (glass of the bulb)	1970	$(4,4\pm0,2)\cdot10^{-6}$	$(3,5\pm0,3)\cdot10^{-6}$	$(3,2\pm1,8)\cdot10^{-4}$	0,72
FÉU-43 (dynode system and base)	1970	$(1,0\pm0,3)\cdot10^{-6}$	$(9,5\pm3,6)\cdot10^{-7}$	$(1,25\pm0,08)\cdot10^{-2}$	0,28
FÉU-49 (glass of the bulb)	1975	$(9,9\pm0,5)\cdot10^{-7}$	$(1,1\pm0,2)\cdot10^{-6}$	$(2,5\pm0,5)\cdot10^{-4}$	0,87
FÉU-49 (dynode system and base)	1975	$(9,4\pm0,2)\cdot10^{-7}$	$(5,5\pm3,1)\cdot10^{-7}$	$(7,0\pm0,7)\cdot10^{-4}$	0,13
FÉU-49B (glass of the bulb)	1976	$(9,4\pm0,2)\cdot10^{-7}$	$(7,5\pm2,2)\cdot10^{-7}$	$(7,1\pm3,6)\cdot10^{-5}$	0,87
FÉU-49B (dynode system and base)	1976	$(1,2\pm0,2)\cdot10^{-6}$	$(6,9\pm1,6)\cdot10^{-7}$	$(5,6\pm3,8)\cdot10^{-4}$	0,13
FÉU-56	1964	$(1,1\pm0,2)\cdot10^{-6}$	$(1,3\pm0,1)\cdot10^{-6}$	$(2,5\pm0,4)\cdot10^{-3}$	—
FÉU-81	1977	$(9,5\pm1,1)\cdot10^{-7}$	$(9,6\pm1,1)\cdot10^{-7}$	$(9,3\pm0,3)\cdot10^{-3}$	—
FÉU-85 (glass of the bulb	1974	$(4,0\pm1,4)\cdot10^{-7}$	$(7,2\pm1,5)\cdot10^{-7}$	$(4,7\pm0,08)\cdot10^{-2}$	0,64
FÉU-85 (dynode system and base)	1974	$(6,8\pm1,9)\cdot10^{-7}$	$(2,3\pm0,3)\cdot10^{-6}$	$(2,00\pm0,07)\cdot10^{-2}$	0,36
FÉU-87	1976	$(3,6\pm2,0)\cdot10^{-7}$	$(6,7\pm1,9)\cdot10^{-7}$	$(4,22\pm0,08)\cdot10^{-2}$	—
FÉU-93	1974	$(1,6\pm0,2)\cdot10^{-6}$	$(1,8\pm0,2)\cdot10^{-6}$	$(4,0\pm0,4)\cdot10^{-3}$	—
FÉU-110	1977	$(7,2\pm1,7)\cdot10^{-7}$	$(1,6\pm0,2)\cdot10^{-6}$	$(2,4\pm0,4)\cdot10^{-3}$	—
Quartz sand (Kyshtym, USSR)		$<9,7\cdot10^{-9}$	$<5,7\cdot10^{-9}$	$<5,9\cdot10^{-6}$	—
Quartz sand (Brasil)		$<9,4\cdot10^{-9}$	$<5,5\cdot10^{-9}$	$<2,3\cdot10^{-6}$	—
Granite (Kyzyl-Sui)		$(1,71\pm0,01)\cdot10^{-5}$	$(8,3\pm0,2)\cdot10^{-6}$	$(3,6\pm0,2)\cdot10^{-2}$	—
Granite (Kyzyl-Sui)‡		$(1,80—1,65)\cdot10^{-5}$	$(7,7—8,8)\cdot10^{-6}$	$3,6\cdot10^{-2}$	
Hypersthene granite		$(1,00\pm0,01)\cdot10^{-5}$	$(6,9\pm0,3)\cdot10^{-7}$	$(4,27\pm0,03)\cdot10^{-2}$	—
Hypersthene granite		$(10,6\pm0,3)\cdot10^{-6}$	$(6,0\pm0,5)\cdot10^{-7}$	$4,1\cdot10^{-2}$	
Hypersthene granite [8]		$(9,5\pm0,2)\cdot10^{-6}$	$(7,0\pm0,5)\cdot10^{-7}$	$(4,28\pm0,03)\cdot10^{-2}$	

*The ^{40}K concentration was obtained from the ratio $Q^{40K} = g\ ^{40}K/g = 1.18\cdot10^{-4}\ Q^{K}$ (g K/g).
†One standard deviation was assumed in estimating the errors caused by statistical fluctuations.
‡Determined with the track technique of [7].

expressed in g of X per g); m_e^X and M_{sam}^X, concentration (g) of the element in the standard source and in the sample, respectively, the concentrations determined from preceding calculations and made in the sequence Th, U, K; t_{eX}, t_{sam}, and t_b, duration of the measurements made on the standard source of the corresponding radionuclide, the sample, and the background, respectively; S_E^{eX}, area under the peak of total absorption of photons of energy E of a particular nuclide (E = 2.62; 1.76; and 1.46 MeV for Th, U, and K, respectively), the area to be considered on the spectrum of a standard source; S_E^{sam}, area under the peak of total absorptionion on the spectrum of the sample; S_E^b, area of the background spectrum produced by the equipment, the area to be calculated in the same intervals as in the case of S_E^{eX} and S_E^{sam}. In the measurements described, the areas under the peaks were calculated in the following energy intervals: 2.341-2.829; 1.644-1.993; and 1.307-1.595 MeV for Th, U, and K.

The spectrometer was calibrated with a standard ^{137}Cs source. The peak of total absorption corresponds to γ-quanta with the energy 662 keV and was set to the 190th channel of the analyzer. The energy resolution on the 662-keV line was 11%. Spectrometric information was gathered with an NTA-1024 analyzer. The stability of the spectrometric channel and the total nonlinearity of the analyzer scale were better than 1%. The duration of the measurements on each sample was chosen equal to $5\cdot10^3$, $1\cdot10^4$, or $5\cdot10^4$ sec, depending upon the purity in terms of radiation and the mass of the material to be measured.

The measurements were made in a low-background underground chamber [5]. The γ spectrometer with an NaI(Tl) single crystal as scintillator (diameter 200 × 200 mm) and a well diameter of 100 × 100 mm has been described in [6] and was inserted into an additional shield of tungsten with a low background. Under these conditions, the detector background reached 4.5 pulses/sec in the energy interval 0.1-3.5 MeV. When measurements on the samples were made, they were inserted into the detector well (Fig. 1). The background counting rate was 0.044, 0.066, and 0.253 pulses/sec in these energy intervals and under the total absorption peaks of the γ-quanta with the energies 2.62 MeV (Th); 1.76 MeV (U), and 1.46 MeV (K), respectively (Fig. 2). The

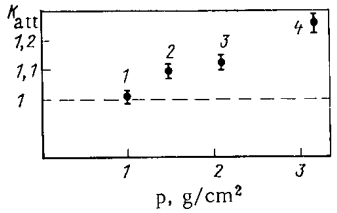

Fig. 3. Dependence of the coefficient of attentuation of 1.46-MeV γ-quanta (^{40}K) upon the density of distributed sources: 1) water; 2) ground quartz glass; 3) sand of dunite with low radioactivity; 4) cesium iodide.

errors listed in Table 1 correspond to the statistical errors with a confidence level of 65% and the range from 40 to 0.7%, depending upon the purity in terms of radiation, the mass of the sample, and the duration of the measurement. According to the data listed in Table 1, the sensitivity of the potassium measurements is nominally lower than that in the case of uranium and thorium by several orders of magnitude. The reason is that the concentration of an element is listed in that table (one must take into consideration that the ^{40}K concentration is of the order of 0.01% in the natural mixture of isotopes).

Since the photomultipliers have different configurations, the geometrical efficiency of recording was calculated for each photomultiplier type in relation to the geometry of the standard sources. Furthermore, since the granites used as standards and the samples on which the measurements were made have different density values, the figures resulting from the measurements may be too large as a consequence of the differences in self-absorption of photons of a distributed source. Additional measurements were made to assess this effect. Filler materials in the form of powders of various densities were used to prepare uniformly distributed ^{40}K, ^{238}U, and ^{232}Th sources of identical volumes and the same well volume. Differences in self-absorption were brought into account by comparing the counting rates of the initial source (salts of potassium, uranium, or thorium with a mass of approximately 50 g) with those of the same source introduced into the corresponding filler (Fig. 3). The differences in the self-absorption in the case of granite (the filler was dunite powder of low radioactivity) and in the case of glass (ground quartz glass as the filler) do not exceed the errors of the measurements (~10%). Thus, in measurements on the glass bulbs of the photomultipliers, the difference between the glass density (~1.5 g/cm^3) and the granite density (~2.3 g/cm^3) does not significantly influence the absorption of 1.46-MeV γ-quanta. In the case of photons of higher energy, the effect is of even less importance (within the measurement errors specified).

In order to take into consideration the difference in the distribution of radioactive contaminants in the entire photomultiplier and in the ground material of the various photomultiplier components, measurements were made on certain types of entire photomultipliers and on the same types of photomultipliers which had been ground to obtain a threefold increase in volume density. The volumes of the samples which were made for the measurements was the same in all cases. These measurements did not reveal counting rate differences which exceeded the limits of the statistical errors. In order to obtain exemplary estimates of the relative contribution of the metal of the dynode system and of the glass of the base, measurements on those components of one of the FÉU-49B photomultipliers were made (see Table 2).

It follows from a comparison of the samples of glass bulbs of certain photomultiplier types and quartz sand samples (see data of Table 1) that the glass bulbs of the photomultipliers must be replaced by quartz glass bulbs when low-background γ spectrometers are assembled; however, the radioactivity of the dynode system must also be considered.

TABLE 2. Concentration (g/g) of ^{232}Th, ^{238}U, and K

Sample	^{232}Th	^{238}U	K
Sample glass of socket	$(7,6\pm1,2)\cdot10^{-7}$	$(1,0\pm0,1)\cdot10^{-6}$	$(3,0\pm0,2)\cdot10^{-5}$
Dynode system of FÉU-49B	$(8,0\pm1,3)\cdot10^{-7}$	$(5,1\pm1,2)\cdot10^{-7}$	$(1,2\pm0,2)\cdot10^{-4}$

The authors thank A. A. Pomanskii for useful discussions and R. R. Asadullin and A. B. Peregud for their help in evaluating the results.

LITERATURE CITED

1. E.L. Kovalchuk, A. A. Pomansky, and A. A. Smolnikov, "The new experimental limit for the electron stability," in: Proc. Int. Conf. "Neutrino-79," Bergen (Norway), p. 164.
2. Yu. V. Sivintsev et al., At. Energ., 22, No. 1, 60 (1967).
3. V. A. Bobrov, F. P. Krendelev, and M. A. Gofman, Gamma-Spectrometric Analysis in a Low-Background Chamber [in Russian], Nauka, Novosibirsk (1975).
4. E. I. Zheleznova, I. P. Shumilin, and B. Ya. Yufa, Radiometric Analysis Techniques of Natural Radioactive Elements [in Russian], Nedra, Moscow (1968).
5. G. T. Zatsepin et al., Kratk. Soobshch. Fiz., 20, No. 6, 20 (1975).
6. E. L. Kovalchuk et al., in: Proc. of the Natural Radiation Environment, 3rd Symp., Houston, 23-28 April, 1978.
7. V. I. Glotov, Candidate's Dissertation, Inst. Nucl. Res. Acad. Sci. USSR, Moscow (1979).
8. O. P. Sobornov, Geokhimiya, 11, 1700 (1977).

SODIUM TARGET FOR A NEGATIVE-ION INJECTOR

B. A. D'yachkov, A. I. Krylov,
V. V. Kuznetsov, and N. N. Semashko

UDC 621.039.647

The thermonuclear research program performed on tokamaks and open traps [1-3] makes it necessary to develop injectors of deuterium atoms with an energy of several hundred kilovolts and a power of up to several hundred megawatts, the injectors working in quasistationary operation. Beams of atoms with such particle energies are, as far as energy is concerned, more advantageously obtained by stripping negative ions than by neutralization of positive ions, which latter method is used at lower energies [4].

A promising method of obtaining negative hydrogen and deuterium ions is the charge reversal in which a beam of primary accelerated particles with an energy of the order of several keV is converted into a beam of negative ions and atoms during the beam's passage through a target of alkali-metal vapors (e.g., cesium or sodium vapors) [5, 7]. The negative ions formed in the target can then be brought to the required energy with the aid of a preacceleration system. An advantage of this method is that the extensively developed technology of positive-ion sources [8, 9] can be employed and that (when a charge-reversal target in the form of an ultrasonic vapor stream intersecting the beam path is created) the gasdynamic properties of the stream help to reduce the gas pressure exerted upon the high-vacuum system of the injector [10, 11].

The intensity and the angular divergence of the negative-ion beam obtained by charge reversal depend upon several interrelated factors such as the intensity and the angular divergence of the primary positive-ion beam, the efficiency of beam conversion into negative ions, and the particle scattering in the target of charge reversal. The selection of the target material affects the efficiency with which negative ions are generated and the energy of the particles undergoing charge reversal; the maximum of the efficiency depends upon the target thickness; the energy of the primary beam particles accounts for the optimum current density at which the angular spread of the beam reaches its minimum, and the value of the minimum proper. Furthermore, the material of the target stream and the circulation technique determine the vapor flow from the target ("effusion") and the gasdynamic properties of the stream. Furthermore, the safety and the convenience of operation must be considered. All these factors together led to the use of sodium as the substance of a charge-reversal target in the MIN negative-ion injector [12].

The subject matter of the present article is an investigation of the properties of a sodium target with charge reversal as one of the basic elements of the MIN injector.

Translated from Atomnaya Énergiya, Vol. 49, No. 4, pp. 246-251, October, 1980. Original article submitted March 6, 1980.

0038-531X/80/4904-0699$07.50

Design and Operation of the Target of the MIN Injector

The development of the target for the MIN was preceded by testing a model of a charge-reversal sodium target of smaller dimensions (aperture diameter 100 mm). In the course of these tests, the requirements to be satisfied by a target of greater dimensions were worked out. First experiments with negative ion beams having a current of up to 0.15 A were made [6, 13].

The injector target made it possible to obtain a stream thickness of up to $5 \cdot 10^{15}$ atoms/cm^2. The apertures for the passage of the ion beam undergoing charge reversal have a size of 22×48 cm, which made it possible to expect a current of negative hydrogen ions of 5-10 A when the IBM-6 positive-ion source was employed [3].

Figure 1 schematically shows the design of the target. Molten sodium from condenser 7 is transferred with the aid of two electromagnetic pumps through heated tubes with reflex valves to a vapor generator where sodium vapors are developed. The vapor is transferred from the vapor generator through a plane-parallel Laval nozzle (critical gas section 1×500 mm) to a separating stage in which thin flaps are used to cut the peripheral vapor stream sections, which have a large divergence angle, from the vapor stream. The collimated central portion of the stream intersects the charge-reversal area of the hydrogen beam, and partial incidence upon the horizontal and vertical surfaces of the intermediate condenser 5 causes the main portion of the stream to arrive at condenser 7. The vapor stream hits all walls of the charge-reversal area and of the intermediate condenser 5. All surfaces hit by the stream are kept by a thermostat on a temperature above the melting point of sodium; for this purpose, PÉS-3 silicon oil is pumped through the tubes. The sodium con-

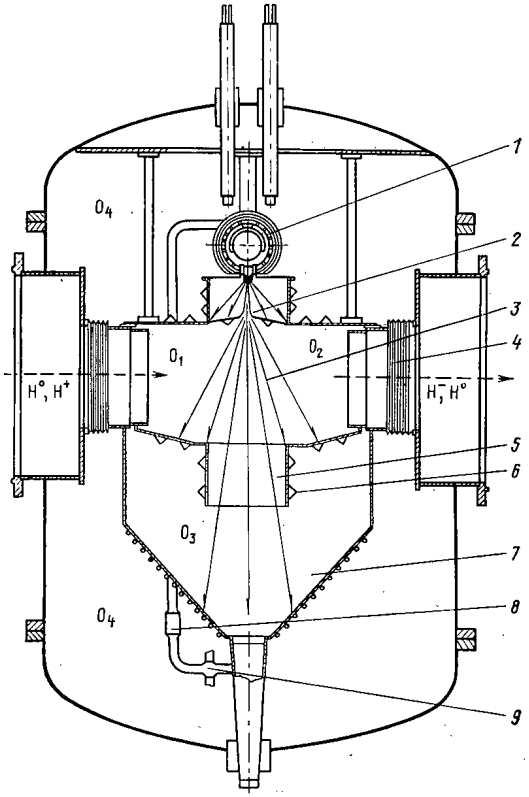

Fig. 1. Sodium target with charge reversal: 1) vapor generator; 2) separating stage; 3) region of charge reversal of the ion beam; 4) bellows; 5) intermediate condenser; 6) cooling tubes; 7) condenser; 8) reflux valve; 9) electromagnetic pump; the solid arrows indicate the sodium stream; the dashed arrows indicate the beam of ions and atoms; O_1 denotes the volume of the ion conduit between the positive ion source and the stream; O_2 denotes the volume of the ion conduit between the stream and the preacceleration system of the negative ions; O_3 denotes the volume of condenser 7; and O_4 denotes the volume of the target housing.

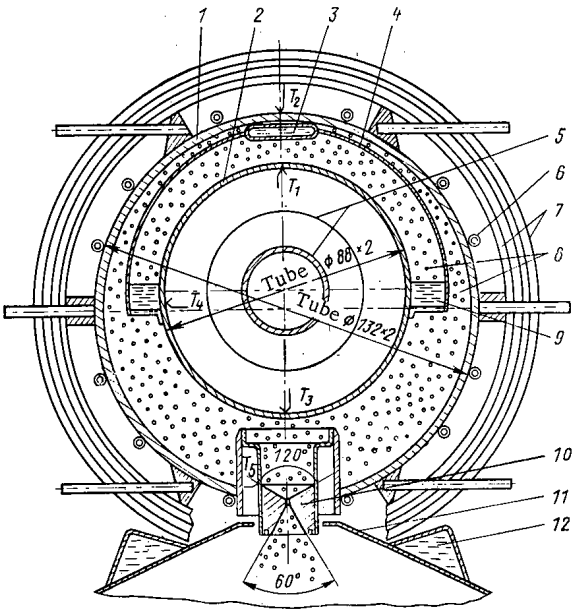

Fig. 2. Vapor generator: 1) outer cylinder; 2) inner cylinder; 3) distributing tube; 4) half-cylinder; 5) internal heater; 6) external heater; 7) shields; 8) sodium vapor; 9) pocket with liquid sodium; 10) nozzle; 11) housing of the separating stage; 12) cooling tube of the separating stage; T_1-T_5) points at which termocouples are placed.

densed on the surfaces flows to the inlet of electromagnetic pumps and is returned to the vapor generator. Thus, the sodium circulates through the target circuit. The silicon oil (boiling point ~300°C) is also used to melt the sodium when it is included in the target.

The volume O_3 of condenser 7 is evacuated by an N5T diffusion pump; the volume O_4 is evacuated by an N2T pump. The two pumps are provided with sorption traps of iron oxide. When the target was made, particular attention was paid to the tight packing of the target components separating the volume O_4 from the volumes O_1, O_2, and O_3; for this purpose, bellows were employed. During the operational use of the sodium stream, a gasdynamic separation of the volumes O_1, O_2, and O_3 occurs.

The vapor generator (Fig. 2) is a "tube in a tube" with a nozzle along the mantle of the outer cylinder. The half-cylinder and the internal cylinder form a pocket which contains liquid sodium. In order to obtain uniform arrival over the entire length of the vapor generator, the liquid sodium is introduced from both end faces through two distributing tubes with openings uniformly distributed over their length; the total area of the openings is smaller than the area of the tube cross section. The heat required for the evaporation process (up to 10 kW) is supplied by a coaxial internal tantalum heater. An additional external heater (power up to 5 kW) made of molybdenum wire is placed upon the cylinder. The geometry of the two heaters compensates for the magnetic field generated by the currents flowing through the heaters. All components of the vapor generator are made from niobium except for three outer shields made from stainless steel and except for the heaters. The sodium is admitted to the vapor generator periodically, once every 60-90 sec, with a feed pulse duration of 5-10 sec. Sodium is evaporated from the pocket and, at the time of feeding, also from the hotter surface of the inner cylinder. The vapor is incident upon the nozzle through the openings in the upper part of the half-cylinder (not shown in Fig. 2), the total area of which is about 5 cm^2. The temperature of the vapor generator is checked at various points with the aid of Chromel–Alumel thermocouples (T_1-T_5).

The separating stage, the condenser, and other target components are made from Kh18N10T steel; the current leads are made from copper. The filling of the target by sodium and the cleaning of the target are effected as described in [13].

EXPERIMENTAL MEASUREMENTS MADE WITH THE TARGET

The sodium target can be continuously operated, whereby a quasistationary vapor stream with up to $5 \cdot 10^{15}$ atoms/cm^2 is obtained. Limitations result only from the power of the electrical supply system for the

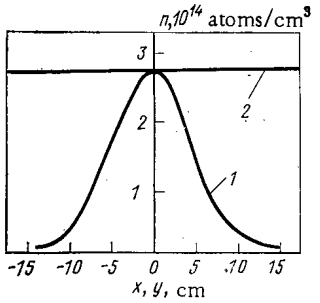

Fig. 3. Sodium vapor density in the stream: a) in the direction x of motion of the beam undergoing charge reversal; 2) in the direction y along the nozzle of the vapor generator. The abscissa 0 corresponds on the beam axis to a point which is 10 cm below the intersection of the stream with the beam axis.

internal heater of the vapor generator. The thickness of the stream is irregular in the course of time, because the rate of sodium evaporation increases when it hits the hotter surface of the inner cylinder at the time of admitting sodium (see Fig. 2). Then the thickness of the stream can increase 2-3 times.

Thickness of the Stream and Its Density Profile. The thickness of the stream is defined as $\delta = \int_{-\infty}^{+\infty} n(x)\,dx$, where n(x) denotes the concentration of the sodium vapor in the region in which the stream intersects the ion beam; and x denotes the coordinate in the direction of beam motion. The main technique used to measure the thickness is calorimetric: The thermal power of the sodium stream portion leaving the separating stage and intersecting the beam is measured. The stream thickness is calculated from the known oil consumption and the thermodynamic characteristics of both oil and sodium. The integral stream thickness averaged over a time interval of several minutes is determined with this method.

The local flow density of the sodium vapor in the region of charge reversal was determined by collecting sodium in 40 deep metal beakers placed at various points of a horizontal plane situated 10 cm below the axis of the ion beam. The stream was switched on for a certain time (between 20 and 40 min). Switching on and switching off the beam was monitored by a thermal emission probe. The amount of sodium collected was weighed thereafter. The amount of sodium and the calculated vapor velocity were used to determine n. The results of such a measurement are shown in Fig. 3.

In order to study the behavior of the stream at individual points in the course of time, a movable thermal emission probe of tungsten was employed. We recorded in the measurements the current of sodium ions formed on the glowing probe surface and accelerated by a potential difference of 3000 V between a net-shaped electrode and the emission surface. The velocity of vapor motion in the stream is greater than the local speed of sound. Direct measurements of the Mach number were not made. Indirect data indicate that the Mach number at the output of the separating stage is 3-5.

Vacuum Properties of the Target. The following evacuation conditions are encountered in the atom injector in which negative ions are used to obtain the atoms [14]. The gas of the source flows into the volume O_1 between the source of positive ions and the charge-reversal target. In this volume, the primary beam portion, which did not go through the target aperture, is liberated in the form of gas. The neutral component of the beam is picked out in the volume O_2 behind the charge-reversal target. There the gas stream from O_1 enters. When a sodium charge-reversal target is employed, the maximum efficiency in the formation of negative ions from deuterons (protons) is 0.12, i.e., 88% of the beam passing through the target is composed of atoms which must be removed from the volume O_2 by pumping means mounted behind the particle stream.

The admissible pressure in the volumes O_1 and O_2 is given by the conditions of injector operation. The pressure p_1 in the volume O_1 is limited by the stable operation of the source of the positive ions and can reach $\sim 5 \cdot 10^{-1}$ Pa. The pressure p_2 in the volume O_2 must not exceed the presure at which a noticeable stripping of the negative ions would occur before they have been accelerated to the required velocity by the preacceleration system. In the case of the MIN injector, $p_2 \leqslant 1 \cdot 10^{-3}$ Pa. In the volume between the charge-reversal target and

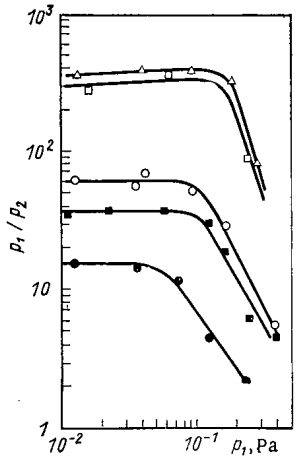

Fig. 4. Pressure drop of the various gases in the sodium stream in dependence upon the pressure in the volume on the side of gas admission: Δ – Ar; □ – N_2; ○ – D_2; ■ – He; ● – H_2; stream thickness $\delta = 3.5 \cdot 10^{15}$ atoms/cm^2.

the preacceleration system, which is close to the target and mounted in a high-voltage insulator, it is hard to obtain an efficient evacuation of the gas. When the "beam" component of the gas is removed, basically after passage through the preacceleration system, the gas flow passing from O_1 into O_2 goes directly through the region of motion of the negative ions and creates conditions for their premature stripping.

Correspondingly, the ultrasonic vapor stream generated, which intersects the ion beam, reduces the gas flow from O_1 into O_2. The stream must provide for a pressure drop from the value p_1 on the one side to the value p_2 on the other. Furthermore, the pressure p_3 arising by gas transfer from the volume O_1 into the volume O_3 must not cause a transfer from O_3 into O_2 comparable to the transfer from O_1 into O_2. Both flows of gas into the volume O_2 ($O_1 \rightarrow O_2$ and $O_1 \rightarrow O_3 \rightarrow O_2$) should be much smaller than the gas flow entering into O_2 in the form of the beam. The required pumping rate in the volume O_2 is then minimized. For example, for a stationary 75-A source of positive ions, with a gas efficiency factor of ~0.25, a pumping rate of $\sim 5 \cdot 10^3$ m^3/sec is required for obtaining a pressure of about $1 \cdot 10^{-3}$ Pa in the injector. When the gas transfer through the stream is low (<1 m^3 · Pa/sec) and the stream maintains a pressure drop of $5 \cdot 10^{-1}$–$1 \cdot 10^{-3}$ Pa, the above pressure in the first volume may be maintained with a pumping rate of about 10 m^3/sec, whereas the pumping rate in the second volume must be about 10^3 m^3/sec. In principle, this pumping rate can be obtained for the first volume in view of its evacuation by the stream of the target.

In vacuum experiments with the target, the gas contamination by the ion source was modeled. The gas was admitted in quasistationary operation (during 10 sec) and the gas flow reached 1 m^3 · Pa/sec. The target was evacuated through volume O_3 by a pump. The pressures p_1, p_2, and p_3 in the volumes O_1, O_2, and O_3 were measured (see Fig. 1). The thickness of the stream was varied in the range $(2\text{–}5) \cdot 10^{15}$ atoms/cm^2. The gas was admitted either to the volume O_1 or to the volume O_3. The measurements were made with H_2, D_2, He, N_2, and Ar gas.

Figure 4 shows the results of p_1/p_2 measurements in one mode of stream operation, when various gases were admitted. The ratio p_1/p_2 taken for various gases on the flat section of the curves indicates that the values depend upon the molecular weight of the gas and the size of its molecules. This seems to be related to the diffusion by which the gas penetrates the stream. Under the same conditions of operating the stream, the pumping rates of the gases of the stream were measured at a gas consumption of 0.8 m^3 · Pa/sec. The rates were 6.7 m^3/sec for H_2, 6.2 m^3/sec for He, 6.0 m^3/sec for D_2, 4.0 m^3/sec for N_2, and 3.6 m^3/sec for Ar.

The pressure drop p_1/p_2 (admission of gas to O_1) and p_3/p_2 (admission of gas to O_3) was strongly influenced by the delay of gas admission relative to the time at which liquid sodium was admitted to the vapor generator. This is related to the fact that the stream is not uniform in the course of time, as mentioned above. By reducing the delay from the maximum value at which the gas was directly fed in before admitting the sodium to the vapor generator to the minimum value for which the gas was admitted immediately after admission of the sodium, p_1/p_2 was increased about ten times and p_3/p_2, about three times. At the same target thickness, the drop p_3/p_2 was several times greater than for p_1/p_2 and the pressure under the stream exceeded 1 Pa. A p_1/p_2

of 100 was obtained for H_2 at $\delta = (3-5) \cdot 10^{15}$ atoms/cm^2 and $p_1 = 10^{-1}$ Pa. The curves of Fig. 4 were obtained for the same delay (nonoptimal delay).

The measurements show that the shutoff and pumping of the vapor stream in a particular target suffice at a thickness which is only 1.5-2 times greater than that required for obtaining equilibrium charge-reversal of the primary beam into negative-ion beams.

The future goal is to remove the nonuniformity of operation of the vapor generator, to improve the conditions of vapor-stream flow over the target walls in the charge-reversal region and over the walls of the intermediate condenser, and to reduce spurious gas flow in the region O_2 of high vacuum in the stream bypass (through the volume O_2). This should obviously closely approach the above requirements to reduce the pressure drop and the pumping rate.

Effusion of the Active Substance into the Target Apertures. This parameter determines the duration of target operation without reloading active substance, and the conditions of operation of the closest elements of the negative-ion injector, viz., the ion source, the preacceleration system of the negative ions, and the diagnostic system. The parameter affects to a lesser extent the contamination of the hot plasma of a thermonuclear trap because it is rather far from the target [14]. The majority of the targets used in the injectors are operated as an ultrasonic stream, which greatly reduces the effusion in comparison with other techniques. The effusion from the ultrasonic stream of the target may depend basically upon two factors: effusion from the stream proper by gasdynamic divergence during the outflow into the vacuum and by effusion owing to surface condensation. Effusion from the stream can be reduced several times by accelerating the stream to Mach numbers exceeding a certain critical value M_{cr} which depends upon the geometry of the actual target design. (For the target described, $M_{cr} = 5$). In the second case, the effusion is reduced by improving the conditions of vapor condensation and, first of all, by reducing the temperature of the surfaces on which condensation occurs. In pulsed operation of the target, the effusion from surfaces can be negligibly small, provided that one uses extensive cooling of the surfaces of condensation (e.g., by liquid nitrogen [15]). In continuous operation with circulation, the lower limit of effusion is given by the evaporation rate of the active material at its melting point. Thus, in the case of sodium the value was close to $2 \cdot 10^{-8}$ kg/m$^2 \cdot$ sec, i.e., in our case $2 \cdot 10^{-9}$ kg/sec through the aperture of the target.

The effusion was measured in several ways: by weighing thin metal sheets after their sputtering with sodium at various points of the ion conduit; using the rate of sputtering onto two walls situated at opposite ends of the ion–atom channel of the injector (the intensity of the mercury lamp light passing through the glass as a function of the sputtering by sodium was measured); also the heated emission probe mentioned above was employed. The three methods rendered similar average values of the sodium flux density from the target, viz., $\sim 4 \cdot 10^{-6}$ kg/m$^2 \cdot$ sec for $\delta = 2 \cdot 10^{15}$ atoms/cm^2. The effusion at the time of sodium admission to the vapor generator was several dozen times greater than in the rest periods between sodium admissions. However, in these rest periods the effusion was also large in comparison with the possible effusion, which is given by the average temperature of the cooling surface for oil condensation. The increased effusion is explained by the fact that the surfaces of condensation do not have a continuous cooling (the spacing of the cooling tubes is 5 cm); temperature drops of up to 200°C are possible at characteristic thermal flows (~ 2 W/cm^2) provided by the stream.

It was confirmed in a subsequent experiment that, in our case, the effusion depends not upon the removal of sodium from the stream but upon the evaporation from the surfaces of condensation. The temperature of the liquid cooling the walls of the charge-reversal region and of the intermediate condenser (Fig. 1) was reduced from 120 to 20°C. On this occasion the effusion decreased by a factor of 180. Naturally, after some time the entire quantity of sodium had been frozen out on those walls.

Thus, when pulsations in the operation of the vapor generator are eliminated, a continuous cooling of the surfaces on which sodium is condensed and, possibly, the use of independent lines for temperature stabilization designed for surfaces with various thermal loads make it possible to reduce the effusion of sodium to a level which is close to the specified evaporation rate of sodium at its melting point.

Dependence of the Divergence Angle of the H^- Beam upon the Target Thickness and the Target Composition. An electrostatic deflection system on a slit-shaped, narrow current pickup was used to analyze the distribution of the H^- current density over the angles in a filament stream of small cross section picked out on the axis of the ion beam. The measurements were made in the target thickness range of $(1-5) \cdot 10^{15}$ atoms/cm^2 at a particle energy of 3-8 keV in the initial beam and a current density equivalent to 5 mA/cm^2. At the energy 5 keV, an increase in the target thickness by $\Delta\delta = 1 \cdot 10^{15}$ atoms/cm^2 broadened the distribution function by 0.15°, which can be satisfactorily explained by twin interaction processes.

The characteristics of the H^- beam components with an energy of $\frac{1}{2}$ and $\frac{1}{3}$ of the initial energy E_0 were measured in the same experiments. These components were formed by dissociation of the molecular ions of the initial beam and charge-reversal in the target. For $\delta = 2.5 \cdot 10^{15}$ atoms/cm^2 and $E_0 = 6.5$ keV, the composition of the analyzed small filament of the H^- stream was characterized by the ratio 0.45 : 0.28 : 0.27 for H^- ions with the energy E_0, $\frac{1}{2} E_0$, and $\frac{1}{3} E_0$. The presence of a large fraction of ions with an energy below E_0 indicates that a rather intensive dissociation of molecular ions takes place in the sodium stream even at a thickness which is close to the equilibrium thickness. It was observed in measurements of the angular distribution of the current density that, in the ion stream under consideration, the width of the components with the energy $\frac{1}{2} E_0$ and $\frac{1}{3} E_0$ exceeds the corresponding value for the component with the energy E_0 by 0.1 and 0.3°, respectively.

CONCLUSIONS

The charge-reversal sodium target developed for the MIN injector corresponds at the present time to most of the requirements made on such targets for full-scale injectors of negative ions of hydrogen and deuterium. The range of thickness values obtained fully satisfies the experimental requirements and can be expanded, if necessary. The uniformity of the stream profile in space and in the course of time suffices in its present form for the experimental goals, and ways of improving it are clearly visible. This applies also to the vacuum conditions in the target and to the effusion of sodium from the target. A charge of several kilograms of sodium makes it possible to keep the target in operation for 65 h without downtime. The target was disconnected for further design improvements. A target in the form of a continuous ultrasonic stream of great width makes it possible to use in the injector not only charge-reversal properties but also vacuum shutter properties. This may greatly affect the design and the dimensions of such an injector.

LITERATURE CITED

1. E. P. Velikhov et al., At. Energ., 45, No. 1, 3 (1978).
2. G. I. Dimov, V. V. Zakaidalov, and M. E. Kishenevskii, Fiz. Plasmy, 2, No. 4, 597 (1976).
3. N. N. Semashko et al., in: Problems of Atomic Science and Technology, Thermonuclear Synthesis Series [in Russian], No. 1 (3), TsNIIatominform, Moscow (1979), p. 3.
4. B. A. D'yachkov, Zh. Tekh. Fiz., 38, No. 8, 1259 (1968).
5. J. Osher, IEEE Trans. Nucl. Sci., No. 5, 22; No. 3, 57 (1975).
6. B. A. D'yachkov et al., Preprint Inst. Atom. Energ.-2523, Moscow (1975).
7. E. Hooper, P. Willman, and A. Schlachter, Preprint UCID-17726, Livermore, LLL (1978).
8. V. M. Kulygin et al., Zh. Tekh. Fiz., 49, No. 1, 167 (1979).
9. K. Ehlers et al., in: Proc. of the 2nd Symp. on Ion Sources and Formation of Ion Beams, Berkeley, 22-25 Oct. 1974, p. 1.
10. A. I. Krylov et al., in: Trans. Fourth All-Union Conf. on Plasma Accelerators and Ion Injectors [in Russian], Moscow (1978), p. 130.
11. N. F. Vershinin, B. A. D'yachkov, and V. I. Zinenko, Pis'ma Zh. Tekh. Fiz., 5, No. 2, 110 (1979).
12. N. Semashko, V. Kuznetsov, and A. Krylov, in: Proc. Symp. on Production and Neutral. Negat. Hydrogen Ions and Beams, Report BNL-50727 (1977), p. 170.
13. B. A. D'yachkov et al., Prib. Tekh. Eksp., No. 5, 37 (1978).
14. A. I. Krylov, V. V. Kuznetsov, and N. N. Semashko, At. Energ., 48, No. 3, 186 (1980).
15. E. Hooper et al., in: Proc. Symp. on Production and Neutral. Negat. Hydrogen Ions and Beams, Report BNL-50727 (1977), p. 163.

PARTICLE ACCELERATION IN AN HF FIELD INHOMOGENEOUS OVER ITS CROSS SECTION

B. I. Bondarev and A. P. Durkin

UDC 621.384.64

One of the simplest methods of increasing the current in a linear ion accelerator is to increase the size of the aperture. This method can be employed, e.g., when superconducting solenoids focus the particles [1]. In order to determine the possibilities of accelerating particles in the channel of a linear accelerator with a rather large aperture, one must find out how an accelerating field E_z which is inhomogeneous over its cross section influences the longitudinal motion of the particles. An increase in the aperture radius causes basically two effects, viz., a change in the efficiency of particle acceleration and a perturbation of the longitudinal oscillations.

Let us consider two cases: phase of a synchronous particle changing by 2π and by π during acceleration. In the first case, the field at the boundary of the aperture can be represented in the form

$$E(z, R) = \sum_{n=0}^{\infty} E_n \cos \omega n z,$$

where $\omega = 2\pi/L$; L, period of the expansion; and R, radius of the aperture. The field inside the aperture is given by the formula

$$E(z, r) = E_0 J_0(2\pi r/\lambda) + \sum_{n=0}^{\infty} E_n \frac{I_0(2\pi T_n r/\lambda)}{I_0(2\pi T_n R/\lambda)} \cos \omega n z,$$

where $T_n = \sqrt{(n\lambda/L)^2 - 1}$; λ denotes the wavelength; and J_0 and I_0 are Bessel functions. For $n\lambda \gg L$ we have $T_n \approx n\lambda/L$ and $(2\pi/\lambda)T_n = n$.

In the second case, the field at the boundary of the aperture is of the form

$$E(z, R) = \sum_{k=0}^{\infty} E_{2k+1} \cos \frac{(2k+1)\pi z}{L},$$

where $L = \beta\lambda/2$ denotes the length of an acceleration period ($\beta = v/c$; v, particle velocity; and c, velocity of light). The field inside the aperture is defined as

$$E(z, r) = \sum_{k=0}^{\infty} E_{2k+1} \frac{I_0\left[\frac{(2k+1)\pi r}{L}\right]}{I_0\left[\frac{(2k+1)\pi R}{L}\right]} \cos \frac{(2k+1)\pi z}{L}. \quad (1)$$

The above equations show that an increase in the aperture radius means in the first case that the field on the accelerator axis tends to a constant value, the tube shielding becomes worse, and the coefficient of the flight time T decreases. In the second case, the field decreases toward the axis and this implies a deterioration of the efficiency of acceleration. The results of the subsequent considerations hold for the two cases, but in order to make our considerations more specific, we will dwell on the second case.

Let us consider the longitudinal oscillations of particles in an inhomogeneous field. When e denotes the charge of the particle, the force acting upon the particle obeys the law $F = eE(z, r)\cos(\omega t + \varphi)$. It follows from [2] as an approximation that in each period, one traveling harmonic with the amplitude E_m contributes to the acceleration and that the energy increase ΔW_s of a synchronous particle during the acceleration period is given by

$$\Delta W_s = eE_m L \cos \varphi_s.$$

Since the particles have different transverse trajectories, the distribution of the field $\tilde{E}(z) = E[z, r(z)]$ acting on the particle in various acceleration periods varies. But since only one harmonic contributes to the acceleration in each period, as indicated above, the formula

Translated from Atomnaya Énergiya, Vol. 49, No. 4, pp. 251-253, October, 1980. Original article submitted April 4, 1980.

0038-531X/80/4904-0706$07.50

$$\Delta W_s = eE_{mn}L_n \cos\varphi_{sn}$$

applies to the period with the number n. The change in E_{mn} from period to period implies a change in the synchronous phase, i.e., in each period there appears a particle which changes its phase by π during the flight in that period. This particle can be considered the center of oscillations for a given acceleration period.

Thus, $eE_{mn}L_n \cos\varphi_{sn} = \Delta W_{nR}$, where $\Delta W_{nR} = eE_{mR}L_n \cos\varphi_{sR}$ denotes the increment of the energy in the n-th acceleration period of the synchronous particle under consideration, which moves in a homogeneous field.

We obtain for determining φ_{sn}:

$$E_{mR} \cos\varphi_{sR} = E_{mn} \cos\varphi_{sn}. \tag{2}$$

When $\cos\varphi_{sn} > 1$ follows from Eq. (2), there is no synchronous particle for the particular period. When there are sufficiently many of such periods, there is the risk of the particle bunch disintegrating.

Let us describe the problem in terms of mathematics. We consider the cross section of a six-dimensional phase-plane diagram of the beam, the cross section consisting of points having identical coordinates x_0, $\dot{x}_0$, y_0, and $\dot{y}_0$ in transverse phase space at the beginning of the acceleration process. In each acceleration period, the particles oscillate relative to the synchronous particle but, as outlined above, the center of the oscillations and the frequency of the particles change from period to period. The coordinates β_{sn} (centers of the oscillations) coincide with β_s for the synchronous particle of the calculations, but the φ_{sn} values differ in neighboring periods.

We note the following changes in the equation of motion:

1) E_m is a piecewise constant function changing its value in the transition to the following acceleration period;

2) there appears a piecewise constant function χ describing the change in the position of the center of oscillations. In the period with the number k we have $\chi(k) = \varphi_{sk} - \varphi_{sk-1}$. One can assume that E_m and χ change periodically with twice the frequency $\mu = 2\mu_\Pi$ of the transverse oscillations. The projection of the six-dimensional phase-plane diagram upon the phase plane of the longitudinal coordinate and velocity is limited by a curve described around the phase patterns for all cross sections.

Obviously, the amplitudes of the change of $E_m(k)$ and $\chi(k)$ of particles from any cross section depend upon the deviation of the particles' synchronous phase $\varphi_s(k)$ from the calculated value φ_{sR}. A simple analysis of Eq. (2) shows that the change in the synchronous phase decreases with increasing φ_{sR}. This means that the acceleration of particles in a channel with large aperture is basically possible, provided that in the accelerator section of strong inhomogeneity of the accelerating field over the cross section, the synchronous phase is boosted, whereby the acceleration times are reduced. Equation (2) shows that the region of longitudinal capture decreases when the region of transverse particle oscillations corresponding to a particular cross section gets closer to the accelerator axis. The most extensive trapping corresponds to particles whose region of transverse oscillations is close to the boundary of the aperture; the least extensive trapping corresponds to particles moving along the accelerator axis.

For particles moving at a constant distance r from the accelerator axis, the constant E_{mr} and φ_{sr} values are determined from Eqs. (1) and (2). When the particles perform transverse oscillations on the path section $r_1 \leq r \leq r_2$, then $|2\nu - \mu| \gg 0$ without parametric resonance, where ν and μ denote the frequencies of the longitudinal and transverse oscillations, respectively. The particle motion in the direction of the accelerator axis can be described with the $\bar{E}_{mr}$ value averaged over the period of the transverse oscillations. In this case, $E_{mr_1} < \bar{E}_{mr} < E_{mr_2}$. Thus, the trapping region for a cross section with some initial transverse coordinates and velocities encloses the trapping region of axial particles. Thus, in order to avoid particle losses, one must concentrate the bunch before the entry into the accelerating channel so that the bunch is inscribed in the trapping region for axial particles. In this case the phase width of the entire beam is defined by the size of the region occupied by the initial phase diagram during the oscillation process at the E_m and φ_s values corresponding to the beam boundary.

Let us consider the case of small oscillations for estimating the influence of a field inhomogeneity upon the phase volume.

The equation of small oscillations has the following form for each cross section:

$$(d^2\psi/d\tau^2) + 2\delta(\tau)(d\psi/d\tau) + \tilde{\nu}^2(\tau)[\psi - \chi(\tau)] = 0. \tag{3}$$

TABLE 1. Increase in Aperture Size (R/R_0) and in the Current (I/I_0) at Various φ_{sR} Values

φ_{sR}, deg	$W_{\lambda R}/W_{\lambda 0}$	R/R_0	I/I_0
—37	1	1	1
—75	3,1	3	9
—80	4,8	3,5	12,5
—85	9	4,8	23
—88	23	6,5	42

where $\tau = \omega t$; $\psi = \varphi - \varphi_s(k)$; $2\delta(\tau) = \frac{d}{d\tau}\ln(\gamma_s^2 p_s \delta_s)$; $\tilde{\nu}(\tau) = \gamma^{-3/2}\,\tilde{\Omega}(\tau)/\omega = \bar{\nu}\sqrt{\frac{W_\lambda \mid \mathrm{tg}\,\varphi_s(k)\mid}{2\pi\beta_s}}$; p_S denotes the momentum of the synchronous particle; $\gamma = (1-\beta_S^2)^{-1/2}$; and W_λ denotes the specific acceleration.

The general form of Eq. (3) reveals that the phase volume is increased over the calculated value by changes in the form of each cross section and by displacements of the center of the oscillations. Let us consider two cases: we assume that the phase-plane diagram at the beginning of the accelerator has the same form for all cross sections and is an ellipse conforming to the calculated uniform channel or to an inhomogeneous channel for the axial particles. The longitudinal motion is described for each cross section by the migration of the initial ellipse inside its conforming ellipse. When the bunch fills the entire aperture, the above considerations lead to the conclusion that the greatest conforming ellipse is elongated relative to the initial ellipse by $\theta = \sqrt{\mathrm{tg}\,(\varphi_{sR}/\mathrm{tg}\,\varphi_{s0}}$ times in the first case, the elongation taking place in the direction of the ψ axis in the first case, and in the direction of the $\dot{\psi}$ axis in the second case.

Let us calculate the oscillation amplitude in the center of the bunch for each cross section. A change in the position of the beam center is described by the equation

$$d^2\varphi/d\tau^2 + 2\delta(\tau)(d\psi/d\tau) + \tilde{\nu}^2(\tau)\,\psi = \tilde{\nu}^2(\tau)\,\chi(\tau) \tag{4}$$

with the initial conditions $\psi(0) = \Delta\varphi_S$ and $\dot{\psi}(0) = 0$, where $\Delta\varphi_S$ denotes the deviation of the beam center from the center of the oscillations at the beginning of the accelerator.

In order to obtain an estimate of $\psi(\tau)$, we can assume for $\tilde{\nu}^2(\tau)$ in Eq. (4) the average value $\tilde{\nu}^2(\tau) \equiv \bar{\nu}_r^2$. Then the solution to Eq. (4) has the form

$$\psi = \exp\Big[-\int_0^\tau \delta(z)\,dz\Big]\Delta\varphi_s \cos\bar{\nu}_r\tau + \bar{\nu}_r \times \tag{5}$$

$$\times \exp\Big[-\int_0^\tau \delta(z)\,dz\Big]\int_0^\tau \exp\Big[\int_0^z \delta(z)\,dz\Big]\chi(z)\quad \sin\nu_r(\tau - z)\,dz = \psi_1 + \psi_2.$$

Since the exponential functions in the formulas for ψ_2 change only slowly, we can obtain

$$\psi_2(N) = 2\sin\frac{\bar{\nu}_r}{2}\sum_{k=1}^{N}\chi(k)\sin\bar{\nu}_r\left(N-k-\frac{1}{2}\right),$$

where N denotes the current number of the acceleration period; and $\chi(k) = \varphi_S(k) - \varphi_S(k-1)$. Assuming that the function $\varphi_S(k)$ is given by the first harmonic $\varphi_S(k) = \varphi_0 + \varphi_1\sin(\mu k + \varphi_2)$, we obtain $\chi(k) = 2\sin(\mu/2)\,\varphi_1\cos[\mu(k+1/2) + \varphi_2]$. The quantity $\psi_2(N)$ is the sum of the oscillations with the frequencies $\mu + \bar{\nu}_r$ and $\mu - \bar{\nu}_r$; the maximum of this function with respect to N is estimated with the formula

$$|\psi_{2\max}| \leqslant \Delta = 2\bar{\nu}_r\mu^2\varphi_1/(\mu^2 - \bar{\nu}_r^2) \tag{6}$$

(we have substituted $\sin\bar{\nu}_r/2 = \bar{\nu}_r/2$ and $\sin\mu/2 = \mu/2$).

When the particles perform transverse oscillations on the section $r_1 \leq r \leq r_2$, we may approximate $\varphi_1 = |\varphi_{sr_2} - \varphi_{sr_1}|/2$, where φ_{sr_2}, φ_{sr_1} denote the synchronous phase values for the field at the distances r_2 and r_1 from the axis, respectively. (Naturally, $\psi_2 = 0$ for $r_2 = r_1$).

The oscillations of the beam center consist of two components: ψ_1 denotes oscillations related to the shifting of the beam center with respect to the oscillation center at the beginning of the accelerator; and ψ_2 denotes oscillations related to changes in the position of the oscillation center from period to period. We note that for $\mu^2 \gg \bar{\nu}_r^2$, $\Delta = \bar{\nu}_r\Delta\varphi_r$, where $\bar{\nu}_r \leqslant (\nu_R + \nu_0)/2$, and $\Delta\varphi_r < |\varphi_{sR} - \varphi_{s0}|/2$. Since large values of the syn-

chronous phase must be selected to obtain stable acceleration, the Δ value is small relative to the width of the trapping region. Since the boundary particles have the greatest trapping region and the axial particles have the smallest trapping region, it follows from Eqs. (5) and (6) that the second version, in which the center of the bunch at the beginning of the acceleration process coincides with the center of oscillations for axial particles, is most convenient.

Thus, for obtaining stable particle acceleration in a channel with a hf field strongly inhomogeneous over the cross section, one must reduce the acceleration rates after having increased the synchronous phase. In order to reduce particle losses, one must form bunches at the input to the accelerating channel, taking into account the acceleration conditions which superimpose themselves in the case of the axial particles. The field inhomogeneity decreases in proportion to the increase in particle energy and it becomes possible to increase the acceleration rates, which means that the synchronous phase is brought to the usual values. Table 1 shows the relation between the φ_{sR} values at the aperture boundary and the admissible increase in aperture radius R and the beam current I. All values were determined under the condition that the phase of the synchronous particle is $\varphi_{s0}=-37°$ on the accelerator axis.

Let us consider the accelerating structure in the form of an H resonator enclosed by a superconducting solenoid as a possible version of the initial portion of an accelerator. Assume $\lambda=1.5$ m, an initial particle energy $W=0.75$ MeV ($\beta=0.04$), and a field strength $E=150$ kV/cm at the aperture boundary. In order to reach adequate field homogeneity in such an accelerator, one usually selects an aperture diameter $2R\approx1$ cm. We select the aperture diameter 3 cm, and then the average field on the axis is about 3 times weaker than at the aperture boundary. When we choose the synchronous phase value $\varphi_{sR}=-75°$, we have $\varphi_{s0}=-37°$ on the axis. The angle under which the gap is passed is assumed to be 100°.

An approximate calculation shows that for $W=30$ MeV ($\beta=0.245$) the field becomes almost homogeneous and the subsequent accelerator section with large aperture does in no way differ from the same accelerator section with the usual aperture. We made an approximate calculation of the accelerating channel at the section up to an energy $W\approx30$ MeV for an accelerator with large aperture and took into account that the synchronous phase at the aperture boundary changes smoothly so that for any acceleration period, the synchronous phase on the axis is constant ($\varphi_{s0}=-37°$). Then 4.5 m is obtained for the length of the section of the calculations, and the number of acceleration periods is 46. For an accelerator with a homogeneous field, $L\approx3.6$ m and $N\approx34$. Thus, a ninefold increase in the accelerator current implies an increase in its length by 25% relative to the usual form of the accelerator.

The authors thank S. K. Esin for his comments.

LITERATURE CITED

1. B. P. Murin et al., Linear Ion Accelerators [in Russian], Atomizdat, Moscow (1978).
2. I. M. Kapchinskii, Particle Dynamics in Linear Resonance Accelerators [in Russian], Atomizdat, Moscow (1966).

Programming and Computer Software

A translation of *Programmirovanie*

Editor: N. N. Govorun

This new journal provides authoritative and up-to-date reports on current progress in programming and the use of computers. By publishing papers ranging from theoretical research to practical results, this bimonthly will be essential to a wide circle of specialists. It features results of vital research in the following directions:

- logical problems of programming; applied theory of algorithms; and control of computational processes
- program organization; programming methods connected with the idiosyncrasies of input languages, hardware, and problem classes; and parallel programming
- operating systems; programming systems; programmer aids; software systems; data-control systems; IO systems; and subroutine libraries.

Subscription: Volume 6, 1980 (6 issues) $115.00

Random Titles from this Journal

NEW RUSSIAN JOURNALS

IN ENGLISH TRANSLATION

BIOLOGY BULLETIN

Izvestiya Akademii Nauk SSSR, Seriya Biologicheskaya

The biological proceedings of the Academy of Sciences of the USSR, this prestigious new bimonthly presents the work of the leading academicians on every aspect of the life sciences—from micro- and molecular biology to zoology, physiology, and space medicine.

Volume 8, 1981 (6 issues) $225.00

SOVIET JOURNAL OF MARINE BIOLOGY

Biologiya Morya

Devoted solely to research on marine organisms and their activity, practical considerations for their preservation, and reproduction of the biological resources of the seas and oceans.

Volume 7, 1981 (6 issues) $145.00

WATER RESOURCES

Vodnye Resursy

Evaluates the water resources of specific geographical areas throughout the world and reviews regularities of water resources formation as well as scientific principles of their optimal use.

Volume 8, 1981 (6 issues) $250.00

HUMAN PHYSIOLOGY

Fiziologiya Cheloveka

A new, innovative journal concerned *exclusively* with theoretical and applied aspects of the expanding field of human physiology.

Volume 7, 1981 (6 issues) $225.00

SOVIET JOURNAL OF BIOORGANIC CHEMISTRY

Bioorganicheskaya Khimiya

Features articles on isolation and purification of naturally occurring, biologically active compounds; the establishment of their structure, methods of synthesis, and determination of the relation between structure and biological function.

Volume 7, 1981 (12 issues) $275.00

SOVIET JOURNAL OF COORDINATION CHEMISTRY

Koordinatsionnaya Khimiya

Describes the achievements of modern theoretical and applied coordination chemistry. Topics include the synthesis and properties of new coordination compounds; reactions involving intraspheral substitution and transformation of ligands; complexes with polyfunctional and macromolecular ligands; complexing in solutions; and kinetics and mechanisms of reactions involving the participation of coordination compounds.

Volume 7, 1981 (12 issues) $285.00

THE SOVIET JOURNAL OF GLASS PHYSICS AND CHEMISTRY

Fizika i Khimiya Stekla

Devoted to current theoretical and applied research on three interlinked problems in glass technology; the nature of the chemical bonds in a vitrifying melt and in glass; the structure-statistical principle; and the macroscopic properties of glass.

Volume 7, 1981 (12 issues) $175.00

LITHUANIAN MATHEMATICAL JOURNAL

Litovskii Matematicheskii Sbornik

An international medium for the rapid publication of the latest developments in mathematics, this quarterly keeps western scientists abreast of both practical and theoretical configurations. Among the many areas reported on in depth are the generalized Green's function, the Monte Carlo method, the "innovation theorem," and the Martingale problem.

Volume 21, 1981 (4 issues) $175.00

PROGRAMMING AND COMPUTER SOFTWARE

Programmirovanie

Reports on current progress in programming and the use of computers. Topics covered include logical problems of programming; applied theory of algorithms; control of computational processes; program organization; programming methods connected with the idiosyncracies of input languages, hardware, and problem classes; parallel programming; operating systems; programming systems; programmer aids; software systems; data-control systems; IO systems; and subroutine libraries.

Volume 7, 1981 (6 issues) $115.00

SOVIET MICROELECTRONICS

Mikroelektronika

Reports on the latest advances in solutions of fundamental problems of microelectronics. Discusses new physical principles, materials, and methods for creating components, especially in large systems.

Volume 10, 1981 (6 issues) $195.00

Send for Your Free Examination Copy

PLENUM PUBLISHING CORPORATION, 233 Spring St., New York, N.Y. 10013
In United Kingdom: 88/90 Middlesex St., London E1 7EZ, England
Prices slightly higher outside the U.S. Prices subject to change without notice.